Development and Application of Theoretical Models for Molecular Magnetism

Author: Shashank V. Rao

ORCID: 0000-0002-0152-360X

Supervisor: A/Prof Alessandro Soncini

Presented for the Fulfilment of the Degree: Doctor of Philosophy

School Of Chemistry

University Of Melbourne

Australia

September 2019

Abstract

My thesis consists of two projects. In the first, I have worked on the development of scalar relativistic and spin-orbit coupling methods within the ab-initio framework of the package CERES, developed in our group. In the other project, I have explored for the possibility of attaining toroidal moments in magnetic rings with weak or zero spin-orbit coupling. I managed to theoretically identify entirely new families of molecules that have a degenerate ground state where it is possible to prepare a purely toroidal quantum state.

In Project 1, I have implemented the Douglas Kroll Hess method of 2nd order in the quantum chemistry code CERES to incorporate the scalar relativistic effects. I have also explored approximations to the Breit-Pauli Hamiltonian, and found that the bare one-electron operator is often sufficient to obtain reasonably good crystal field energy levels within the lowest spin-orbit multiplet. I also present a comparison between different mean-field approximations for incorporating the two-electron terms.

In Project 2, I have theoretically investigated new spin-frustrated molecular triangles that show the first known example of a toroidal quartet, composed of two degenerate toroidal doublets, solely as a consequence of spin-frustration, and despite having no spin-orbit coupling. Finally, I have generalized these findings to extended odd-membered ring, and managed to identify infinite families of molecular rings that show a ground multiplet composed of one or more toroidal doublets.

Contents

List of Figures

List of Tables

Declaration

This is to certify that:

1. The thesis comprises only my original work towards the Ph.D. except where indicated in the preface
2. Due acknowledgement has been made in the text to all other material used
3. The thesis is fewer than 100,000 words in length, exclusive of tables, maps, bibliographies and appendices

_____ _____

Shashank V. Rao Date

Preface

All work presented in this thesis is original and was conducted by the candidate during 2015-2019. The research was supervised by Associate Professor Alessandro Soncini. The student's research was funded by a Melbourne International Research Scholarship and Melbourne International Fee Remission Scholarship offered through the Melbourne India Postgraduate Program and through his supervisor's Australian Research Council (ARC) Discovery Project Grant no: DP150103254. Participation to conferences has been funded by the University of Melbourne through a Science Abroad Travelling Scholarship (2016).

The following papers have been submitted by the candidate and have been included as chapters in this thesis:

- *Spin-Orbit Coupling Descriptions of Magnetic Excitations in Lanthanide Complexes.* Shashank Vittal Rao (51% contribution), Matteo Piccardo, Alessandro Soncini, Submitted to Physical Chemistry Chemical Physics on 26th August 2019
- *Toroidal Moment in a Family of Spin Frustrated Heterometallic Triangular Nanomagnets Without Spin-Orbit Coupling: Applications to a Molecular Spintronics Device.* Shashank Vittal Rao(51% contribution), Jared M. Ashtree, Alessandro Soncini, Submitted to Physica B on 12th January 2020

_____ _____

Shashank V. Rao Date

Acknowledgements

This Ph.D. has been long time dream, come true. It has been an amazing opportunity for me to learn many new things about scholarship and its pursuit. Of course, much of what I have accomplished during these four years would not have happened if it were not for the timely efforts of several people that I would like to thank here. Firstly, I want to thank the smartest person I have met in my life, my Supervisor, Associate Professor Alessandro Soncini. From the several fruitful discussions to the tremendous amount of thought that he puts to a problem even before the first equation is written, is truly inspiring. The sheer artistry and creativity that he brings to the subject has been highly motivating. On a personal level, he has also helped me pull together when research proved challenging and encouraging me with helpful suggestions and deep insights into research and life in research. I would like to thank my Ph.D committee - Dr Lars Goerigk, who has always been a constant and proactive source of help and to Prof. Ashok Muthupandian, who has not only been a personal mentor but also for helping me bond with MIPP group. I would like to thank the university of Melbourne and the MIPP program for providing the funding for this research, it has helped tremendously. I would like to thank my Research Group- Matteo for his wise opinions on science, Simone for being the torch-bearer on being a good researcher, Kieran for engaging, thoughtful and meaningful conversations and Jared for being the sweetest friend particularly when I was at my lowest. Of course, no acknowledgement would be complete without thanking my lovely wife, Divya Rao for being my Honorspren, My parents Sujatha Rao for being my beacon of hope and Dr V. S. N. Rao for planting the seed of being a researcher in my mind. Lastly, I want to thank Yash Vakilna for providing the bedrock of my sanity, Debajit Dutta for a sincere and honest friendship and Namrata Srivastava for all the fun times.

Part I

Project 1

Chapter 1

Introduction

Nowadays Single Molecule Magnets (SMM) seem to be very promising systems to be used in the design and development of innovative technological devices for IT data storage and processing [2–6]. These are molecular systems that are capable of showing magnetic properties that one would typically associate with bulk magnets such as magnetic hysteresis. Hysteresis is a phenomena where, a material that has been magnetized by an external magnetic field does not get demagnetized upon the removal of the field, but retains some of the magnetism. The field required to demagnetize such a material is called a coercive field.

While in bulk ferromagnetism the magnetic hysteresis, is strongly determined by the thermodynamic phase of the magnet, in SMMs it is an inherently kinetic effect, usually addressed as the slow relaxation of the magnetization. [5]

This property was discovered in 1991 when it was found that a complex of Manganese [2] ($[Mn_{12}O_{12}(CH_3COO)_{16}(H_2O)_4] \cdot 2\,CH_3COOH \cdot 4\,H_2O$) [Mn12Ac] was able to show magnetic hysteresis at liquid helium temperatures. Subsequently, many other molecules have been discovered to show this behavior both including transition metals [2,7–9] and lanthanide metals [10–12] , opening to interesting possibilities of developing high density memory storage [5], magnetic imaging [13], molecular spintronics devices [14,15] and quantum computers [16]. Increasing the SMMs temperature of operability is a main goal in the development of technological applications in this area [11].

To obtain this goal, it is important to understand both the electronic structure and the spin dynamics of these molecules.

The unpaired electrons of an open-shell ion give rise to a Hunds rule ground Russell-Saunders term where the electrons achive maximal spin S and maximal angular momentum L. In complexes of transition metal ions, the effect of the ligand field most often quenches the orbital angular momentum component (i.e. fully removes the $2L + 1$ degeneracy of the Russel Saunders term), so that the ground crystal field term often can be described in terms of a pure $2S + 1$-degnerate spin manifold interacting with the lligand field and throug spin orbit coupling . The magnetically isotropic $2S + 1$ degeneracy is thus further weakly split by the combined effect of spin-orbit coupling and the low-symmetry harmonics of the crystal field potential, giving rise to magnetic anisotropy. The effect in transition metal ion complexes is known as zero-field splitting, and described, for the case of a purely axial crystal field potential, by an effective spin Hamiltonian $D * S_z^2$, where D is proportional to the gaps created by the ligand field effects within the $2S + 1$ manifold, while Z is the direction of the so-called easy axis, along which there is an energy gain for the unpaired electrons to align their spin. [1]

When an external magnetic field is applied, the Zeeman-effect causes the selective population of states aligned along the magnetic field. Upon removal of this field the magnetic anisotropy introduces a barrier to relaxation to the unmagnetized state. This process is more clearly understood with the following diagram where the case for odd number of unpaired electrons is illustrated. Here the anisotropy breaks the $2S + 1$ multiplet but preserves the degeneracy of $\pm M_S$ (Kramers degeneracy when S is half integer or Ising degeneracy when S is an integer). Upon application of a magnetic field the Kramers (Ising) doublets split. Selectively populating the spin polarized state. On removal of the magnetic field there is an anisotropy barrier of height $U_{eff} = |D|S^2$ that prevents the molecule from relaxing immediately.

$$U_{eff} = |D|S^2 \tag{1.1}$$

Through this it is possible to model spin relaxation as an Arrhenius-like equation:

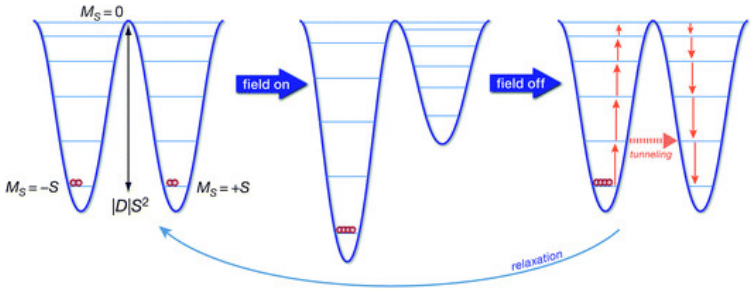

Figure 1.1: Summary of the mechanism of magnetic relaxation [1]. Vertical axis is the energy of the zero-field split energies and horizontal is the M_S quantum number.

$$\tau = \tau_0 e^{\frac{-U_{eff}}{k_B T}} \tag{1.2}$$

where τ is the lifetime at a temperature T and U_{eff} is the barrier to the relaxation to these systems. One of the conclusions that can be drawn from the above equation is that a higher U_{eff} is likely to cause a longer spin relaxation time.

A parameter that characterizes a single molecule magnet is the blocking temperature T_B below which the molecular magnetization survives for longer than a characteristic experimental time, hence giving rise to lagging or hysteresis behaviour. There are different conventions for the evaluation of the blocking temperature as it is highly dependent on the characteristic timescale of the experiment used to probe slow relaxation. The convention proposed by Gatteschi, Vilain Sessoli defines it as the temperature corresponding to a relaxation time of 100s [5]. However, it has become more common to define blocking temperature as the highest temperature at which SMMs display magnetic hysteresis for a sweeping rate of 20 Oe*s^{-1} [11].

The mechanisms that play an important role in the magnetism of SMMs have been studied since the discovery of [2] $Mn_{12}Ac$ and subsequently [7] $[Fe_8O_2(OH)_{12}(tacn)_6Br_8]$ (Fe_8Br_8), where tacn = 1,4,7-triazocyclononane. Both of these molecules have a high value of spin at $S = 10$ and a U_{eff} of 51cm^{-1} and 18cm^{-1}, respectively. We would expect from equation 1.1 that U_{eff} would be highly dependent on spin. Upon identification of this potential strategy several molecules have been synthesized which aim to increase the spin. Synthesizing SMM with high total spin it has been reached in the literature a record

barrier of 62cm^{-1} was achieved [8] with the synthesis of $S = 12$ complex $[Mn_6O_2(sao)_6(O_2CPh)_2(EtOH)_4]$, where saoH2 = 2-hydroxybenzaldehye oxime. However, it was eventually realized [1] that building ever larger rings to increase total spin was not always a viable strategy. This can be seen with [9] the molecule $[Mn_{19}O_8(N_3)_8(H_3L)_{12}(MeCN)_6]_2{}^+$ which has 19 metal centres that give a spin of 83/2. However, the U_{eff} is only a meagre 4cm^{-1}

This has, in recent times, led to the search for newer, more promising strategies to develop a single molecule magnet that can work at higher temperatures. One of the more promising strategy is the use of Ln atoms as central ions in SMM [17–21].

Ln(III) trivalent ions show strong spin-orbit coupling and as result Ln(III) complexes present an electronic structure dominated by pseudo-degenerate $^{2J+1}L_J$ multiplets where the ground state $2J + 1$-degeneracy is split by the interaction with the crystal field, which is weaker than the spin-orbit interaction [5, 6, 22]. Nonetheless, the anisotropy introduced by the crystal field effects in the case of lanthanoid complexes within the spin-orbit multiplet is greater than that of transition metals [23].

The presence of high enough axial symmetry (at least 8-fold rotation axis) in the crystal field would ensure that the states would be characterized by a sharp M_J. A low degree of overlap between the different atomic M_J states would ensure that the system did not significantly speed up relaxation across the barrier via quantum tunnelling of the magnetization (QTM), forcing the molecular magnetization to relax only via thermal excitations that can be controlled solely by temperature.

Thus ideally, lanthanide single molecule magnets could be engineered to have higher barriers of several hundred and sometimes thousands of wavenumbers, although such a tight control of QTM is by no means simply achievable through chemical synthesis, as yet. As a matter of fact, regardless of how much chemical control has been achieved to date, Ln(III)-SMMs have been shown to display slow magnetic relaxaion at higher temperatures than their transition metal ion analogues. This thinking has been validated by numerous experimental works [17–21].

When I started my Ph.D. the highest temperature ever found for SMM in LnSMMs was 14 K at a field sweep rate of 20 Oersted per second [10]. This was a Terbium dimer bridged by a participant $[N_3]^{2-}$ radical

ligand. In recent years, there has been tremendous progress in this area leading to the synthesis of Dy(III)-SMMs which show magnetic hysteresis up to 60 K [11] and, more recently, at 80 K [12] (measured at a field sweep rate of 22 Oersted per second and 25 Oersted per second respectively).

One of the key points to obtain more promising SMMs is to deeply understand they electronic structure, which calls for the aid of ab initio theoretical models. Multiconfigurational ab initio calculations on Ln(III) complexes have been quite successful [24–41].

One of the most popular methods to calculate the electronic structure of lanthanide complexes consists of the Complete Active Space Self Consistent Field via State Interaction with Spin Orbit coupling (CASSCF/RASSI-SO) method [24, 25, 42–45]. In CASSCF/RASSI-SO, a set of molecular orbitals(MO), used to build all multielectronic wavefunctions arising within a given spin-symmetry, are optimized together with the configuration interaction (CI) linear expansion coefficients describing the multiconfigurational character of the wavefunction (i.e. the CASSCF wavefunctions). Next, a suitable spin orbit coupling (SOC) operator is diagonalized on the basis of all the CASSCF multielectronic wavefunctions, where wavefunctions belonging to different spin manifolds are built from molecular orbitals that are not orthogonal to each other.

Recently, inspired by the pioneering work of McWeeny [46,47], an alternative computational strategy has been proposed by the Soncini Research Group [41, 48–50] where an average energy functional is minimized to optimize a set of MOs over the basis of all possible CI configurations arising from the 4f ligand field space, across all allowed spin symmetries, which is called the Configuration Averaged Hartree Fock (CAHF) approach. This enables the decoupling of the optimization of the CI and MO coefficients. The CI problem is then diagonalized in a second step along with a suitable SOC operator which can be defined as a Complete Active Space Configuration Interaction with Spin-Orbit coupling (CASCI-SO).

This brings us to the development of the CERES quantum chemistry code [41, 48–50] (Computational emulator of rare earth systems), a computational package developed within our group, whose aim is to develop targeted methodologies such as the CAHF/CASCI-SO for the computation of the electronic structure and magnetic properties of lanthanoid complexes. This method has also been implemented in the current version of CERES [49] to which I contributed with the activity described in this first part of the Ph.D. thesis.

Aside from of the electrostatic Hamiltonian that is a challenge in much of many-body quantum mechanics, the lanthanoid complex is further complicated by the presence of not negligible relativistic effects. Relativistic effects in quantum mechanics are better discussed within the framework set by the Dirac equation. [51].

The Dirac equation is solved by a 4 components wavefunction, but many strategies have been proposed in the literature to reduce it to 2 components, which makes its study simpler, and the computational simulations significantly more feasible. We assume that the energy scales are significantly smaller than what would be needed for matter-antimatter pair-production. This produces a two component method which can be intuitively visualized in a Bohr-like picture.

As the nuclear charge increases, the innermost electrons move quite faster and faster to have a large enough centrifugal force to keep them in orbit. In a lanthanide atom this speed is large enough to be comparable to the speed of light. This is the part of the relativistic corrections that are considered spin-free

In addition, the orbit of the f-electrons is large enough that the orbital magnetic moment of the electrons becomes quite high. The resulting magnetic interaction with the spin magnetic moment can cause the energy levels to shift. This is incorporated in the spin-dependent part.

While there are many ways to make the reduction of the Dirac equation from 4 to 2 components, the most popular method is that proposed by Douglas, Kroll and Hess (DKH), which makes use of perturbation theory. [51–54]. This can be done to any order of perturbation theory, but in practice the second order flavour DKH2 is sufficient. DKH2 is particularly useful, as it enables us to transform the Hamiltonian into a two component form that accounts for the relativistic speeds of electrons. Thus, the rich architecture of the many body theory available for two component quantum mechanics can be subsequently deployed.

Scalar relativistic effects within the DKH2 formalism are computed using some fundamental numerical ingredients which consist of molecular integrals over the atomic basis set (typically Gaussian Type Orbitals) of a special operator which involves the product of the electrons linear momentum (p), the nuclear attraction potential (V) and the linear momentum again, for short referred to as pVp integrals. Part of my project consisted in the implementation of such integrals instrumental for the DKH2 approximation to the scalar relativistic one-electron part of the molecular Hamiltonian, within the code CERES developed in the Soncini

Research Group. This implementation work is described in Chapter 2, after an introduction to the theoretical background needed to discuss the underlying ab initio approach to the calculation of the electronic structure of Ln(III) complexes.

Moreover, the spin-dependent effects are most usually incorporated via an appropriate spin-orbit coupling operator, usually given by the Breit-Pauli Hamiltonian [55–57]. This can be further subdivided into a one-electron component and a two-electron component. The one-electron part represents the interaction of the spin magnetic moment of the electron with the magnetic moment that arises from its orbiting in the Coulomb field of the nucleus. Similarly, the two-electron term accounts for the relative motion of two-electrons. This is further subdivided into two categories: the first is the interaction of the orbital magnetic moment of one on the spin of the other. The second is the interaction between the magnetic moment of the two spins.

The use of the full Breit-Pauli operator is quite expensive. As a result there are several approximations that have been suggested which have been implemented in different software packages. These approximations range from the atomic approximation [58–60] of Hess and Schimmelpfenning which is implemented in MOLCAS package, to the Resolution of Identity Method which is implemented in the ORCA package [61].

However, while the inclusion of two-electron contributions also via mean field theories is well known to be fundamental for the evaluation of spectroscopic excitations in Ln(III) complexes, what level of spin-orbit coupling interactions is needed for a sufficiently good description of magnetic excitations between the crystal field levels of the ground spin-orbit multiplet has never been explored. This is the aim I set off to discuss in Chapter 3, where a comparative analysis of one-electron and possible mean field representations of the two-electron spin-orbit operators is presented combined with a thorough application of a recently proposed strategy involving the use of the Cholesky decomposition of the two-electron SOC integrals [50]. I summarize the results of the work of Part 1 in Chapter 4.

Chapter 2

Implementation of Scalar Relativistic Effects in the Ab-initio Package CERES

This Chapter starts with a brief and basic overview of the theoretical methods that are currently used for the ab-initio description of the ground crystal field energy levels and magnetic properties in lanthanide complexes. I present an overview of the main physical effects that need to be accounted in the description of lanthanide complexes, such as electron correlation and spin-orbit coupling, and then proceed with a discussion of such effects with a special focus on the developments I have been involved in during my Ph.D. studies and their implementations in the quantum chemistry package CERES, an ab initio tool fully developed in the Soncini Research Group [41, 48–50], which is specifically designed for the simulation of the crystal field splitting of the lowest spin-orbit coupling multiplet in lanthanide complexes, and the calculation of their magnetic properties.

More specifically, I present my studies on the spin free and spin dependent relativistic effects within the framework of the multiconfigurational CAHF/CASCI-SO method [41, 48].

Next, I proceed with a brief introduction to two-component methods for the calculation of relativistic effects, on the basis of which, I finally discuss my contribution to the implementation of the scalar relativistic one-electron Hamiltonian within the CERES ab initio package.

2.1 Quantum Chemistry Calculations for Lanthanide Complexes

2.1.1 The Electronic Schrödinger Equation

The wavefunction is a mathematical tool that is used to describe the quantum state of a system. A wavefunction denoted by $\Psi(x, X, t)$ would depend on time t, the spatial and spin coordinates of n electrons $x \equiv \{x_i\}(i = 1, 2, 3, 4...n)$ as well as the spatial and spin coordinates of N nuclei $X \equiv \{X_I\}(I = 1, 2, 3, 4...N)$. Within the framework of non-relativistic quantum mechanics, the wavefunction can be determined solving the the Schrödinger equation [62, 63].

$$i\hbar\frac{\partial}{\partial t}\Psi(x, X, t) = \hat{H}\Psi(x, X, t), \tag{2.1}$$

where, the Hamiltonian operator $\hat{H}$ describes the total energy of a system and $\hbar$ is the reduced Planck's constant. If the Hamiltonian is time-invariant, it is possible to factor out $\Psi(x, X, t)$, in a time-independent component and a time-dependent phase factor, as:

$$\Psi(x, X, t) = \psi(x, X)e^{-\frac{iEt}{\hbar}}, \tag{2.2}$$

now $\psi(x, X)$ just depends on the space and spin coordinates of the electrons and nuclei, and it can be determined solving the time-independent Schrödinger equation [62, 63].

$$\hat{H}\psi(x, X) = E\psi(x, X), \tag{2.3}$$

where $\psi(x, X)$ is the eigenfunction associated to the eigenvalue E, the corresponding energy.

The full expression of the time-independent molecular Hamiltonian reads(in atomic units):

$$\hat{H} = -\sum_i \frac{1}{2}\nabla^2_{r_i} - \sum_I \frac{1}{2M_N}\nabla^2_{R_I} - \sum_{i,I} \frac{Z_I}{|\mathbf{r_i} - \mathbf{R_I}|} + \sum_i \sum_{j>i} \frac{1}{|\mathbf{r_i} - \mathbf{r_j}|} + \sum_I \sum_{J>I} \frac{Z_I Z_J}{|\mathbf{R_I} - \mathbf{R_J}|} \tag{2.4}$$

here the r_i and m_e is the spatial coordinates and mass of the electron,the R_I, Z_I and M_N is the spatial coordinates, charge and mass of the nuclei, the Laplace operator is $\nabla^2 = \frac{\partial^2}{\partial x^2} + \frac{\partial^2}{\partial y^2} + \frac{\partial^2}{\partial z^2}$ and ϵ_0 is the permittivity of free space.

Since the nuclei are much heavier than the electrons ($m_p \approx 1836 m_e$ and $m_n \approx 1839 m_e$), it is reasonable to assume that the nuclei are stationary when dealing with the motion of the electrons. This way it becomes possible to assume the nuclei as fixed in space during the electronic motion, hence they become static sources of attractive electrostatic potential for the electrons. This is known as the Born-Oppenheimer approximation, where nuclei are decoupled from the electrons and $\psi(x, X)$ becomes

$$\psi(x, X) = \psi(x; X)\chi(X), \tag{2.5}$$

where $\chi(X)$ depends just the nuclear coordinate and the electronic coordinate $\psi(x; X)$ depends parametrically on the nuclear coordinates X. Furthermore, under this approximation the Schrödinger equation (2.3) simplifies into the electronic Schrödinger equation, or many-electron Schödinger equation, which reads:

$$\hat{H}_e \psi(x; X) = E_e(X)\psi(x; X) \tag{2.6}$$

where $E_e(X)$ is the electronic energy which has a parametric dependence on the nuclear configuration X

$$\hat{H}_e = \hat{T}_e + \hat{V_{ee}} + \hat{V_{eN}} \tag{2.7}$$

2.1.2 The Hartree Fock Theory

The simplest way to write a multielectron wavefunction $\psi(\mathbf{x})$ that is antisymmetric with respect to coordinate exchange is the Slater Determinant [62, 63]

$$\psi(x_1, x_2, x_3, x_4, \ldots, x_n) = \frac{1}{\sqrt{n!}} \begin{vmatrix} \chi_1(x_1) & \chi_2(x_1) & \ldots & \chi_n(x_1) \\ \chi_1(x_2) & \chi_2(x_2) & \ldots & \chi_n(x_2) \\ \vdots & \vdots & \ddots & \vdots \\ \chi_1(x_n) & \chi_2(x_n) & \ldots & \chi_n(x_n) \end{vmatrix} \tag{2.8}$$

where $\chi_i(x_j)$ is a mono electronic wavefunction dependent just on the coordinates x_j. While the trial function in (2.8) has the expected anti-symmetry property, the one-electron orbitals $\chi_i(x_j)$ are still unknown. The optimal one-electron orbitals χ_i can then be variationally determined by minimizing the total energy of the trial wavefunction Eq. (2.8).

The Hartree-Fock method consists of exactly the aforementioned variational procedure, consisting in the optimization of a set of trial orbitals χ_i so to minimize the energy of a single Slater determinant wavefunction (or of a wavefunction that is a fixed linear combination of a number of Slater determinant functions). This leads to effective mean-field one-electron eigenvalue equations for an effective one-electron operator F, called the Fock Hamiltonian or Fock operator, which needs to be iteratively solved as the mean field Fock Hamiltonian depends on the current guess for the orbitals χ_i themselves. The form of ψ in Eq. (2.8) implies an independent particle model, which, while in fact capable of describing some correlation effect in the motion of electrons with the same spin, it is by definition completely incapable of describing any correlation at all in the motion of electrons of opposite spin. Any improvement in this direction i.e. any attempt at describing electron correlation effects, must necessarily imply the optimization of a wavefunction that is a linear superposition of Slater determinants, in which not only the one-electron orbitals are optimized, but also the coefficients of the linear combination, known in general as Configuration Interaction (CI) coefficients. This is discussed in the next section.

2.1.3 Post-HF Methods

A better approximation to $\psi(x)$ is given as:

$$|\psi\rangle = \sum_{i=0} c_i |\phi_i\rangle \tag{2.9}$$

where $|\phi_i\rangle$ is a Slater determinant describing an antisymmetrised product of a set of MOs, each determinant corresponding to a chosen relevant occupation of a given set of MOs. If all possible configurations arising from a specific choice of an atomic or molecular one-electron basis are incorporated in the linear expansion (2.9), then the method is called full CI (FCI) [64] and for this case the orbital optimization becomes redundant. However, this is unfeasible except for the smallest molecules, which leads to approximations to the full CI

wavefunctions, leading to restricted CI methods being more common in practice, such as CIS, CID and CISD, in which single, double and both single and double excitation to the lowest energy Slater determinant are taken into account, although such truncation of the CI expansion suffers from problems such as size extensivity.

To overcome the problems related to such arbitrary truncations of the CI expansion, Roos [65] proposed a method that preserves some desirable mathematical properties of the full CI approach (i.e. size extensivity, invariance of the energy under change of one-electron basis within the excitation space etc.), while heavily reducing the computational cost, at the expense of reduced capability of capturing correlation effects. The method is known as Complete Active Space Self Consistent Field (CASSCF), and is tantamount of writing a full CI expansion within a subset of one-particle orbitals, which define the so-called active space. In such approach, the full CI coefficients within this active space are optimized simultaneously with all the one-particle orbitals (usually molecular orbitals), which makes it a specific form of multiconfigurational self-consistent field (MCSCF) method. Such an approach has proven successful for specific problems in that it is capable of fully capturing a special component of electron correlation known as static correlation or strong electron correlation, at the expense of usually not being capable of capturing the so-called dynamical correlation. Since in lanthanide ions strong electron correlation, related to the large pseudo-degeneracy or multiconfigurational character of the wavefunction, is a large component of the overall interactions, CASSCF, especially as implemented in the MOLCAS package [42], has been very successful to study Ln(III) SMMs. The minimal active space here consists of the multielectron configurational space spanned by the 4f orbitals only, also known as the ligand field space.

In the case of Ln(III) complexes, after several CASSCF wavefunctions have been optimized (typically within a state-averaged CASSCF approach where the same orbitals are optimized for a whole spin manifold of electronic configurations, with one state-averaged CASSCF carried out for each spin symmetry), we still need to diagonalize a suitable Spin-Orbit coupling operator over the basis of these CASSCF wavefunctions. Thus the complete method is called CASSCF/RASSI-SO. We will analyse these spin-orbit effects later in this thesis, in more detail.

The CASSCF/RASSI-SO method has been implemented and widely tested for the calculation of the electronic structure and magnetic properties of lanthanide complexes by the molecular magnetism community [24–35]. At the time I began my Ph.D. work, this was the method of choice for computing electronic structure and properties for lanthanide single molecule magnets such as g-tensors, magnetic susceptibility and crystal field energies.

One of the limits of CASSCF/RASSI-SO approach to the calculation of the electronic structure of Ln(III) complexes consists of the fact that one needs to represent and diagonalize a spin orbit coupling operator on a basis of several CASSCF subspaces built on optimized molecular orbitals, where molecular orbitals from different subspaces are not orthogonal to each other. Such non-orthogonal problem slows down calculations, especially for the larger basis sets, and for those ions having several accessible spin symmetries, such as Dy(III).

To overcome this deficiency of the CASSCF/RASSI-SO computational strategy, the Configuration Averaged Hartree-Fock [41] (CAHF/CASCI-SO) method, which will be briefly described in the next section, was proposed and implemented in the quantum chemistry package CERES [41,48,49]within the Soncini Research Group.

2.1.4 CAHF/CASCI-SO

In CASSCF the molecular orbital optimization is driven by the minimization of the energy of one specific (i.e. state specific CASSCF) or more (i.e. state averaged CASSCF) electronic states. Because of the degeneracy in the energies of the isolated metal, for Ln complexes the variational optimization is usually conducted on the average energy of the lowest energy N states, where N is calculated by taking all the possible combinations of the 4f electrons in the 4f orbitals and given a total spin S. If the number of CI roots entering the average energy functional equals the number of slater determinants entering the CI expansion, then the optimization problem becomes decoupled from the CI problem. This is because the average energy in this case coincides with the trace of the CI variational matrix (divided by the number of the roots):

$$\sum_i \epsilon_i = Tr\left[\mathbf{H}_{CI}\right] \tag{2.10}$$

where ϵ_i are the eigenvalues of the CI matrix. Which is independent by any rotation of the CI basis.

This allows the orbital optimization to be resolved at first within the configurational averaged Hartree-Fock (CAHF) method, where now the CAHF energy functional is defined as the average energy of all the single determinant configurations spanning the full 4f active space, followed, in a completely separate step, by a small CI diagonalization, where the spin-orbit coupling Hamiltonian is added to the electrostatic Hamiltonian before the CASCI, which thus results in a CASCI-SO approach for the optimization of the CI coefficients only. [41]

The CASCI-SO step thus includes all (14, n) Slater determinants arising from all possible occupations (regardless of spin) of the 14 4f-spin orbitals by the n 4f electrons of a given lanthanide ion. As shown in refs [41,48], the separation into spin-symmetries can be safely ignored by virtue of strong spin orbit coupling in lanthanide ions, which is significantly mixing many-electron configurations of different spin, and thus is more conveniently diagonalized together with the full 4f-CI problem. The approach was inspired by the work of McWeeny et al. [46]. CAHF/CASCI-SO has been implemented in dedicated program for for the electronic structure and magnetic properties of Ln(III) complexes, named CERES [41,48,49].

2.2 Relativistic Effects in Lanthanoid Complexes

The properties and energies of many transition and heavy element compounds are strongly influenced by relativistic effects [52], which are accounted for by the Direct equation, the Lorentz invariant equation of motion for the quantum mechanical relativistic electron, described in this theory by a four-component wavefunction. The time-independent version of the Dirac equation for a hydrogenoid atom reads:

$$\hat{H}_D\phi = \left[c\boldsymbol{\alpha}\cdot\mathbf{p} + (\beta-1)mc^2 + V\right]\phi = E\phi \tag{2.11}$$

where V is an attractive potential of the Coulomb type $V = \frac{Ze^2}{r}$. The scale of energies has been shifted by the rest energy of the electron mc^2. The Dirac matrices are given by:

$$\boldsymbol{\alpha} = \begin{pmatrix} \mathbf{0} & \boldsymbol{\sigma} \\ \boldsymbol{\sigma} & \mathbf{0} \end{pmatrix}, \quad \boldsymbol{\beta} = \begin{pmatrix} \mathbf{1} & \mathbf{0} \\ \mathbf{0} & \mathbf{1} \end{pmatrix} \tag{2.12}$$

and the $\boldsymbol{\sigma}$ are the Pauli matrices given by:

$$\sigma_x = \begin{pmatrix} 0 & 1 \\ 1 & 0 \end{pmatrix}, \quad \sigma_y = \begin{pmatrix} 0 & -i \\ i & 0 \end{pmatrix}, \quad \sigma_z = \begin{pmatrix} 1 & 0 \\ 0 & -1 \end{pmatrix}, \tag{2.13}$$

It can be shown that the Dirac 4-spinor can be partitioned into two large components and two small components, which, at the relatively low energies of interest to chemistry, describe a weakly coupled particle-antiparticle pair each having spin 1/2 (i.e. described by a 2-spinor), i.e. the electron and the positron, respectively. It is thus customary in quantum chemistry to perturbationally eliminate the small components, which results in a two-component equation for the spin 1/2 electron only.

It is thus expedient to decouple the large and small components of the 4 component Dirac Spinor and then to subsequently decouple the computationally expensive spin dependent part from the spin free part of the the electron-only relativistic Hamiltonian.

This would give us a two-component Hamiltonian that is capable of incorporating the spin free relativistic effects and also enable us to directly incorporate all of the theoretical tools developed for non-relativistic quantum mechanics.

The spin-free effects are accounted for by two broad decoupling schemes. The first scheme consists of the elimination based techniques, which rely on the observation that the small component is suppressed by a factor of $(2mc)^{-1}$ as compared to the large component, for weak potentials. This leads to the "Regular Approximations" (RA) [66] of which the zeroth order (ZORA) and first order (FORA) are the most popular.

The second decoupling startegy relies on the application of suitable unitary transformations to the Dirac Hamiltonian to block diagonalize it. The first attempt in this direction was made by Foldy and Wouthuysen [67]. although the approach gives rise to highly singular terms in the presence of an external potential. Also, the wavefunctions in this method are not analytic near $\frac{1}{c} \to 0$ resulting in an ill defined non-relativistic limit.

Only the free particle Foldy Wouthuysen(fpFW) transformation can be used in a way that avoids expansion in terms of $\frac{1}{c}$, where here the block diagonalizing transformation matrix U_0 to apply to the Hamiltonian is given by:

$$U_0 = A_p(1 + \beta R_p) \tag{2.14}$$

with

$$A_p = \sqrt{\frac{E_p + mc^2}{2E_p}}, \quad E_p = \sqrt{\mathbf{p}^2c^2 + m^2c^4}, \quad R_p = \frac{c\boldsymbol{\alpha} \cdot \mathbf{p}}{E_p + mc^2} = \boldsymbol{\alpha} \cdot \mathbf{P_p} = \mathcal{R}_p \boldsymbol{\alpha} \cdot \mathbf{p} \tag{2.15}$$

This results in the Hamiltonian

$$H_1 = U_0 H_D U_0^\dagger = \mathcal{E}_0 + \mathcal{E}_1 + \mathcal{O}_1 \tag{2.16}$$

where the $\mathcal{E}$ denotes even (diagonal) terms and $\mathcal{O}$ denotes odd (off-diagonal) terms and the subscript denotes the order of the external potential. These terms evaluate to:

$$\mathcal{E}_0 = \beta E_p - mc^2, \quad \mathcal{E}_1 = A_p(V + R_p V R_p)A_p, \quad \mathcal{O}_1 = \beta A_p \left[R_p, V\right] A_p \tag{2.17}$$

A systematic way of eliminating the odd terms to generate higher order terms, is the Douglas-Kroll-Hess (DKH) method [52–54]. The core strategy in this method is to perform progressive unitary transforms to move perturbatively to a block diagonal Hamiltonian, or at least one where the off diagonal term is very small. Hence, considering that the first unitary transformation coincides with the fpFW transformation, the DKH perturbative decoupling strategy reads:

$$H_{bd} = U H_D U^\dagger \tag{2.18}$$

$$= \ldots U_4 U_3 U_2 U_1 H_1 U_1^\dagger U_2^\dagger U_3^\dagger U_4^\dagger \ldots \tag{2.19}$$

$$= \sum_{k=0}^{\infty} \mathcal{E}_k \tag{2.20}$$

$$= \sum_{k=0}^{\infty} \begin{pmatrix} \mathcal{E}_{k^+} & 0 \\ 0 & \mathcal{E}_{k^-} \end{pmatrix} = \sum_{k=0}^{\infty} \begin{pmatrix} \mathcal{E}_{k^+}^{sf} + \mathcal{E}_{k^+}^{sd} & 0 \\ 0 & \mathcal{E}_{k^-}^{sf} + \mathcal{E}_{k^-}^{sd} \end{pmatrix} \tag{2.21}$$

The $\mathcal{E}_k$ is a 4×4 matrix operator consisting of two 2×2 operators $\mathcal{E}_{k^+}$ and $\mathcal{E}_{k^-}$ which are the energies in block diagonal form, which can be further decomposed into spin free (sf) and spin dependent (sd) components.

The Douglas-Kroll-Hess transformation can be systematically calculated to any arbitrary order for $\mathcal{E}_{k^+}$. However, the DKH of the order 2 is already sufficient to account for the largest part of the relativistic correction to the molecular Hamiltonian.

The kernels of the integral operator are well known e.g. in the References [52–54].

2.2.1 Implementation of DKH2

The implementation of the DKH terms up to the second order as presented in the previous paragraph leads to modifications in the kinetic energy T_e and nuclear attraction $\hat{V_{eN}}$ terms in the non relativistic Hamiltonian. Only the one-electron operators for kinetic energy($\hat{T_e}$) and nuclear attraction($\hat{V_{eN}}$) are affected. The corrections to the two-electron term ($\hat{V_{ee}}$) are small and can be neglected. As evident from the explicit forms of the decoupled block diagonal even terms e.g. Eq. (2.16), (2.17) and (2.18), after substitution of appropriate operators defined in Eq. (2.15), to evaluate the DKH2 re-dressed kinetic energy and nuclear potential operators one needs to evaluate integrals of the form $\hat{p} \cdot (\hat{V}_{eN})\, \hat{p}$ over the Gaussian Type Orbital atomic basis.

The widely adopted strategy (across quantum chemistry software such as ORCA, MOLCAS, MOLPRO etc.) [51–54] is to transform all the operators involved in the DKH2 transformation to the basis of the p^2 eigenfunctions, where the kinetic energy is diagonal. In such basis it is then straightforward to compute the DKH Hamiltonian by evaluating all even order terms resulting from Eq. (2.18) up to the desired order of perturbation theory, second order in our case. As a last step, we transform the Hamiltonian back to position space.

The implementation of the DKH Hamiltonian in CERES has been hindered by the fact that the that the open source library used by CERES for the calculation of molecular integrals, LIBINT [68], did not perform the calculation of the $\hat{p} \cdot (\hat{V}_{eN})\, \hat{p}$ integrals. (Note: No package aside from LIBINT was used to implement the following procedure)

As a result the $\langle \hat{p} \cdot (\hat{V}_{eN})\, \hat{p} \rangle$ had to be implemented based on the calculation of the nuclear attraction potential integrals $\langle V_{eN} \rangle$ in LIBINT. In order to do this I developed a particular way of implementing the

known DKH method by using some properties of the Cartesian Gaussian functions. A Cartesian Gaussian function is defined by [63]:

$$\chi_a^{ijk}(\mathbf{r}_A) = x_A^i y_A^j z_A^k e^{-a\mathbf{r}_A^2} \tag{2.22}$$

where $\mathbf{r}_A = (x_A, y_A, z_A)$ are the position with respect to nucleus A, a is the Gaussian exponent, i, j, k are Cartesian Gaussian quantum numbers, which are non-negative integers such that $L_a = i+j+k$ is the angular momentum associated with $\chi_a(\mathbf{r}_A)$

On this basis we can write:

$$\langle \chi_a^{ijk}(\mathbf{r}_A) | \hat{p} \cdot (\hat{V}_{eN})\, \hat{p} | \chi_b^{lmn}(\mathbf{r_B}) \rangle = pVp(i,j,k,l,m,n) \tag{2.23}$$

$$\langle \chi_a^{ijk}(\mathbf{r}_A) | V_{eN} | \chi_b^{lmn}(\mathbf{r_B}) \rangle = V(i,j,k,l,m,n) \tag{2.24}$$

A particular property of the Cartesian Gaussian is its ability to be factored into components

$$\chi_{ax}^{ijk}(x_A) = x_A^i e^{-ax_A^2} \Rightarrow \chi_a^{ijk}(\mathbf{r}_A) = \chi_{ax}^i(x_A)\chi_{ay}^j(y_A)\chi_{az}^k(z_A) \tag{2.25}$$

It also has the iterative relation:

$$\frac{d\chi_{ax}^i(x_A)}{dx} = 2a\chi_{ax}^{i+1}(x_A) - i\chi_{ax}^{i-1}(x_A) \tag{2.26}$$

we also use the equation [52]:

$$\langle \chi_a^{ijk}(\mathbf{r}_A) | \hat{p} \cdot (\hat{V}_{eN})\, \hat{p} | \chi_b^{lmn}(\mathbf{r_B}) \rangle = \langle \nabla\chi_a^{ijk}(\mathbf{r}_A) | V_{eN} | \nabla\chi_b^{lmn}(\mathbf{r_B}) \rangle \tag{2.27}$$

It becomes then possible to express the needed $pVp(i,j,k,l,m,n)$ using (2.25)-(2.27):

$$\begin{aligned} pVp(i,j,k,l,m,n) = {} & 4abV_{i+1,j,k,l+1,m,n} - 4alV_{i+1,j,k,l-1,m,n} - 4biV_{i-1,j,k,l+1,m,n} + 4liV_{i-1,j,k,l-1,m,n} \\ & + 4abV_{i,j+1,k,l,m+1,n} - 4amV_{i,j+1,k,l,m-1,n} - 4bjV_{i,j-1,k,l,m+1,n} + 4mjV_{i,j-1,k,l,m-1,n} \\ & + 4abV_{i,j,k+1,l,m,n+1} - 4anV_{i,j,k+1,l,m,n-1} - 4bkV_{i,j,k-1,l,m,n+1} + 4nkV_{i,j,k-1,l,m,n-1} \end{aligned} \tag{2.28}$$

Equation (2.28) has been implemented in CERES for the evaluation of DKH corrections to the molecular Hamiltonian within the CAHF/CASCI-SO computational strategy.

The spin dependent effects which were neglected in the preceding discussion will be taken more in detail in the next chapter which is a paper I have authored and it deals with this subject in more detail.

Chapter 3

Spin-Orbit Coupling Descriptions Of Magnetic Excitations in Lanthanide Complexes

Authors: Shashank V. Rao, Matteo Piccardo, Alessandro Soncini

Affiliation: The School of Chemistry, University of Melbourne, Parkville, Victoria 3010, Australia

Submitted: 26th August 2019

Journal: Physical Chemistry Chemical Physics

Manuscript No.: CP-ART-08-2019-004638

Abstract

We present a number of computationally cost-effective approaches to calculate magnetic excitations (i.e. crystal field energies and magnetic anisotropies in the lowest spin-orbit multiplet) in lanthanide complexes.

In particular, we focus on the representation of the spin-orbit coupling term of the molecular Hamiltonian, which has been implemented within the quantum chemistry package CERES using various approximations to the Breit-Pauli Hamiltonian. The approximations include the (i) bare one-electron approximation, (ii) atomic mean field and molecular mean field approximations of the two-electron term, (iii) full representation of the Breit-Pauli Hamiltonian. Within the framework of the CERES implementation, the spin-orbit Hamiltonian is always fully diagonalized together with the electron repulsion Hamiltonian (CASCI-SO) on the full basis of Slater determinants arising within the $4f$ ligand field space. For the first time, we make full use of the Cholesky decomposition of two-electron spin-orbit integrals to speed up the calculation of the two-electron spin-orbit operator. We perform an extensive comparison of the different approximations on a set of lanthanide complexes varying both the lanthanide ion and the ligands. Surprisingly, while our results confirm the need of at least a mean field approach to accurately describe the spin-orbit coupling interaction within the ground Russell-Saunders term, we find that the simple bare one-electron spin-orbit Hamiltonian performs reasonably well to describe the crystal field split energies and g tensors within the ground spin-orbit multiplet, which characterize all the magnetic excitations responsible for lanthanide-based single-molecule magnetism.

3.1 Introduction

The use of lanthanoid atoms as central metal ions in inorganic complexes seems to be the most promising way to achieve Single Molecule Magnets (SMM) with high operational temperatures [3, 4, 11, 12, 69]. This promise comes from the characteristic electronic structure properties of the lanthanide complexes, which involve only a weak mixing of the valence f-orbitals with the ligand. The valence space of these systems is more akin to atomic $4f$-orbitals, and like their atomic counterparts, the electronic structure of these complexes is dominated by spin-orbit J-multiplets, that are only weakly split by electronic interaction with the ligand field [5,22]. As a consequence, lanthanide based SMMs feature a large magnetic anisotropy arising from the crystal field splitting of the large unquenched angular momentum states in the ground multiplet.

Due to the typical over-parametrization afflicting phenomenological crystal field theory models [5, 70], nowadays the ab initio calculations of the crystal field energy levels of lanthanide complexes play an important role in the interpretation of the experimental results. Among the various available ab initio approaches, the Complete Active Space Self-Consistent Field with Restricted Active Space State Interaction via Spin-Orbit coupling (CASSCF/RASSI-SO) method has been successfully used in the literature to compute the magnetic properties of the lanthanide complexes [44, 45, 71]. Such a method involves converging a set of molecular orbitals (MO) for each spin configuration in the CASSCF step. Then diagonalizing the Spin-Orbit Coupling (SOC) operator over the basis of the CASSCF wavefunctions. This is the method of choice in the popular package MOLCAS [42], and it has extensively used to simulate the magnetic properties of lanthanide-based systems.

Recently, an alternative strategy has been proposed by us [41, 48], were a set of MO are optimized by minimizing the average-energy functional represented on the basis of all the possible CI configurations, which is called Configuration Averaged Hartree Fock (CAHF) method [41, 46, 72]. The optimizations of the MO and CI coefficients are then decoupled, and the latter coefficients are determined in a second step by direct diagonalization of the total Hamiltonian within the Complete Active Space Configuration Interaction with Spin-Orbit coupling (CASCI-SO) method.

CAHF/CASCI-SO method has been shown to produce consistent results with CASSCF/RASSI-SO approach with a significant saving in computational time, and it has been implemented into the Computational Emulator of Rare Earth Systems (CERES) quantum chemistry package [49], an ad hoc tool specifically designed for the calculation of the electronic structure and magnetic properties of lanthanide complexes.

In this study, we focus our attention on the SOC operator, which enters the CASCI-SO step. Spin-orbit interaction plays an important role in the case of lanthanide complexes. It causes the splitting and mixing of the atomic terms. The SOC Hamiltonians arise naturally from the reduction of the Dirac equation and its many electron extensions to two components theory [51]. This reduction can be achieved in many different ways, and the most renowned spin-orbit Hamiltonian thus achieved is the Breit-Pauli Hamiltonian [73], including both a one-electron (1e-SOC) term, and a two-electron (2e-SOC) term. However, the Breit-

Pauli operator is quite complex, and different approximations are often used in the literature [74]. While many studies have been published on the performances of the different SOC approximations in the accurate modeling of spectroscopic transitions in organic molecules and inorganic complexes, including inter-multiplet transitions in lanthanide systems [58,74–77], to our knowledge we present here the first extensive comparison of the performance of different approximations to the full Breit-Pauli Hamiltonian in the calculation of the crystal field splitting of the ground multiplets of lanthanide complexes, i.e. of their magnetic excitations.

Moreover, two of us have recently presented a new development that makes the evaluation of all the two-electron integrals entering the the Breit-Pauli Hamiltonian more efficient by the use of the Cholesky decomposition technique [50]. The aim of this work is then to (i) introduce working equations for the use of the Cholesky representation of the 2e-SOC integrals within the Breit-Pauli Hamiltonian and various mean-field approximations to it, (ii) apply our developments to the explicit ab initio calculation of the crystal field levels in a family of Ln(III) complexes, and finally (iii) compare the performances of the bare 1e-SOC and different mean-field approximations to the spin-orbit coupling Hamiltonian with respect to that of the full Breit-Pauli Hamiltonian, via a detailed analysis of the ensuing errors affecting the crystal field energy levels in the lowest energy multiplets for a series of Ln(III) complexes.

3.2 Spin-Orbit Coupling Hamiltonian

The Breit-Pauli spin-orbit Hamiltonian in atomic units for a system of N_e electrons and N_n nuclei has form [51, 73, 78–80]:

$$\begin{aligned}\mathcal{H}_{\mathrm{SO}}^{\mathrm{BP}} &= \mathcal{H}_{\mathrm{SO}}^{(1)} + \mathcal{H}_{\mathrm{SO}}^{(2)} \\ &= \frac{\alpha^2}{2} \sum_{i}^{N_e} \sum_{I}^{N_n} \frac{Z_I}{|\mathbf{r}_i - \mathbf{R}_I|^3} \hat{\mathbf{l}}_{iI} \cdot \hat{\mathbf{s}}_i - \frac{\alpha^2}{2} \sum_{i}^{N_e} \sum_{j \neq i}^{N_e} \frac{1}{|\mathbf{r}_i - \mathbf{r}_j|^3} \hat{\mathbf{l}}_{ij} \cdot (\hat{\mathbf{s}}_i + 2\hat{\mathbf{s}}_j)\end{aligned} \tag{3.1}$$

where $\alpha = c^{-1}$ is the fine structure constant with c speed of light, $\hat{\mathbf{l}}_{iI} = (\hat{\mathbf{r}}_i - \mathbf{R}_I) \times \hat{\mathbf{p}}_i$ is the angular momentum of the i-th electron relative to the I-th nucleus at position $\mathbf{R}_I$ with charge Z_I, and $\hat{\mathbf{l}}_{ij} = (\hat{\mathbf{r}}_i - \hat{\mathbf{r}}_j) \times \hat{\mathbf{p}}_i$ the angular momentum of the i-th electron relative to the j-th electron, with $\hat{\mathbf{r}}_i$ and $\hat{\mathbf{p}}_i$ position and momentum vector operators. Finally, $\hat{\mathbf{s}}_i$ is the spin operator of the i-th electron. The one-electron operator $\mathcal{H}_{\mathrm{SO}}^{(1)}$

represents the interaction of the spin magnetic moment of the electron i with the magnetic moment that arises from its orbiting in the Coulomb field of the nucleus I. The two-electron $\mathcal{H}_{\rm SO}^{(2)}$ includes two parts: (i) the terms which have factor $\hat{\mathbf{s}}_i$, representing the spin-orbit coupling of electron i in the Coulomb field of electron j, called spin-same-orbit (SSO) terms, and (ii) the terms which have factor $\hat{\mathbf{s}}_j$, representing the coupling between the spin magnetic moment of electron i and the orbital magnetic moment of electron j and vice versa, called spin-other-orbit (SOO) terms. Note that the two-electron term can be also written as:

$$\mathcal{H}_{\rm SO}^{(2)} = -\frac{\alpha^2}{2} \sum_{i}^{N_e} \sum_{j \neq i}^{N_e} \frac{1}{|\mathbf{r}_i - \mathbf{r}_j|^3} \left(\hat{\mathbf{l}}_{ij} + 2\,\hat{\mathbf{l}}_{ji} \right) \cdot \hat{\mathbf{s}}_i \tag{3.2}$$

From now on let us use $\psi_a(\mathbf{x}) = \phi_a(\mathbf{r})\eta_a$ to indicate a single electron molecular spin-orbital, with spatial part $\phi_a(\mathbf{r})$ and spin η_a ($= \alpha$ or β), and define the 1e-SOC and the 2e-SOC integrals on the spatial coordinates as:

$$(\phi_a \mid \mathbf{g} \mid \phi_b) = \frac{\alpha^2}{2} \left\langle \phi_a(1) \left| \sum_I \frac{Z_I\, \hat{\mathbf{l}}_{1I}}{|\mathbf{r}_1 - \mathbf{R}_I|^3} \right| \phi_b(1) \right\rangle \tag{3.3}$$

and:

$$\begin{aligned} &(\phi_a\phi_b \mid \mathbf{g} \mid \phi_c\phi_d) \\ &= -\frac{\alpha^2}{2} \left\langle \phi_a(1)\phi_c(2) \left| \frac{\hat{\mathbf{l}}_{12}}{|\mathbf{r}_1 - \mathbf{r}_2|^3} \right| \phi_b(1)\phi_d(2) \right\rangle \\ &= -\frac{\alpha^2}{2} \left\langle \phi_c(1)\phi_a(2) \left| \frac{\hat{\mathbf{l}}_{21}}{|\mathbf{r}_1 - \mathbf{r}_2|^3} \right| \phi_d(1)\phi_b(2) \right\rangle \end{aligned} \tag{3.4}$$

The 2e-SOC integrals have symmetry:

$$\begin{aligned} (\phi_a\phi_b \mid \mathbf{g} \mid \phi_c\phi_d) &= \quad 0 && \text{if} \quad a = b \\ &= \quad (\phi_a\phi_b \mid \mathbf{g} \mid \phi_d\phi_c) \\ &= -(\phi_b\phi_a \mid \mathbf{g} \mid \phi_c\phi_d) \\ &= -(\phi_b\phi_a \mid \mathbf{g} \mid \phi_d\phi_c) \\ &\neq \quad (\phi_c\phi_d \mid \mathbf{g} \mid \phi_a\phi_b) \end{aligned} \tag{3.5}$$

As usual when dealing with the CI approach, more direct developments rely on the second quantization formalism [47, 63, 81]. In second quantization, $\mathcal{H}_{\rm SO}^{\rm BP}$ has form [75, 82]:

$$\begin{aligned}\mathcal{H}_{\rm SO}^{\rm BP} = &\sum_{ab} (\phi_a \mid \mathbf{g} \mid \phi_b) \cdot \mathbf{T}_{ab} \\ &+ \sum_{abcd} \Big[(\phi_a\phi_b \mid \mathbf{g} \mid \phi_c\phi_d) + 2 (\phi_c\phi_d \mid \mathbf{g} \mid \phi_a\phi_b) \Big] \\ &\cdot \Big(\mathbf{T}_{ab} E_{cd} - \delta_{bc} \mathbf{T}_{ad} \Big) \end{aligned} \tag{3.6}$$

where $E_{cd}/\mathbf{T}_{ab}$ are the singlet/triplet excitation operators:

$$E_{cd} = a^+_{c\alpha} a_{d\alpha} + a^+_{c\beta} a_{d\beta} \tag{3.7}$$

$$T^x_{ab} = \frac{1}{2} \Big(a^+_{a\alpha} a_{b\beta} + a^+_{a\beta} a_{b\alpha} \Big) \tag{3.8}$$

$$T^y_{ab} = \frac{1}{2i} \Big(a^+_{a\alpha} a_{b\beta} - a^+_{a\beta} a_{b\alpha} \Big) \tag{3.9}$$

$$T^z_{ab} = \frac{1}{2} \Big(a^+_{a\alpha} a_{b\alpha} - a^+_{a\beta} a_{b\beta} \Big) \tag{3.10}$$

with $a^+_{cs_c}/a_{cs_c}$ creation/annihilation operator of an electron in the spin-orbital ψ_c, with spatial part ϕ_c and spin η_c.

Within all the CI methods, the molecular orbitals are partitioned in two main groups: (i) one set collecting the N_i orbitals that are doubly occupied in all the configurations, called inactive orbitals, (ii) the second set collecting the N_a orbitals which allow for an occupation number from 0 to 2, called active orbitals. Pointing out that the operator $\mathbf{T}_{ab}$ can not connect two doubly occupied orbitals, the Hamiltonian in eq. (3.6) can be re-written making explicit the non-null terms as:

$$\mathcal{H}_{\rm SO}^{\rm BP} = \sum_{ab}^{N_a} h_{ab} \cdot \mathbf{T}_{ab} + \sum_{abcd}^{N_a} \Big[(\phi_a\phi_b \mid \mathbf{g} \mid \phi_c\phi_d) + 2 (\phi_c\phi_d \mid \mathbf{g} \mid \phi_a\phi_b) \Big] \cdot \mathbf{T}_{ab} E_{cd} \tag{3.11}$$

where now a and b indices run just on the active set of orbitals, and

$$h_{ab} = (\phi_a \mid \mathbf{g} \mid \phi_b) + F^{\rm I}_{ab} + F^{\rm A}_{ab} \tag{3.12}$$

$F^{\rm I}_{ab}$ term in the previous equation has form:

$$F^{\rm I}_{ab} = \sum_{e}^{N_i} \Big[2 (\phi_a\phi_b \mid \mathbf{g} \mid \phi_e\phi_e) - 3 (\phi_a\phi_e \mid \mathbf{g} \mid \phi_e\phi_b) - 3 (\phi_e\phi_b \mid \mathbf{g} \mid \phi_a\phi_e) \Big] \tag{3.13}$$

and it represents the interaction between the electrons sitting in the active orbitals and the mean field generated by the electrons sitting in the inactive orbitals, than it is the analogue of the Fock matrix for the Coulomb interactions [75,81]. F^{A}_{ab} term in eq. (3.12) is given by:

$$F^{\mathrm{A}}_{ab} = -\sum_{c}^{N_a}\Big[(\,\phi_a\phi_c\;|\,\mathbf{g}\,|\;\phi_c\phi_b\,) + 2\,(\,\phi_c\phi_b\;|\,\mathbf{g}\,|\;\phi_a\phi_c\,)\Big] \tag{3.14}$$

3.3 Cholesky representation

The integrals entering eq. (3.11) are usually evaluated by expanding the functions ϕ_a on a set of N_{AO} atomic basis functions $\{\varphi_a\}$:

$$\phi_a(\mathbf{r}) = \sum_{\mu}^{N_{\mathrm{AO}}} c_{\mu a}\varphi_\mu(\mathbf{r}) \tag{3.15}$$

Here come the intense computational effort of a molecular calculation which aims to include explicitly both the $\mathcal{H}^{(1)}_{\mathrm{SO}}$ and $\mathcal{H}^{(2)}_{\mathrm{SO}}$ term in eq. (3.1), that is the evaluation of all the 2e-SOC integrals in atomic orbitals (AO) basis, and their transformations to the molecular orbitals (MO) basis:

$$(\,\phi_a\phi_b\;|\,g_\alpha\,|\;\phi_c\phi_d\,) = \sum_{\mu\nu\tau\kappa}^{N_{\mathrm{AO}}} c_{\mu a}c_{\nu b}c_{\kappa c}c_{\tau d}\,(\,\varphi_\mu\varphi_\nu\;|\,g_\alpha\,|\;\varphi_\kappa\varphi_\tau\,) \tag{3.16}$$

Different approximations have been proposed in the literature to reduce the time needed for SOC integrals evaluation [58, 74, 83]. We propose here a new approach, which allows for significant speed ups of the calculations without loss of accuracy. This can achieved by the use of the Cholesky representation for the 2e-SOC integrals recently presented in the literature by some of us [50]:

$$\begin{aligned}
&(\,\varphi_\mu\varphi_\nu\;|\,g_\alpha\,|\;\varphi_\kappa\varphi_\tau\,)\\
&= \frac{-i\alpha^2}{2}\varepsilon_{\alpha\beta\gamma}\Big[(\,\varphi_\mu\nabla_\gamma\varphi_\nu\;|\,\nabla_\beta\varphi_\kappa\varphi_\tau\,) + (\,\varphi_\mu\nabla_\gamma\varphi_\nu\;|\,\varphi_\kappa\nabla_\beta\varphi_\tau\,)\Big]\\
&\approx \frac{-i\alpha^2}{2}\sum_{J}^{N_{\mathrm{CH}}}\Big([L^\gamma_{\mu\nu}]^J[L^\beta_{\tau\kappa}]^J + [L^\gamma_{\mu\nu}]^J[L^\beta_{\kappa\tau}]^J\Big)
\end{aligned} \tag{3.17}$$

where $\varepsilon_{\alpha\beta\gamma}$ is the Levi-Civita symbol, $(\,\varphi_\mu\varphi_\nu\;|\,\varphi_\kappa\varphi_\tau\,)$ is an Coulomb electron repulsion integral (ERI), and $[L^\gamma_{\mu\nu}]^J$ is an element of the J-th Cholesky vector in AO basis. N_{CH} the dimension of the Cholesky basis, i.e. the number of the Cholesky vectors. In ref. [50], we showed that chosen the Cholesky δ threshold, the errors

Δ_{SOC} affecting the integrals evaluated by eq. (3.17) is always $\Delta_{\mathrm{SOC}} \leq 2\delta$. Then, the 2e-SOC integrals in MO basis can be expressed on the Cholesky basis by substituting eq. (3.17) into eq. (3.16):

$$
\begin{aligned}
&(\phi_a\phi_b \mid g_\alpha \mid \phi_c\phi_d) \\
&= \sum_{\mu\nu\tau\kappa}^{N_{\mathrm{AO}}} c_{\mu a}c_{\nu b}c_{\kappa c}c_{\tau d} (\varphi_\mu\varphi_\nu \mid g_\alpha \mid \varphi_\kappa\varphi_\tau) \\
&= \frac{-i\alpha^2}{2}\varepsilon_{\alpha\beta\gamma} \sum_{\mu\nu\tau\kappa}^{N_{\mathrm{AO}}} c_{\mu a}c_{\nu b}c_{\kappa c}c_{\tau d} \\
&\qquad \Big[(\varphi_\mu\nabla_\gamma\varphi_\nu \mid \nabla_\beta\varphi_\kappa\varphi_\tau) + (\varphi_\mu\nabla_\gamma\varphi_\nu \mid \varphi_\kappa\nabla_\beta\varphi_\tau) \Big] \\
&\approx \frac{-i\alpha^2}{2}\varepsilon_{\alpha\beta\gamma} \sum_{J}^{N_{\mathrm{CH}}} \Big([L^\gamma_{ab}]^J [L^\beta_{dc}]^J + [L^\gamma_{ab}]^J [L^\beta_{cd}]^J \Big)
\end{aligned}
\tag{3.18}
$$

where $[L^\gamma_{ab}]^J \neq [L^\gamma_{ba}]^J$ is an element of the J-th Cholesky vector transformed in the MO basis:

$$
[L^\gamma_{ab}]^J = \sum_{\mu\nu}^{N_{\mathrm{AO}}} c_{\mu a}[L^\gamma_{\mu\nu}]^J c_{\nu b} \tag{3.19}
$$

Moreover, the term in eq. (3.13) on AO basis reads:

$$
F^{\mathrm{I}}_{ab} = \sum_{\mu\nu}^{N_{\mathrm{AO}}} c_{\mu a}c_{\nu b}F_{\mu\nu} \tag{3.20}
$$

where:

$$
\begin{aligned}
F_{\mu\nu} = \sum_{\kappa\tau}^{N_{\mathrm{AO}}} D_{\kappa\tau} \Bigg[&(\varphi_\mu\varphi_\nu \mid \mathbf{g} \mid \varphi_\kappa\varphi_\tau) \\
&- \frac{3}{2} (\varphi_\mu\varphi_\kappa \mid \mathbf{g} \mid \varphi_\tau\varphi_\nu) - \frac{3}{2} (\varphi_\tau\varphi_\nu \mid \mathbf{g} \mid \varphi_\mu\varphi_\kappa) \Bigg]
\end{aligned}
\tag{3.21}
$$

and $D_{\kappa\tau}$ is an element of the molecular density $\mathbf{D}$ for the inactive electrons in AO basis:

$$
D_{\kappa\tau} = 2\sum_{c}^{N_i} c_{\kappa c}c_{\tau c} \tag{3.22}
$$

By the use of the Cholesky representation for the 2e-SOC integrals, $F_{\mu\nu}$ becomes:

$$
\begin{aligned}
F_{\mu\nu} \approx & -\frac{i\alpha^2}{2}\varepsilon_{\alpha\beta\gamma}\sum_{J}^{N_{\mathrm{CH}}}\sum_{\kappa\tau}^{N_{\mathrm{AO}}} D_{\kappa\tau} \\
& \Bigg[[L^{\gamma}_{\mu\nu}]^J\Big([L^{\beta}_{\kappa\tau}]^J + [L^{\beta}_{\tau\kappa}]^J\Big) \\
& \quad -\frac{3}{2}\Big([L^{\gamma}_{\mu\kappa}]^J[L^{\beta}_{\nu\tau}]^J + [L^{\gamma}_{\tau\nu}]^J[L^{\beta}_{\kappa\mu}]^J\Big)\Bigg] \\
= & -\frac{i\alpha^2}{2}\varepsilon_{\alpha\beta\gamma}\sum_{J}^{N_{\mathrm{CH}}}\Bigg[[L^{\gamma}_{\mu\nu}]^J\sum_{\kappa\tau}^{N_{\mathrm{AO}}} D_{\kappa\tau}\Big([L^{\beta}_{\tau\kappa}]^J + [L^{\beta}_{\kappa\tau}]^J\Big) \\
& \quad -3\sum_{c}^{N_i}\Big([K^{\gamma}_{\mu c}]^J[K^{\beta}_{\nu c}]^J + [K^{\gamma}_{c\nu}]^J[K^{\beta}_{c\mu}]^J\Big)\Bigg]
\end{aligned}
\tag{3.23}
$$

where $[K^{\gamma}_{\mu c}]^J \neq [K^{\gamma}_{c\mu}]^J$ are the semi-transformed Cholesky vectors:

$$
[K^{\gamma}_{\mu c}]^J = \sum_{\kappa}^{N_{\mathrm{AO}}}[L^{\gamma}_{\mu\kappa}]^J c_{\kappa c} \tag{3.24}
$$

$$
[K^{\gamma}_{c\mu}]^J = \sum_{\kappa}^{N_{\mathrm{AO}}}[L^{\gamma}_{\kappa\mu}]^J c_{\kappa c} \tag{3.25}
$$

Thus, the computation and use of the spin-orbit Hamiltonians implemented in CERES includes five steps: (i) evaluation and storage of the Cholesky representation for the 2e-SOC integrals as presented in ref. [50], (ii) evaluation of F^{I}_{ab} in eq. (3.11) by direct contraction of the inactive density matrix with the Cholesky vectors (eq. (3.23)) and transformation on the molecular basis (iii) transformation of the Cholesky vectors on the molecular basis within the chosen active space and construction of the 2e-SOC integrals (iv) evaluation of the effective one-electron integrals in eq. (3.12) via eq. (3.14) (v) update and diagonalization of the CI-SOC matrix.

The proposed approach allows the following advantages: (i) rigorous evaluation of the most important contributions for 2e-SOC integrals, (ii) full control on the needed accuracy by the choice of the unique Cholesky δ threshold, and (iii) the one-off calculation and the storage of the smallest amount of data needed to numerically represent all the 2e-SOC integrals with absolute accuracy smaller than 2δ, which are then readily available for transformations as in eqs. (3.18) and (3.23) (this can be really favourable within the self-consistent approaches which include the SOC contribution in the iterative procedure).

A complete analysis of the Cholesky Decomposition to the full Breit-Pauli operator has been done previously [50], where it was tested for a lanthanide complex of Dysprosium [$Dy(acac)_3(H_2O)_2$] across different basis sets. It was seen that in the case of a SARC2 basis set for $\delta = 10^{-4},\ to\ 10^{-8}$ the cholesky decomposition took less than 22% of the time required by a direct calculation of the Breit-Pauli Hamiltonian. In the case of a generally decomposed ANO-RCC basis for a $\delta = 10^{-4},\ 10^{-6}\ and\ 10^{-8}$ the time spent was 50%, 60% and 86% respectively of the direct computation.

3.4 Spin-Orbit Mean Field

To avoid dealing explicitly with the 2e-SOC terms during the evaluation of the elements for the CI matrix, in the literature it is often used the mean field (MF) approximation. The latter is based on two assumptions:

1. the second term in the right-hand side of eq. (3.11) and F^{A}_{ab} term in eq. (3.12) are ignored. This reduces $\mathcal{H}^{\mathrm{BP}}_{\mathrm{SO}}$ to an effective one-electron operator on the MO basis;

2. the two-electron interactions within the active space are accounted for in an mean field approach within the F^{I}_{ab} term in eq. (3.12).

Under these simplifications, eq. (3.11) reduces to:

$$\mathcal{H}^{\text{BP-MF}}_{\mathrm{SO}} = \sum_{ab}^{N_a} \Big[(\ \phi_a\ |\, \mathbf{g}\, |\ \phi_b\ ) + F^{\mathrm{MF}}_{ab} \Big] \cdot \mathbf{T}_{ab} \tag{3.26}$$

with:

$$\begin{aligned} F^{\mathrm{MF}}_{ab} = \sum_{c}^{N_e} \frac{n_c}{2} \Bigg[& (\ \phi_a\phi_b\ |\, \mathbf{g}\, |\ \phi_c\phi_c\ ) \\ & - \frac{3}{2} (\ \phi_a\phi_c\ |\, \mathbf{g}\, |\ \phi_c\phi_b\ ) - \frac{3}{2} (\ \phi_c\phi_b\ |\, \mathbf{g}\, |\ \phi_a\phi_c\ ) \Bigg] \end{aligned} \tag{3.27}$$

In the previous equation, n_c is the occupation number of the orbital ϕ_c ($n_c = 2$ for an inactive orbital, $n_c = n^{\mathrm{el}}_a/N_a$ for an active orbital, with n^{el}_a the number of active electrons), and now the index c runs over all the complete set of N_e molecular orbitals.

Also within the MF approximation, the 2e-SOC integrals can be efficiently evaluated by the use of their Cholesky representation:

$$F_{\mu\nu}^{\mathrm{MF}} \approx -\frac{i\alpha^2}{2}\varepsilon_{\alpha\beta\gamma}\sum_{J}^{N_{\mathrm{CH}}}\Bigg[[L_{\mu\nu}^{\gamma}]^{J}\sum_{\kappa\tau}^{N_{\mathrm{AO}}}D_{\kappa\tau}\Big([L_{\tau\kappa}^{\beta}]^{J}+[L_{\kappa\tau}^{\beta}]^{J}\Big) - \frac{3}{2}\sum_{c}^{N_e}n_c\Big([K_{\mu c}^{\gamma}]^{J}[K_{\nu c}^{\beta}]^{J}+[K_{c\nu}^{\gamma}]^{J}[K_{c\mu}^{\beta}]^{J}\Big)\Bigg] \tag{3.28}$$

with now:

$$D_{\kappa\tau} = \sum_{c}^{N_e} n_c c_{\kappa c} c_{\tau c} \tag{3.29}$$

3.5 The Atomic Approximation

Although the $\mathcal{H}_{\mathrm{SO}}^{\text{BP-MF}}$ operator in eq. (3.26) defines an effective one-electron operator, the number of atomic spin-orbit integrals which must be calculated it is not reduced if the Cholesky representation is not used. A widely used approximation used in the literature to reduce the computational effort is to restrict to calculation of the two-electron integrals on the AO basis to comprise only the one-center terms. This methodology is based on the assumption that the spin-orbit two-electron operator is a short-range operator, which can be justified by the presence of $1/|\mathbf{r}_i - \mathbf{r}_j|^3$ terms in $\mathcal{H}_{\mathrm{SO}}^{\mathrm{BP}}$. This is called the atomic approximation.

Moreover, the development that has gained larger popularity in the literature is the atomic mean field implementation (AMFI) proposed by Hess and Schimmelpfennig [58,60], where the $\mathcal{H}_{\mathrm{SO}}^{\text{BP-MF}}$ operator is used together with two additional approximations: (i) only one-center integrals are retained throughout, and (ii) the molecular orbitals ϕ_a in eq. (3.27) are replaced by atomic self-consistent field (SCF) orbitals obtained from spherically averaged atomic SCF calculations with predetermined valence shell occupations rather than using the complete non-spherical molecular density. While the combination of these approximations reduces the time needed for the SOC integrals evaluation to a negligible amount, it has been shown that the inclusion of all the significant multicenters two-electron SOC integrals is of primary importance to achieve a good accuracy [74].

In this work, we study how the atomic approximation affects the energy levels when applied to both

$\mathcal{H}_{\rm SO}^{\rm BP}$, and $\mathcal{H}_{\rm SO}^{\rm BP\text{-}MF}$ operators. In both cases, the density used in our SOC atomic calculations is always from the true molecular density, optimized at CAHF level on the whole system.

3.6 Computational Methods

CAHF/CASCI-SO calculations were carried out on a set of Ln(III) complexes to analyze how different approximations for $\mathcal{H}_{\rm SO}^{\rm BP}$ Hamiltonian affect the energy gaps of the lowest energy spin-orbit multiplets.

In CAHF/CASCI-SO strategy [41, 48], at first the CAHF method is used to generate the set of ϕ_a molecular orbitals which minimizes the average-energy functional represented on the basis of all possible Slater determinants, of any M_S quantum number, built up allowing $n_a^{\rm el}$ active electrons to be distributed in all the possible ways in N_a active orbitals. Then, in the CASCI-SO step, the CAHF orbitals are used to construct the representation of the total Hamiltonian of the system, which includes both the Born-Oppenheimer electrostatic and spin-orbit Hamiltonian, still on the basis of all possible Slater determinants in the CAS space of $n_a^{\rm el}$ electrons in N_a orbitals. Finally, the total Hamiltonian is diagonalized to obtain the energy levels.

The number $N_a = 7$ active orbitals have been used for all the Ln ions studied (i.e. $4f$ atomic shell), and the number $n_a^{\rm el} = 2, 3, 5, 6, 7, 8, 9, 10, 11, 12, 13$ active electrons for Pr(III), Nd(III), Sm(III), Eu(III), Gd(III), Tb(III), Dy(III), Ho(III), Er(III), Tm(III), Yb(III) ions, respectively.

The geometries of the Ln complexes analyzed have been fixed to their experimental X-ray structures taken from the literature. [59, 84–89] We indicate the ligands with acac = acetylacetonate, dppz = dipyridophenazine, dpq = dipyridoquinoxaline, phen = 1,10-phenanthroline, hfac = hexafluoroacetylacetonate, glyme = dimethoxyethane.

All atoms were described by the ANO-RCC basis set [90], with the contraction [8s7p5d3f2g1h] for Ln atoms, [4s3p2d1f] for O, [3s2p] for C and N, [2s] for H.

Scalar relativistic terms were included in the one-electron part of the electrostatic Hamiltonian both in the CAHF and CASCI-SO steps, within the second order Douglas-Kroll-Hess (DKH2) approximation [80].

Four different approximations to the Breit-Pauli Hamiltonian $\mathcal{H}_{\rm SO}^{\rm BP}$ were studied: (i) bare $\mathcal{H}_{\rm SO}^{(1)}$, (ii) $\mathcal{H}_{\rm SO}^{\rm MF}$ complete, (iii) atomic $\mathcal{H}_{\rm SO}^{\rm MF}$ (referred to as $\mathcal{H}_{\rm SO}^{\rm AMF}$), and atomic $\mathcal{H}_{\rm SO}^{\rm BP}$ (referred to as $\mathcal{H}_{\rm SO}^{\rm ABP}$). Note that the atomic approximation is applied just to $\mathcal{H}_{\rm SO}^{(2)}$ term, while $\mathcal{H}_{\rm SO}^{(1)}$ always include both one- and two-centers SOC integrals. The CASCI-SO energies within a given multiplet have been compared with the CASCI-SO results which include the true $\mathcal{H}_{\rm SO}^{\rm BP}$.

The Cholesky representation of the 2e-SOC integrals as proposed in this paper was used to speed up the calculations when the atomic approximation is not used. Different Cholesky δ thresholds have been tested at first to reach the best compromise between time performance and accuracy. It has been fixed at $\delta = 10^{-4}$, which shows a significant speed up in the calculations with a loss of accuracy on the energy gaps smaller than 0.01 cm^{-1} with respect to the results which include all the 2e-SOC integrals.

All the calculation were performed using the software package CERES [49], an ab initio quantum chemistry package specifically designed for the calculation of the electronic structure and magnetic properties of lanthanide complexes.

The errors affecting the energy gaps $\Delta E_i^{\rm APP} = E_i^{\rm APP} - E_0^{\rm APP}$, calculated within a given spin-orbit multiplet $M = {}^{(2S+1)}L_J$ by the use of the approximation APP, were analysed by the statistical indicators:

$$(\%\mathrm{error})_i^{\rm APP} = \frac{\Delta E_i^{\rm APP} - \Delta E_i^{\rm BENC}}{\Delta E_i^{\rm BENC}} \times 100 \tag{3.30}$$

$$\mu_M^{\rm APP} = \frac{\sum_{i=1}^{N} (\%\mathrm{error})_i^{\rm APP}}{N} \tag{3.31}$$

$$\sigma_M^{\rm APP} = \sqrt{\frac{\sum_{i=1}^{N} \left[(\%\mathrm{error})_i^{\rm APP} - \mu_M^{\rm APP}\right]^2}{N-1}} \tag{3.32}$$

$$\mathrm{MAE}_M^{\rm APP} = \frac{\sum_{i=1}^{N} |(\%\mathrm{error})_i^{\rm APP}|}{N} \tag{3.33}$$

where $\Delta E_i^{\rm BENC} = E_i^{\rm BENC} - E_0^{\rm BENC}$ are the energy gaps calculated by the use of the true $\mathcal{H}_{\rm SO}^{\rm BP}$, and N is the total number of states in the multiplet (minus one for the ground state in the ground spin-orbit multiplet). The results were graphically represented by the use of the probability density of the normal distribution:

$$P(\%\mathrm{error}; \mu, \sigma) = \frac{1}{\sqrt{2\pi}\sigma} e^{-(\%\mathrm{error}-\mu)^2/(2\sigma^2)} \tag{3.34}$$

For Dy(III) complexes, the principal values of the g tensor were calculated within the pseudo-spin $\tilde{S} = 1/2$

formalism as the square roots of the eigenvalues of the **G** matrix [23, 91]:

$$G_{\alpha\beta} = 2 \sum_{r,s=0,1} \langle \Psi_r \mid m_\alpha \mid \Psi_s \rangle \langle \Psi_s \mid m_\beta \mid \Psi_r \rangle \tag{3.35}$$

where $\mathbf{m} = \mathbf{L} + g_e\mathbf{S}$ is the magnetic moment, with $\mathbf{L} = \sum_i^{N_e} \mathbf{l}_{i\mathrm{Dy}}$ the total electronic angular momentum with respect to the position of the Dy(III) atom, $\mathbf{S} = \sum_i^{N_e} \mathbf{s}_i$ the total spin angular momentum, and g_e the magnetic g factor of the electron. The electronic wavefunctions Ψ_0 and Ψ_1 are a Kramers pair for the system at zero magnetic field. The three eigenvectors of **G** are the directions of the three principal magnetic axes.

3.7 Results and Discussion

The mean μ, standard deviation σ, and MAE for the %errors affecting the energy gaps within the lowest energy spin-orbit multiplet for Ln-acac$_3$-$(H_2O)_2$ complexes, estimated using different approximations to the Breit-Pauli Hamiltonian, are represented in Figure 3.1 (see also Table A.17 in Section A). In the following, MAE = $|\mu|$ if not explicitly reported.

The errors for $\mathcal{H}_{\mathrm{SO}}^{(1)}$ differ between the different ions. A quite large underestimation of the crystal field levels affects the results for Ho(III) ($\mu \approx -11\%$, $\sigma \approx 1\%$), while smaller deviations affect the results for Nd(III) ($\mu \approx -6\%$, $\sigma \approx 2\%$), Pr(III) ($\mu \approx -5\%$, $\sigma \approx 4\%$), and Dy(III) ($\mu \approx -4\%$, $\sigma \approx 1\%$). The energy gaps are well represented for Sm(III), Tb(III), Er(III), Tm(III), Yb(III) (μ within $\pm 1\%$ and $\sigma < 2\%$). As an indication of the magnitude of these errors, it has been shown in the literature that the discrepancies between the simulated ab initio and the experimental results can be larger than 10% [25, 92]. As an example, the ab initio crystal field levels in Er(III)-trensal reported in Table 2 of ref. [25] are affected by a MAE $\approx 19\%$ for CASSCF/RASSI-SO model A1 simulation, or MAE $\approx 8\%$ for RASSCF/CASPT2/RASSI-SO model C4, and in both models the ab initio gap between the ground and the first excited Kramers doublet, which is experimentally observed at 54 cm^{-1}, is affected by an error exceeding +13%.

$\mathcal{H}_{\mathrm{SO}}^{(1)}$ is not sufficient to describe the SO coupling within the spin-only ground multiplet $^8\mathrm{H}_{7/2}$ of Gd(III). Here, the crystal field levels calculated by $\mathcal{H}_{\mathrm{SO}}^{(1)}$ (ΔE = 1.2, 2.3, 4.3 cm^{-1}, see Table A.6) are largely overestimated with respect to the $\mathcal{H}_{\mathrm{SO}}^{\mathrm{BP}}$ results (ΔE = 0.3, 0.5, 1.0 cm^{-1}), leading to $\mu \approx +350\%$.

The 3σ (99.7% confidence) is smaller than 6% for almost all the ions in Figure 3.1, which indicates a systematic nature of the errors introduced by the bare $\mathcal{H}_{\mathrm{SO}}^{(1)}$ approximation. Pr(III) ($3\sigma \approx 12\%$) and Gd(III) ($3\sigma \approx 52\%$) show an higher degree of randomness.

A large improvement in the results is shown by $\mathcal{H}_{\mathrm{SO}}^{\mathrm{MF}}$, where the two-electron interactions are accounted for in a mean field approach. Here, μ never exceeds $\pm 1\%$ for all the ions, with very narrow picked normal distributions.

Similar errors are shown by both the atomic $\mathcal{H}_{\mathrm{SO}}^{\mathrm{AMF}}$ and $\mathcal{H}_{\mathrm{SO}}^{\mathrm{ABP}}$ approximations, where μ falls in the range $\pm 1\%$ for all the ions, with the exception of Gd(III). For the latter, the exclusion of the 2e-SOC multi-center integrals in the computation leads to a quite large underestimation of the energy gaps ($\Delta E = 0.2$, 0.5, and 0.8 cm^{-1}, $\mu \approx -12\%$). Within the atomic approximation, Ho(III), Er(III), and Tm(III) show the largest 3σ values ($3\sigma \approx 2.0\%$, 3.0% and 1.5%, respectively), while $3\sigma < 1.2\%$ for all the other metals. It is noteworthy that the use of the atomic approach does not introduce significant additional errors to the $\mathcal{H}_{\mathrm{SO}}^{\mathrm{MF}}$ results.

Next, we study the errors affecting the various approximations to the spin-orbit Hamiltonian in the calculation of the energy gap between ground and first excited multiplets. While due to lack of dynamical correlation in our approach these calculations would be of limited use to model experimental data, we are only interested here to estimate the typical error affecting spin-orbit Hamiltonians for the calculation of such energy gaps, as a term of comparison with that estimated for the ground multiplet magnetic excitations that are the focus of this study. The results are represented in Figure 3.2 (see Table A.17 in Section A). Here, the bare $\mathcal{H}_{\mathrm{SO}}^{(1)}$ fails completely, with a general overestimation of the crystal field gaps larger than +70% for all the ions but Gd(III). Differently, the $^6\mathrm{P}_{7/2}$ levels for Gd(III) are underestimated ($\Delta E = 35631$, 35687, 35728, 35822 cm^{-1} by $\mathcal{H}_{\mathrm{SO}}^{(1)}$ versus $\Delta E = 38742$, 38779, 38807, 38849 cm^{-1} by $\mathcal{H}_{\mathrm{SO}}^{\mathrm{BP}}$, with $\mu \approx -9\%$ and $\sigma \approx 0.1\%$).

On the other hand, $\mathcal{H}_{\mathrm{SO}}^{\mathrm{MF}}$ approximation leads to errors within the acceptable range $\pm 4\%$, with generally small standard deviations ($\sigma < 1\%$). As for the ground multiplets, $\mathcal{H}_{\mathrm{SO}}^{\mathrm{MF}}$ and $\mathcal{H}_{\mathrm{SO}}^{\mathrm{AMF}}$ approximations lead to very comparable results, and $\mathcal{H}_{\mathrm{SO}}^{\mathrm{ABP}}$ shows almost zero errors.

Overall, $\mathcal{H}_{\mathrm{SO}}^{\mathrm{ABP}}$ Hamiltonian turns out to be a very good compromise between computational saving

and accuracy in the evaluation of the energy gaps for both the ground (of large interest for the magnetic properties) and the first excited (of large interest for the spectroscopic properties) multiplets of Ln(III) complexes. On the other hand, $\mathcal{H}_{\rm SO}^{(1)}$ works quite well for the gaps within the ground multiplets, but it can not be used for the estimation of the gaps in the excited levels.

Eu(III) ion deserves a special consideration. The ground level of Eu(III) is the ^{7}F$_0$ singlet, and the gaps between the lowest energy multiplets ^{7}F$_J$, with $J = 1, 2, 3, 4, 5, 6$, are considerably small. CAHF/CASCI-SO[$\mathcal{H}_{\rm SO}^{\rm BP}$] computations on the isolated Eu^{3+} atom estimates the energy gaps within the ground Russell-Saunders term ^{7}F as $\Delta E = 369$, 1028, 1889, 2880, 3949, 5056 cm^{-1}, which are in a very good agreement with the observed values from spectroscopy $\Delta E = 370$, 1040, 1890, 2860, 3910, 4940 cm^{-1} (see Table A.1) [93]. On the isolated atom, $\mathcal{H}_{\rm SO}^{\rm MF}$ approximation slightly overestimates the levels gaps with respect to $\mathcal{H}_{\rm SO}^{\rm BP}$ Hamiltonian (+3.5%, +3.8%, +4.1%, +4.5%, +5.0%, +5.5% for ^{7}F$_1$, ^{7}F$_2$, ^{7}F$_3$, ^{7}F$_4$, ^{7}F$_5$, ^{7}F$_6$ levels, respectively).

The errors affecting the crystal field splittings for Eu-acac$_3$-(H$_2$O)$_2$ are represented in Figure 3.3. As found for the excited multiplets in the other ions, bare $\mathcal{H}_{\rm SO}^{(1)}$ leads to errors larger than +100%, while the SOC mean field Hamiltonian, both within and without the atomic approximation, shows errors similar to those affecting Eu^{3+} atom ($\mu \approx +5\%$), with small standard deviations (systematic errors) whereas the size of the statistical sample is not too small, that is, for the ^{7}F$_J$ levels with $J > 1$. It is noteworthy that $\mathcal{H}_{\rm SO}^{\rm ABP}$ accurately reproduces the true Breit-Pauli results for all the excited multiplets.

The data obtained varying the ligands' environment for a fixed central Dy(III) ion are represented in Figures 3.4 and 3.5 (see also Table A.18). We find that the %error is largely unaffected by the choice of the ligands for the gaps within both the ground and the first-excited multiplets. As observed in Figures 3.1 and 3.2 for Dy-acac$_3$-(H$_2$O)$_2$ complex, $\mathcal{H}_{\rm SO}^{(1)}$ approximation underestimate/overestimate the energy gaps within the ground/first-excited multiplets of about $-5\%/+100\%$ with respect to $\mathcal{H}_{\rm SO}^{\rm BP}$, while the SOC mean field approximation well reproduces the results for the ground ^{6}H$_{15/2}$ level, and slightly underestimates ($\mu \approx -3$) the gaps within the excited ^{6}H$_{13/2}$ level, for both the multi-center and one-center 2e-SOC integrals evaluations. $\mathcal{H}_{\rm SO}^{\rm ABP}$ leads to almost negligible errors in all cases.

We studied the errors affecting the g tensors, and the orientation of the corresponding principal magnetic

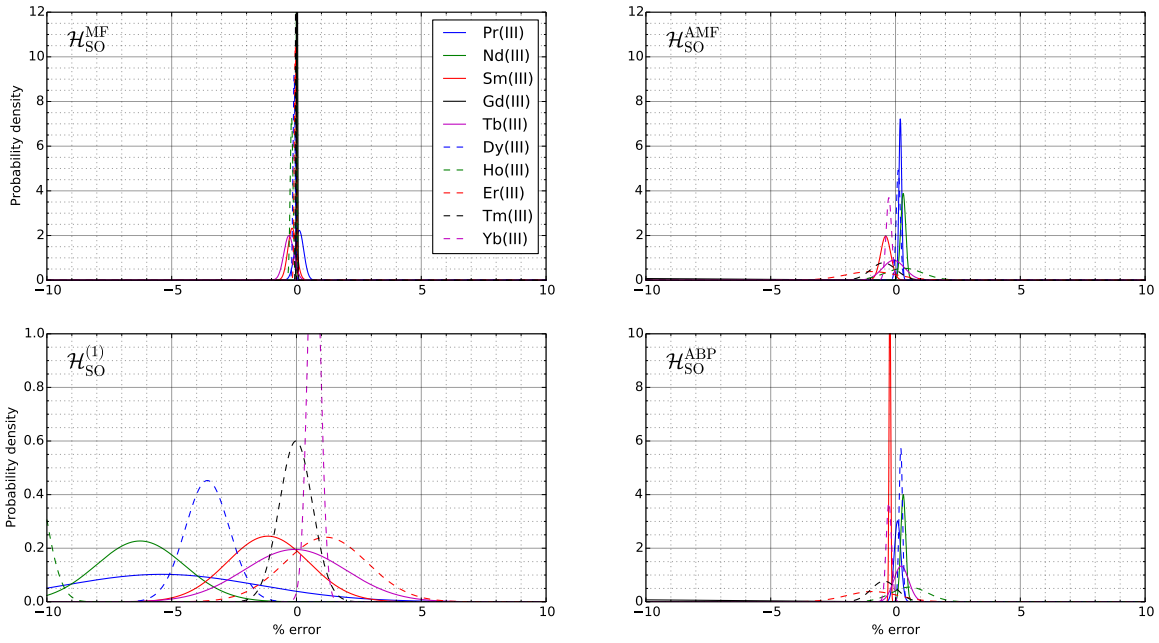

Figure 3.1: Graphical representation (by normal distribution function) of the mean μ and standard deviation σ for the %errors affecting the energy gaps within the ground spin-orbit multiplet for Ln-acac$_3$(H$_2$O)$_2$ complexes, estimated using different approximations for the SOC interaction with respect to the Breit-Pauli Hamiltonian (see Table A.17).

axes, for the ground Kramers doublets in the Dy(III) complexes, of large interest for the modelling for the magnetic behaviour of lanthanide-based SMM complexes. The g tensor values calculated by $\mathcal{H}_{SO}^{BP}$ present almost zero transversal g_x and g_y components, and g_z axial component of about 19.4, which is close to the value expected for a pure $M_J \pm 15/2$ Kramers doublet (i.e. 20), indicating a strong magnetic anisotropy, see Table 3.1.

All the SOC approximations well reproduce the strong axiality. $\mathcal{H}_{SO}^{(1)}$ leads to a very small underestimation on the g_z values of about -1.4%, with the corresponding principal magnetic axis tilted from the axis calculated by $\mathcal{H}_{SO}^{BP}$ of less than 1 degree in all Dy(III) systems. $\mathcal{H}_{SO}^{MF}$, $\mathcal{H}_{SO}^{AMF}$, and $\mathcal{H}_{SO}^{ABP}$ approximations present effective g values and principal magnetic axes orientations almost coincident with the results obtained by $\mathcal{H}_{SO}^{BP}$.

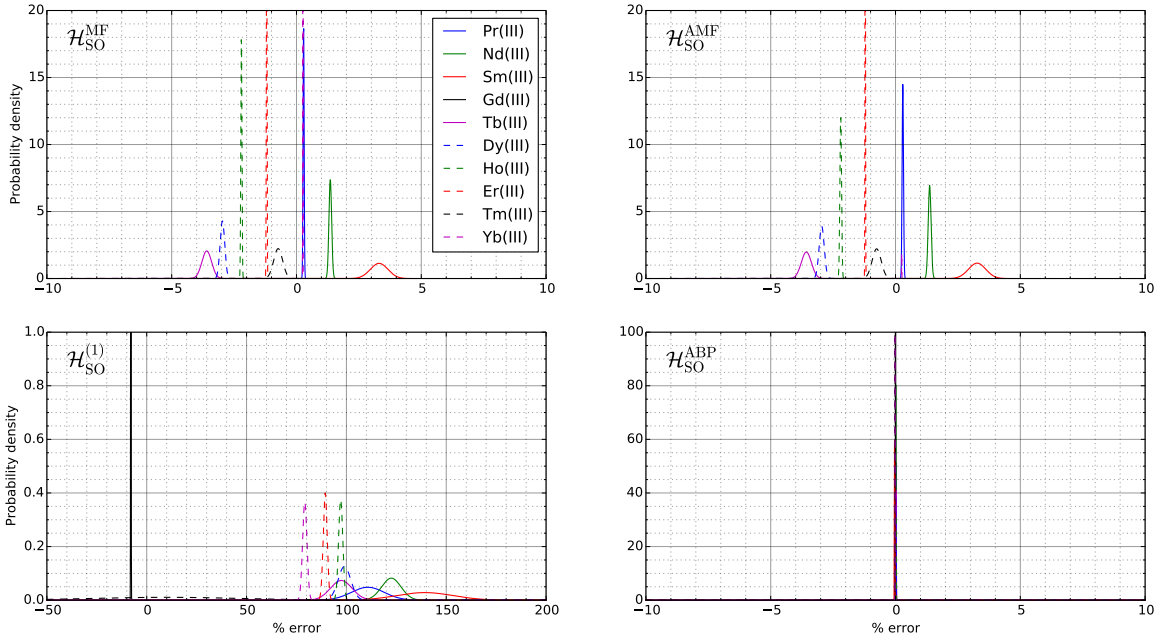

Figure 3.2: Graphical representation (by normal distribution function) of the mean μ and standard deviation σ for the %errors affecting the energy gaps within the first excited spin-orbit multiplet for Ln-acac$_3$-(H$_2$O)$_2$ complexes, estimated using different approximations for the SOC interaction with respect to the Breit-Pauli Hamiltonian (see Table A.18).

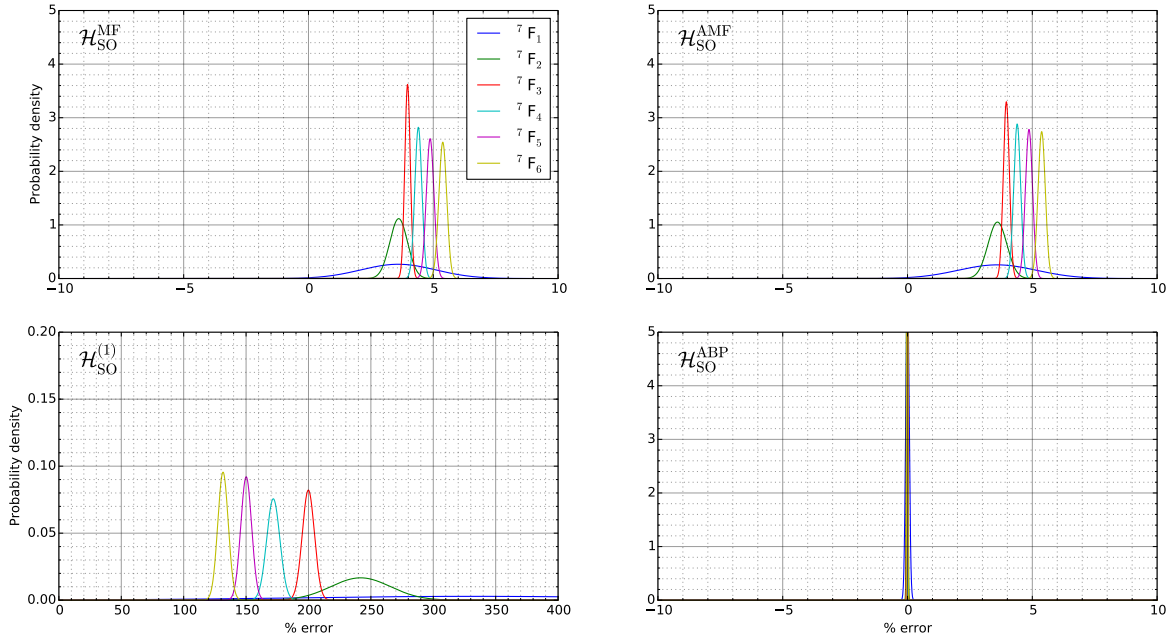

Figure 3.3: Graphical representation (by normal distribution function) of the mean μ and standard deviation σ for the %errors affecting the energy gaps within the lowest energy spin-orbit multiplets $^7\mathrm{F}_J$, with $J = 1, 2, 3, 4, 5, 6$, for Eu-acac$_3$-$(\mathrm{H_2O})_2$ complex, estimated using different approximations for the SOC interaction with respect to the Breit-Pauli Hamiltonian (see Table A.17).

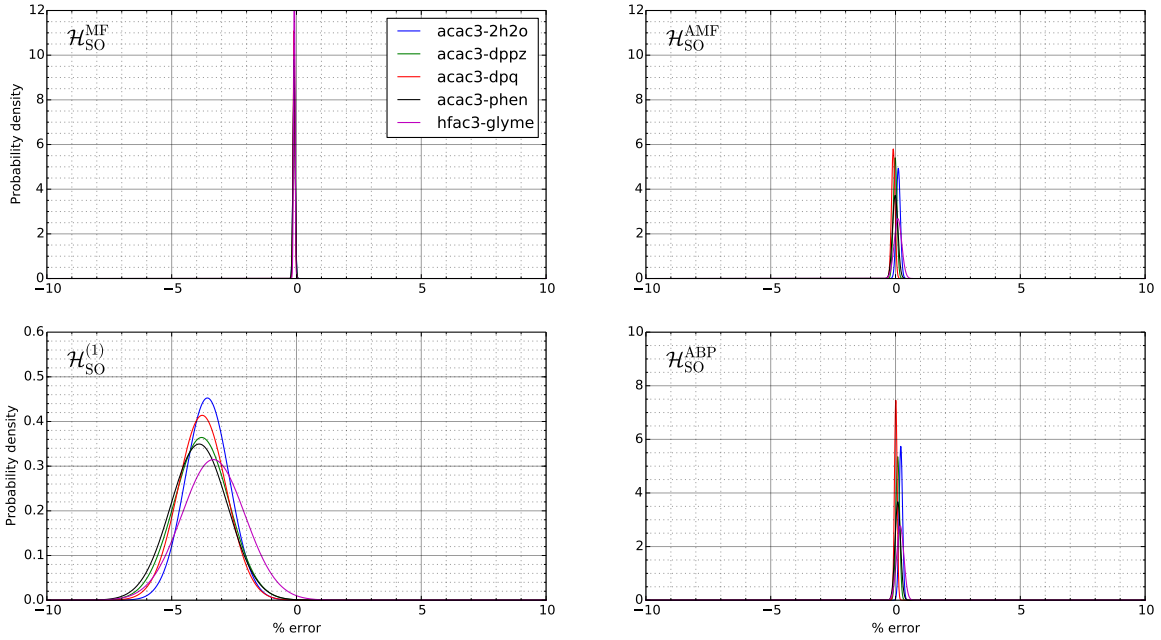

Figure 3.4: Graphical representation (by normal distribution function) of the mean μ and standard deviation σ for the %errors affecting the energy gaps within the ground spin-orbit multiplet $^6\mathrm{H}_{15/2}$ for Dy(III) complexes, estimated using different approximations for the SOC interaction with respect to the Breit-Pauli Hamiltonian (see Table A.18).

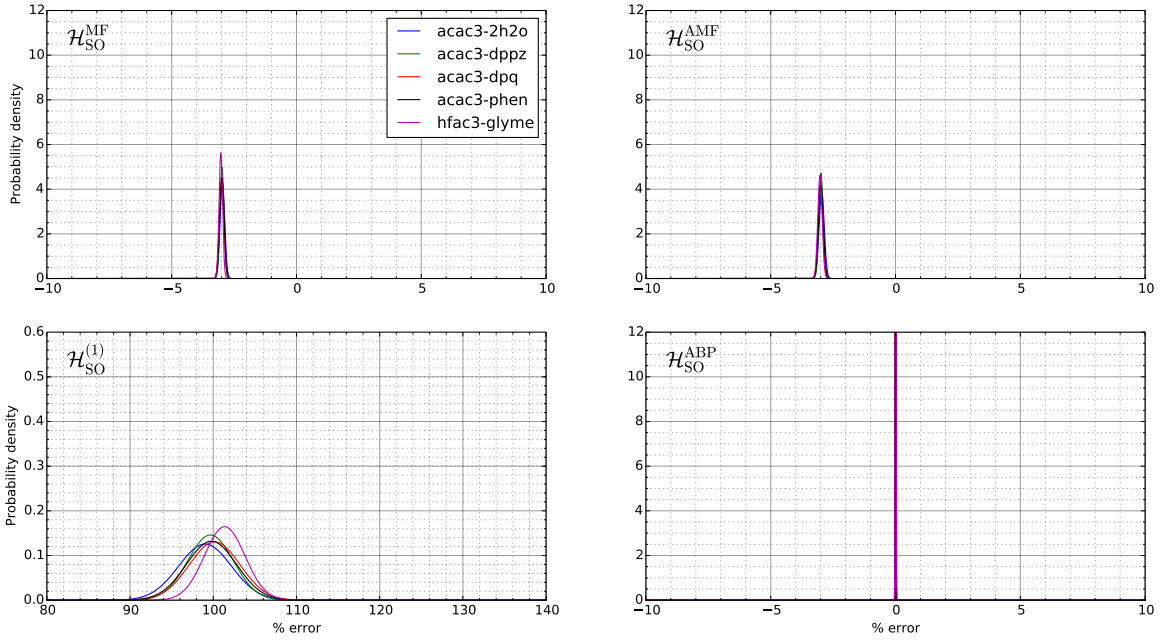

Figure 3.5: Graphical representation (by normal distribution function) of the mean μ and standard deviation σ for the % errors affecting the energy gaps within the first excited spin-orbit multiplet $^6H_{13/2}$ for Dy(III) complexes, estimated using different approximations for the SOC interaction with respect to the Breit-Pauli Hamiltonian (see Table A.18).

Table 3.1: g tensor values for the first Kramers doublet in Dy(III) complexes estimated using different approximations to SOC Hamiltonian with respect to the results obtained by inclusion of the true Breit-Pauli Hamiltonian contribution.

		$\mathcal{H}_{\mathrm{SO}}^{(1)}$	$\mathcal{H}_{\mathrm{SO}}^{\mathrm{MF}}$	$\mathcal{H}_{\mathrm{SO}}^{\mathrm{AMF}}$	$\mathcal{H}_{\mathrm{SO}}^{\mathrm{ABP}}$	$\mathcal{H}_{\mathrm{SO}}^{\mathrm{BP}}$
$acac_3$-$(H_2O)_2$	g_x	0.000	0.000	0.000	0.000	0.005
	g_y	0.000	0.000	0.000	0.000	0.007
	g_z	−0.282	−0.002	−0.001	+0.001	19.441
$acac_3$-dppz	g_x	−0.001	0.000	0.000	0.000	0.005
	g_y	−0.002	0.000	0.000	0.000	0.009
	g_z	−0.268	−0.002	+0.001	+0.003	19.363
$acac_3$-dpq	g_x	0.000	−0.000	0.000	0.000	0.006
	g_y	−0.004	−0.000	0.000	0.000	0.014
	g_z	−0.260	−0.001	0.000	+0.001	19.219
$acac_3$-phen	g_x	0.000	0.000	0.000	0.000	0.005
	g_y	0.000	0.000	0.000	0.000	0.007
	g_z	−0.263	−0.002	+0.002	+0.004	19.340
$hfac_3$-glyme	g_x	−0.002	0.000	0.000	0.000	0.006
	g_y	−0.004	0.000	0.000	0.000	0.010
	g_z	−0.255	−0.002	+0.003	+0.005	19.445

3.8 Conclusions

In this paper we investigated a number of approximations to the full Breit-Pauli spin-orbit coupling operator for the calculation of the ground multiplet crystal field levels and effective g tensors for lanthanide-based compounds within the CAHF/CASCI-SO ab initio method [41, 48].

After briefly reviewing the most widely used approximations to the SOC Hamiltonian in the literature, we presented an implementation of a new approach to the calculation of the 2e-SOC integrals which makes use of their Cholesky representation, which was recently proposed by some of us [50]. This novel method allows for significant speed ups without loss of accuracy, and it can be applied to the true Breit-Pauli Hamiltonian, as well as to its approximations. The novel approach has been implemented in the CERES package [48, 49].

Via extensive comparison of the computed crystal field energies for a family of lanthanide complexes that are of interest to achieve single molecule magnetism, we showed that the use of the bare one-electron SOC Hamiltonian $\mathcal{H}_{\mathrm{SO}}^{(1)}$ reproduces the crystal field split energies of the ground multiplets with almost systematic errors of about -13% to $+2\%$ for Pr(III), Nd(III), Sm(III), Tb(III), Dy(III), Ho(III), Er(III), Tm(III), and Yb(III), while the energy gaps are largely under-/over-estimated for Eu(III)/Gd(III) systems.

Among the approximations that aim to include part of the SOC two-electron interaction, the spin-orbit mean field approach almost completely reproduces the Breit-Pauli results for the ground multiplets, and remains within an error of $\pm 4\%$ for the energies of the first excited multiplets. For both the ground and the excited multiplets, we showed that the atomic approximation, where only the one-center 2e-SOC integrals are retained throughout, and contracted with the true CAHF molecular density, does not introduce additional errors with respect to the results where all the 2e-SOC integrals are evaluated. The errors are quite stable varying the ligands' environment for all the approximations studied.

In Dy(III) complexes, the effective g values for the ground Kramers doublet are reproduced with an error of about -1.4% for $\mathcal{H}_{\mathrm{SO}}^{(1)}$, while the discrepancies in the orientation of the principal magnetic axes are almost negligible. No differences in the g tensors are shown by the other approximations.

These results indicate the atomic approximation as the best compromise between computational saving and high accuracy for both the ground and the excited multiplets. On the other hand, surprisingly the simple

bare 1e-SOC Hamiltonian well reproduces the gaps within the lowest energy crystal field manifold for the main ions used in the literature for the design of the lanthanide-based SMMs (i.e. Dy, Tb, Er), with errors below 4% with respect to the evaluations made by the use of the complete Breit-Pauli Hamiltonian. Finally, it is noteworthy to mention that the g tensor for the lowest crystal field manifold in Dy(III) complexes are all well reproduced already using the bare 1e-SOC Hamiltonian $\mathcal{H}_{\mathrm{SO}}^{(1)}$.

Chapter 4

Conclusions

In this project I studied the relativistic contributions to the molecular Hamiltonian needed for accurate descriptions of the electronic structure and magnetic properties in lanthanide complexes.

In Chapter 2, I briefly presented the ab initio methods most used in the literature for the simulation of the electronic levels of the Ln(III) complexes (i.e. CASSCF/RASSI-SO and CAHF/CASCI-SO), and the equations which define the scalar relativistic corrections to the molecular Hamiltonian within the Douglas-Kroll-Hess formalism. I showed the details of the developments I have been working on for the implementation of the scalar relativistic terms within the CERES package.

In Chapter 3, I thoroughly tested a novel method developed and implemented within the research group for the efficient evaluation of the two-electron spin-orbit terms without loss of accuracy, which makes use of the Cholesky representation of the two-electron spin-orbit integrals, and I investigated a number of approximations to the Breit-Pauli spin-orbit coupling operator for the calculation of the ground multiplet crystal field levels and effective g tensors for lanthanide-based compounds within the CAHF/CASCI-SO method. Via extensive comparison of the computed crystal field energies for a family of lanthanide complexes, I showed that the bare one-electron Hamiltonian well reproduces the gaps within the lowest energy crystal field manifold with errors below 4% with respect to the evaluations made by the use of the complete Breit-Pauli Hamiltonian for the main ions used in the literature in the design of the lanthanide-based SMMs (i.e.

Dy, Tb, Er). Furthermore, the bare one-electron spin-orbit operator well reproduces the g tensor for the lowest crystal field manifold in Dy(III) complexes, then allowing for both high accuracy and computational time saving.

Part II

Project 2

Chapter 5

Introduction

Toroidal quantum states in molecular nanomagnets [94–96] represent a new way of thinking about quantum computation [97], molecular spintronics [98] and magnetoelectric coupling for multiferroics [99, 100], which can be contrasted with a more typical approach to the design of molecular devices based on the total spin (hence magnetic moment) degree of freedom.

These molecular quantum states were predicted [94] and observed [95, 96] in 2008, in a Dysprosium triangle [101], which had tangential in-plane strong magnetic anisotropy axes at the magnetic centres and a weak antiferromagnetic Dy-Dy exchange coupling interaction, resulting in a ground state of the system that is toroidal, i.e. featuring a ground state Kramers doublet with zero magnetic moment and a vortex in-plane arrangement of the local magnetic moments. Toroidal moment is a term that appears in the multipole expansion of the vector potential associated to a collection of local magnetic moments. It is the antisymmetric part of the quadrupole moment [100, 102]. In the context of single molecule magnets, this property can manifest itself as the head to tail arrangement of local metal-centred spin moments arranged along a ring structure, giving rise to two degenerate (clockwise and counterclockwise) non-magnetic vortex spin states within the ground Kramers doublet.

This can be illustrated with the help of a spin triangle of site spin 1/2 triangle that is equilateral and has antiferromagnetic interaction between its sites. Such a triangle is clearly spin frustrated - while the first two

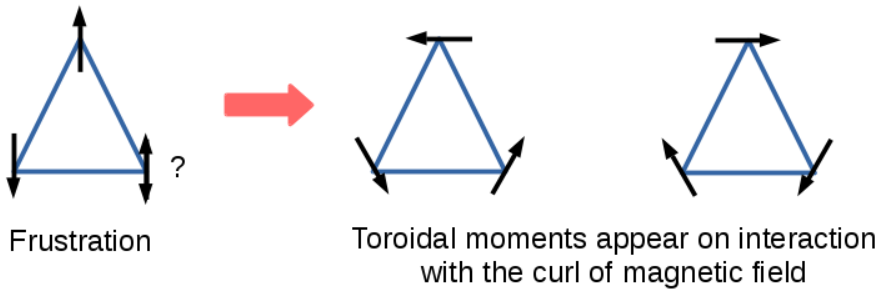

Figure 5.1: An illustration of a spin 1/2 ring with anti-ferromagnetic interactions between the sites. Upon interaction with the curl component of the external magnetic field, the degeneracy breaks leading to two states with a non-zero toroidal moment

spins can be placed anti-parallel to each other, the third spin doesn't have any clear orientation that would be energetically favourable. Both the available directions for orienting the spin leads to a ferromagnetic interaction between one pair of sites. This leads to two states which have total spin equal to 1/2 being degenerate with each other. Such a state is called a frustrated state. If the curl component of an external magnetic field $\vec{B}$, which can be expressed as $\vec{\nabla} \times \vec{B}$ interacts with such a frustrated state, the degeneracy breaks and two distinct toroidal states are obtained which are characterized by non zero values of the toroidal moment observable. Toroidal moment in such a system is given by (in atomic units):

$$\hat{\tau} = \sum_{p=1}^{3} (\hat{\mathbf{r}}_p \times \hat{\mathbf{S}}_p). \tag{5.1}$$

where $\mathbf{r}_p$ is the position vector and $\hat{\mathbf{S}}_p$) is the site spin operator of site p . This can be visualized as given in the figure:

Since the toroidal moment is a component of a generalized quadrupole moment, and intermolecular interactions between molecular magnetic quadrupoles decay faster with intermolecular distance, molecular devices based on the toroidal moment degree of freedom would allow closer packing hence higher device density. One issue given the protected nature of toroidal states, is then to find an efficient way to address

them in order to manipulate their state. Since the toroidal moment is the antisymmetric part of a magnetic quadrupole, it interacts with the curl of a magnetic field [100, 102], but direct and controlled application of such inhomogeneous magnetic fields at the molecular level is currently not feasible yet. Spintronics strategies to address such states have been discussed [95, 98, 103] , including in the next Chapter of this thesis [104], but the practical realization of such experimental set up, while within reach, has not yet been achieved.

Toroidal moments in molecular nanomagnets have recently attracted increasing attention, both in relation to theory [43, 49, 94, 95, 98, 103–105] and experiment [96, 101, 106–120]. Experimentally this has led to the synthesis of several rings other than Dy_3 in the highly in the highly anisotropic regime with four-, five-, and six-membered rings being synthesized [43, 109, 110, 112–118]. Although most of previous work has focused on rings with strong on site magnetic anisotropy and weak exchange [121], molecules with weak spin-orbit coupling have also been investigated, such as Cu3 and V15 [97, 100, 103, 119, 120, 122, 123], where a toroidal moment can arise due to spin frustration rather than strong on-site magnetic anisotropy.

Despite the many advances in ab-initio methods, it is currently not possible to perform meaningful multiconfigurational ab-initio computations for polynuclear metal complexes with more than two open-shell metal centres. Nonetheless, polynuclear metal complexes are of course a class of compounds which are interesting for a variety of reasons, among which the fact that such polynuclear complexes can potentially display a toroidal moment in the ground state, under appropriate conditions of exchange coupling, magnetic anisotropy and/or spin frustration. Hence, while current ab initio calculations can help unravel some single-centre property such as on-site magnetic anisotropy, at this time they struggle to be of much use to describe collective spin states of the metal ring. It is thus necessary to recur to spin Hamiltonian models, which have been a useful tool in this thesis for the study of toroidal moments in metal rings [94, 95, 103]. This Hamiltonian in the second quantized framework is given by:

$$\hat{H_{Spin}} = -\sum_{i,j} J_{i,j} \hat{S}_i \hat{S}_j, \tag{5.2}$$

where i and j are the indices of the site. J is a parameter that models the exchange interaction between sites i and j whose spins are given by $\hat{S}$. In practice, the interaction between sites that are further than

the nearest or next-nearest neighbour are considered zero. This is because the magnitude of exchange falls rapidly with distance. A positive magnitude of J is considered ferromagnetic in this convention.

Interestingly, the existence of toroidal moments in spin-frustrated triangles within the weak spin-orbit coupling regime has only been explored for a local on-site spin length of $S = 1/2$ [103], while rings with more than three centres have only been explored in the strong spin-orbit coupling regime [94,106,108,113,114,121]. In the second part of my Ph.D. thesis I will not only extend the discussion of the relationship between spin-frustration and toroidal moment to a family of generalised spin frustrated triangles having one heterometallic centre with arbitrary on-site spin, and identify the conditions for the existence of a toroidal moment in the resulting frustrated ground state (Chapter 6), but also extend for the first time the study of toroidal moments in the weak spin-orbit coupling regime to families of spin frustrated rings with more than 3 centers (Chapter 7). Conclusions will be drawn in Chapter 8

Chapter 6

Toroidal Moment in a Family of Spin-Frustrated Heterometallic Triangular Nanomagnets without Spin-Orbit Coupling: Applications in a Molecular Spintronics Device

Authors: Shashank V. Rao, Jared M. Ashtree, Alessandro Soncini

Affiliation: The School of Chemistry, University of Melbourne, Parkville, Victoria 3010, Australia

Submitted: 12th January 2020

Journal: Physica B

Manuscript No: PHYSB-D-20-00089

Abstract

We theoretically investigate a family of spin-frustrated triangular molecular nanomagnets with arbitrary on-site spin, featuring one heterometallic ion, in the limit of zero spin-orbit coupling. Analytical evaluation of the Heisenberg exchange states and spectrum shows that the ground state can either be the first example of a toroidal quartet, or feature two weakly split toroidal doublets, depending on the exchange parameters. The nonequilibrium spin dynamics of these toroidal states is modelled within a three-terminal molecular spintronics device, showing that gate and bias voltages can be used to tune the non-equilibrium population of these toroidal states, thus to monitor the ensuing toroidal magnetization of the device.

6.1 Introduction

The increasing demands of data storage and processing, as well as fundamental interest, have been driving research into the behavior of magnetic complexes [5, 124, 125]. The many diverse phenomena displayed by magnetic complexes, such as single-molecule magnetism [3, 4, 69], spin crossover [126] and toroidal moments [107, 121], are now seen as key areas of interest. In particular, the elusive property of toroidal moments has generated much interest recently, due to its applications in quantum computation [97], molecular spintronics devices [98], and magnetoelectric coupling for multiferroics [99, 100].

Toroidal states are vortex states that occur due to the head-to-tail arrangement of spins. The toroidal moment can be understood as the antisymmetric part of the magnetic quadrupole moment, which is odd under both time reversal and space reversal transformations [100, 102]. Molecular toroidal moments were first predicted [94] and observed [95, 96] in 2008, when quantum states with large nonzero toroidal moments were identified in a strongly anisotropic molecular ring, namely the Dy_3 triangle [101] with anisotropy axes tangential to the ring.

Toroidal moments interact with the curl component of a magnetic field, thus do not interact with homo-

geneous magnetic fields [100, 102]. This, combined with the fact that a quadrupole moment interacts over a shorter range than a dipole moment, means that toroidal states can lead to a much denser packing of quantum states than a qubit traditionally implemented with spin dipoles [94].

This concept has sparked a great interest in exploring toroidal moments, both in terms of theory [95,105] and experiment [96, 106, 108], with interest in Dy rings moving past the three-membered systems to four-, five- and six-membered systems [43, 111, 113–115], and also into heterometallic rings [109, 110, 112, 116–118]. Although most of the early interest in this area was in highly anisotropic rings with strong spin-orbit coupling and low site exchange [121], molecules with weak spin-orbit coupling have also been investigated, such as Cu_3 and V_{15} [97, 100, 103, 119, 120, 122, 123].

It is possible to split the populations of different toroidal states by applying a curling magnetic field [100, 102], but there is currently no known method for producing inhomogeneous magnetic fields on the molecular scale. We therefore consider using electric and spin currents to analyze these systems [98, 103, 127, 128], as there have been recent advances in the development of devices that can measure and manipulate spin states [129–135].

While most studies so far demonstrate the possible existence of two distinct ground toroidal states [95,100, 103], we demonstrate here that an "isosceles" spin triangle can produce *four* distinct, nonmagnetic toroidal states within a frustrated ground quartet. Additionally, particular isosceles systems can produce toroidal states in spin-frustrated doublets. In each case, we present analytical expressions for the toroidal moment quantum numbers. While several heterometallic spin triangles have been synthesized and characterized in literature [136–138], our results present specific ranges of spin exchange for which such systems would show these interesting properties, thus presenting a new avenue for future synthetic efforts.

We also analyze and optimize the performance of the isosceles spin triangle in a previously proposed spintronics device [98, 103], and explain how spin-transfer torque leads to a difference in the populations of the clockwise and counterclockwise toroidal states. Because our study explores the zero spin-orbit coupling regime, the spintronics device of interest has now been predicted to produce net toroidal magnetizations on triangles with strong [98], weak [103], or zero spin-orbit coupling.

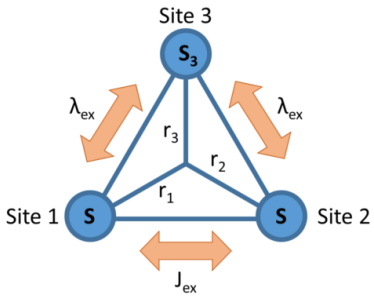

Figure 6.1: Schematic of the spin triangle of interest. Regardless of the overall geometry, the site spins as well as their couplings have a lateral plane of symmetry, so we describe the triangle as "isosceles". That is, the spins at sites one and two are equal, while the exchange interaction between sites one and three is equal to that between sites two and three.

6.2 Toroidal moment in a spin triangle with a $S_3 = \frac{1}{2}$ heteroatom

The isosceles spin triangle is depicted in Fig. 6.1. Sites one and two have spins $S_1 = S_2 \equiv S$, while site three has spin $S_3 = 1/2$. The exchange interaction between sites one and two is J_{ex}, and the other two exchange interactions are λ_{ex}. The Hamiltonian for such a system can be written using a Heisenberg spin model as:

$$\hat{H}_{ex} = -J_{ex}(\hat{\mathbf{S}}_1 \cdot \hat{\mathbf{S}}_2) - \lambda_{ex}(\hat{\mathbf{S}}_2 \cdot \hat{\mathbf{S}}_3 + \hat{\mathbf{S}}_3 \cdot \hat{\mathbf{S}}_1) = \frac{-J_{ex}}{2}(\hat{\mathbf{S}}_{12}^2 - \hat{\mathbf{S}}_1^2 - \hat{\mathbf{S}}_2^2) - \frac{\lambda_{ex}}{2}(\hat{\mathbf{S}}_T^2 - \hat{\mathbf{S}}_3^2 - \hat{\mathbf{S}}_{12}^2), \tag{6.1}$$

where $\hat{\mathbf{S}}_{12} = \hat{\mathbf{S}}_1 + \hat{\mathbf{S}}_2$ and $\hat{\mathbf{S}}_T = \hat{\mathbf{S}}_1 + \hat{\mathbf{S}}_2 + \hat{\mathbf{S}}_3$. The operators $\hat{\mathbf{S}}_1^2$, $\hat{\mathbf{S}}_2^2$ and $\hat{\mathbf{S}}_3^2$ always give constants which can be set as zero energy. As a result, the energies are:

$$E(S_{12}, S_T) = \frac{-\lambda_{ex}}{2} S_T(S_T + 1) - \frac{J_{ex} - \lambda_{ex}}{2} S_{12}(S_{12} + 1). \tag{6.2}$$

We are interested in particular in a spin-frustrated configuration, i.e. an antiferromagnetic ring with $J_{ex} < 0$ and $\lambda_{ex} < 0$, giving ground states with the lowest possible values of S_{12} and S_T. For the first few values of S_{12}, the energies are:

- $S_{12} = 0$, $S_T = \frac{1}{2} \Rightarrow E(0, \frac{1}{2}) = -\frac{3\lambda_{ex}}{8}$
- $S_{12} = 1$, $S_T = \frac{1}{2} \Rightarrow E(1, \frac{1}{2}) = -\frac{3\lambda_{ex}}{8} \pm |J_{ex} - \lambda_{ex}|$

- $S_{12}=1,\ S_T=\frac{3}{2} \Rightarrow E(1,\frac{3}{2})=-\frac{15\lambda_{ex}}{8}\pm|J_{ex}-\lambda_{ex}|$
- $S_{12}=2,\ S_T=\frac{3}{2} \Rightarrow E(2,\frac{3}{2})=-\frac{15\lambda_{ex}}{8}\pm 3|J_{ex}-\lambda_{ex}|$
- $S_{12}=2,\ S_T=\frac{5}{2} \Rightarrow E(2,\frac{5}{2})=-\frac{35\lambda_{ex}}{8}\pm 3|J_{ex}-\lambda_{ex}|$

and so on, where the '+' sign occurs for $|J_{ex}|>|\lambda_{ex}|$, and the '−' sign occurs for $|J_{ex}|<|\lambda_{ex}|$.

When $|J_{ex}|>|\lambda_{ex}|$, the $S_{12}=0,\ S_T=\frac{1}{2}$ doublet is the lowest in energy. We call this doublet $|A,M_T\rangle$, where $M_T=\pm\frac{1}{2}$ is the projection of S_T along the z-axis, perpendicular to the plane of the triangle. Whereas when $\frac{|\lambda_{ex}|}{8}<|J_{ex}|<|\lambda_{ex}|$, we get $S_{12}=1,\ S_T=\frac{1}{2}$ as the lowest energy doublet, which we call $|B,M_T\rangle$. For the case $|J_{ex}|=|\lambda_{ex}|$, the A and B doublets are equal in energy, so the ground manifold is a frustrated quartet.

Using standard angular-momentum coupling theory, expressions for $|A,M_T\rangle$ and $|B,M_T\rangle$ in terms of the individual site spins can be readily found:

$$\sqrt{2S+1}|A,\pm\frac{1}{2}\rangle=\sum_{m=-S}^{S}(-1)^{S-m}|S,m\rangle_1\otimes|S,-m\rangle_2\otimes|\frac{1}{2},\pm\frac{1}{2}\rangle_3, \tag{6.3}$$

$$\sqrt{S(S+1)(2S+1)}|B,\pm\frac{1}{2}\rangle=\pm\sum_{m=a}^{b}(-1)^{S-m}\sqrt{S(S+1)-m(m\mp1)}|S,m\rangle_1\otimes|S,-m\pm1\rangle_2\otimes|\frac{1}{2},\mp\frac{1}{2}\rangle_3$$
$$-\sum_{m=-S}^{S}(-1)^{S-m}m|S,m\rangle_1\otimes|S,-m\rangle_2\otimes|\frac{1}{2},\pm\frac{1}{2}\rangle_3, \tag{6.4}$$

$$(a,b)=\begin{cases}(-S+1,S),\ \text{for}\ |B,+\frac{1}{2}\rangle\\ (-S,S-1),\ \text{for}\ |B,-\frac{1}{2}\rangle.\end{cases}$$

Next, following up from our recent investigation of toroidal moments in a frustrated spin triangle with $S_1=S_2=S_3=1/2$ [103], we want to probe the existence of a toroidal ground state having zero magnetic moment in this generalised spin triangle. The toroidal moment operator reads:

$$\hat{\tau}=g\mu_B\sum_{p=1}^{3}(\hat{\mathbf{r}}_p\times\hat{\mathbf{S}}_p), \tag{6.5}$$

where $\mathbf{r}_p$ is the position vector of site p. Although toroidal states exist for general triangular geometries, we present the equilateral case as an illustrative example. For $|\mathbf{r}_p|=R$, $\alpha_p=\frac{2\pi(p-1)}{3}$ and $\hat{S}_{p\pm}=\hat{S}_{px}\pm\hat{S}_{py}$,

the z-component of the toroidal moment operator becomes:

$$\hat{\tau}_z = -\frac{ig\mu_B R}{2}\sum_{p=1}^{3}(e^{-i\alpha_p}\hat{S}_{p+} - e^{i\alpha_p}\hat{S}_{p-}). \tag{6.6}$$

For the case $|J_{ex}| = |\lambda_{ex}|$, the matrix representation of the toroidal moment operator $\mathbb{T}_z$ over the four-fold ground manifold defined by the A and B doublets Eq. (6.3) can be readily evaluated as:

$$\frac{2\mathbb{T}_z}{g\mu_B R} = \begin{bmatrix} 0 & e^{\left(+i\frac{\pi}{6}\right)} & 0 & -\frac{2}{\sqrt{3}}e^{\left(-i\frac{\pi}{3}\right)}\sqrt{S(S+1)} \\ e^{\left(-i\frac{\pi}{6}\right)} & 0 & -\frac{2}{\sqrt{3}}e^{\left(+i\frac{\pi}{3}\right)}\sqrt{S(S+1)} & 0 \\ 0 & -\frac{2}{\sqrt{3}}e^{\left(-i\frac{\pi}{3}\right)}\sqrt{S(S+1)} & 0 & -e^{\left(+i\frac{\pi}{6}\right)} \\ -\frac{2}{\sqrt{3}}e^{\left(+i\frac{\pi}{3}\right)}\sqrt{S(S+1)} & 0 & -e^{\left(-i\frac{\pi}{6}\right)} & 0 \end{bmatrix}, \tag{6.7}$$

with eigenvectors (grouped in two toroidal doublets $\omega = 1, 2$, see Fig. 6.2 for a graphical representation):

$$2|\tau_{\omega\pm}\rangle = \pm\, e^{\frac{i2\pi}{3}}|A, +\frac{1}{2}\rangle - (-1)^{\omega} i|A, -\frac{1}{2}\rangle \pm (-1)^{\omega} e^{\frac{i\pi}{6}}|B, +\frac{1}{2}\rangle + |B, -\frac{1}{2}\rangle,$$

while the associated eigenvalues are the elusive toroidal moments we find for the two degenerate ground doublets:

$$\tau_{\omega\pm} = \pm\left(\sqrt{\frac{S(S+1)}{3}} - \frac{(-1)^{\omega}}{2}\right) g\mu_B R. \tag{6.8}$$

Note that for $S = 1/2$, we recover the case of a triangle with equal on-site spins $S = 1/2$ [103], where only two states of the degenerate quartet carry a non-zero toroidal moment $\tau = \pm g\mu_B R$, see Eq. (6.8).

However, for $S > 1/2$ and $J_{ex} = \lambda_{ex}$, from Eq. (6.8) we can see that the ground quartet now consists of four distinct toroidal states carrying a non-zero toroidal moment: $|\tau_{1+}\rangle$, $|\tau_{1-}\rangle$, $|\tau_{2+}\rangle$ and $|\tau_{2-}\rangle$. We also consider the cases $|\lambda_{ex}| < |J_{ex}|$ and $\frac{|\lambda_{ex}|}{8} < |J_{ex}| < |\lambda_{ex}|$ by finding the eigenstates of the toroidal moment operator within the subspaces $\{|A, +\frac{1}{2}\rangle,\ |A, -\frac{1}{2}\rangle\}$ and $\{|B, +\frac{1}{2}\rangle,\ |B, -\frac{1}{2}\rangle\}$ [first and second 2×2 blocks of $\mathbb{T}_z$, respectively, see Eq. (6.7)]. We label these toroidal states as $|\tau_{A\pm}\rangle$ and $|\tau_{B\pm}\rangle$, and depict their local spin

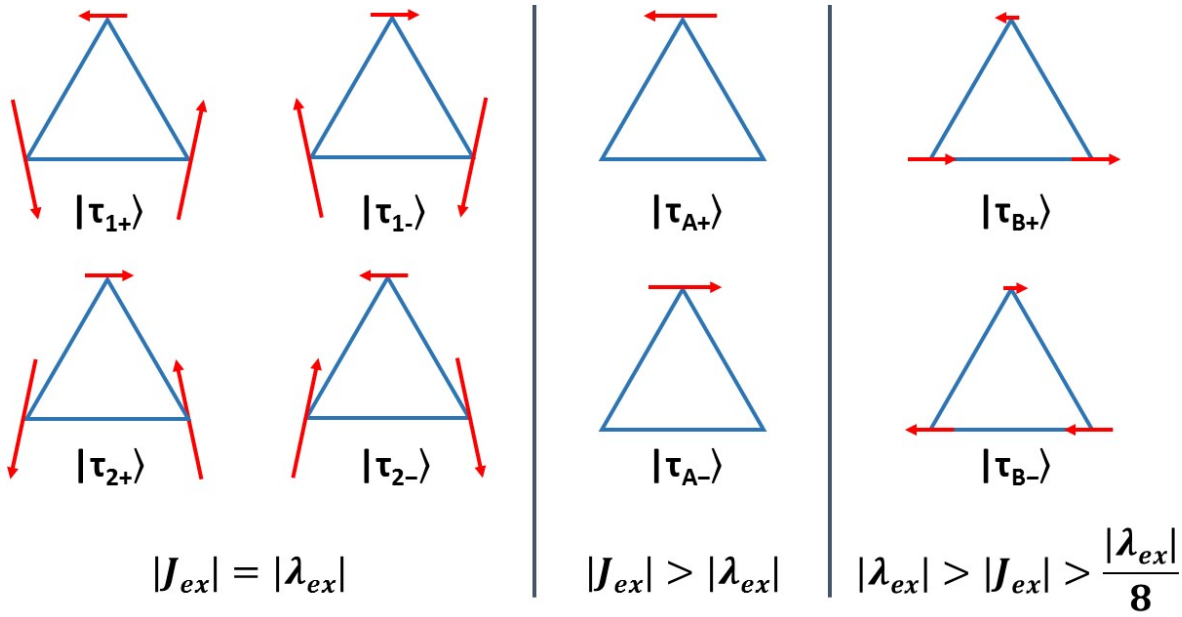

Figure 6.2: Local spin expectation values $\langle \mathbf{S}_p \rangle$ in the toroidal states, shown for $S = 2$, $S_3 = \frac{1}{2}$. In $|\tau_{1\pm}\rangle$ and $|\tau_{2\pm}\rangle$, the spin expectation values at sites one and two have magnitudes $|\langle \mathbf{S}_1 \rangle| = |\langle \mathbf{S}_2 \rangle| = \frac{2S+1}{6}$, and angles with the horizontal of $\cos^{-1}(\frac{1}{2S+1})$, while $|\langle \mathbf{S}_3 \rangle| = \frac{1}{3}$ along the horizontal. In $|\tau_{A\pm}\rangle$, $|\langle \mathbf{S}_1 \rangle| = |\langle \mathbf{S}_2 \rangle| = 0$ and $|\langle \mathbf{S}_3 \rangle| = \frac{1}{2}$, while for $|\tau_{B\pm}\rangle$, $|\langle \mathbf{S}_1 \rangle| = |\langle \mathbf{S}_2 \rangle| = \frac{1}{3}$ and $|\langle \mathbf{S}_3 \rangle| = \frac{1}{6}$. The red arrows indicate the direction and magnitude of $\langle \mathbf{S}_p \rangle$.

expectation values in Fig. 6.2:

$$\sqrt{2}|\tau_{A\pm}\rangle = \mp e^{i\frac{7\pi}{6}}|A, +\frac{1}{2}\rangle + |A, -\frac{1}{2}\rangle, \quad \tau_{A\pm} = \pm\frac{1}{2}g\mu_B R, \tag{6.9}$$

$$\sqrt{2}|\tau_{B\pm}\rangle = \pm e^{i\frac{7\pi}{6}}|B, +\frac{1}{2}\rangle + |B, -\frac{1}{2}\rangle, \quad \tau_{B\pm} = \pm\frac{1}{2}g\mu_B R. \tag{6.10}$$

6.3 Toroidal moment for arbitrary values of the heterometallic spin S_3

We now generalize our model for a generic spin S_3. Using the energies in Eq. (6.2), we look for values of S_3 which lead to frustrated ground states, which may then give rise to toroidal states. For integer n in the antiferromagnetic isosceles spin triangle with $S_1 = S_2 \equiv S$:

- If $S_3 = n$, the ground state will have $S_{12} = n' \leq n$ and integer $S_T = n - n'$, so will not be frustrated.
- If $S_3 = n + \frac{1}{2}$, $2S \geq n$ and $|\lambda_{ex}| < |J_{ex}|$, the ground state will have $S_{12} = n$ and $S_T = S_3 - S_{12} = \frac{1}{2}$, so will be a doublet (termed A').
- If $S_3 = n + \frac{1}{2}$, $2S \geq n + 1$ and $\frac{|\lambda_{ex}|}{8} < |J_{ex}| < |\lambda_{ex}|$, the ground state will have $S_{12} = n + 1$ and $S_T = S_{12} - S_3 = \frac{1}{2}$, so will be a doublet (termed B').

We therefore focus on the case $S_3 = n + \frac{1}{2}$ with frustrated ground states $|A', M_T\rangle$ and $|B', M_T\rangle$. Such systems have been synthesized, for example: $Gd^{III}{}_2Mn^{IV}$ [136], $Fe^{III}{}_2Gd^{III}$ [137, 138] and $Mn^{III}{}_2Gd^{III}$ [137] for various values of λ_{ex} and J_{ex}. We present $|A', +\frac{1}{2}\rangle$ and $|B', +\frac{1}{2}\rangle$ here, written in a direct product basis with m, $l - m$ and $\frac{1}{2} - l$ as the z-components of the spins at sites one, two and three, respectively:

$$\begin{aligned} |\Gamma, +\frac{1}{2}\rangle = &\sum_{l=0}^{a_1} \left(\sum_{m=-S+l}^{S} |S, m\rangle_1 \otimes |S, l-m\rangle_2 C_{12}^{+}(a_1, l, m, S) \right) \otimes |n + \frac{1}{2}, +\frac{1}{2} - l\rangle_3 C_{3\Gamma}(n, l) \\ &+ \sum_{l=-a_1}^{-1} \left(\sum_{m=-S}^{S+l} |S, m\rangle_1 \otimes |S, l-m\rangle_2 C_{12}^{-}(a_1, l, m, S) \right) \otimes |n + \frac{1}{2}, +\frac{1}{2} - l\rangle_3 C_{3\Gamma}(n, l), \end{aligned} \tag{6.11}$$

$$C_{12}^{\pm}(n, l, m, S) = \sqrt{\frac{(2n+1)(2S-n)!(a_5+l)!(a_6-l)!(n-l)!(n+l)!}{(2S+n+1)!(a_5)!(a_6)!}} \sum_{q=a_3}^{a_4} (-1)^{a_5 - n + q} \binom{a_6}{q} \binom{a_5}{n-q} \binom{n}{q-l}, \tag{6.12}$$

$$(a_5, a_6) = (S - m, S + m), \qquad \sqrt{(n+1)(2a_1+1)} C_{3\Gamma}(n, l) = (-1)^{a_1 - l} \sqrt{n - a_2 + 1}, \tag{6.13}$$

$$(a_1, a_2) = \begin{cases} (n, l), & \text{if } \Gamma = A' \\ (n+1, -l), & \text{if } \Gamma = B' \end{cases}, \qquad (a_3, a_4) = \begin{cases} (l, n), & \text{for } C_{12}^{+}(n, l, m, S) \\ (0, n+l), & \text{for } C_{12}^{-}(n, l, m, S) \end{cases}. \tag{6.14}$$

Using the symmetry and normalization properties of the Clebsch-Gordan coefficients between sites one and two:

$$\sum_{m=-S+\frac{l}{2}}^{S-\frac{l}{2}} \langle S, m+\frac{l}{2}, S, -m+\frac{l}{2} | n, l \rangle^2 = 1, \tag{6.15}$$

$$\langle S, m_1, S, m_2 | n, l \rangle^2 = \langle S, m_2, S, m_1 | n, l \rangle^2 = \langle S, -m_1, S, -m_2 | n, -l \rangle^2, \tag{6.16}$$

together with the following identity:

$$\sum_{m=-S+n}^{S} \left(m - \frac{n}{2}\right)^2 \frac{(S-m+n)!(S+m)!}{(S+m-n)!(S-m)!} = \frac{(2S+n+2)!}{4(2n+1)(2n+3)\binom{2n}{n}(2S-n-1)!}, \tag{6.17}$$

we evaluate the relevant reduced matrix elements $\langle \Gamma || \hat{T}^1(\hat{\mathbf{S}}_p) || \Gamma \rangle$ on the basis $|\Gamma, M_\Gamma\rangle = \{|A', +\frac{1}{2}\rangle, |A', -\frac{1}{2}\rangle, |B', +\frac{1}{2}\rangle, |B', -\frac{1}{2}\rangle\}$ for $S_3 = n + \frac{1}{2}$ as:

- $\langle A' || \hat{T}^1(\hat{\mathbf{S}}_1) || A' \rangle = -n/\sqrt{6}$
- $\langle A' || \hat{T}^1(\hat{\mathbf{S}}_2) || A' \rangle = -n/\sqrt{6}$
- $\langle A' || \hat{T}^1(\hat{\mathbf{S}}_3) || A' \rangle = (3+2n)/\sqrt{6}$
- $\langle A' || \hat{T}^1(\hat{\mathbf{S}}_1) || B' \rangle = -2\sqrt{(S-\frac{n}{2})(S+1+\frac{n}{2})/6}$
- $\langle A' || \hat{T}^1(\hat{\mathbf{S}}_2) || B' \rangle = +2\sqrt{(S-\frac{n}{2})(S+1+\frac{n}{2})/6}$
- $\langle A' || \hat{T}^1(\hat{\mathbf{S}}_3) || B' \rangle = 0$
- $\langle B' || \hat{T}^1(\hat{\mathbf{S}}_1) || B' \rangle = (2+n)/\sqrt{6}$
- $\langle B' || \hat{T}^1(\hat{\mathbf{S}}_2) || B' \rangle = (2+n)/\sqrt{6}$
- $\langle B' || \hat{T}^1(\hat{\mathbf{S}}_3) || B' \rangle = (-1-2n)/\sqrt{6}$

Using these results, we can represent the toroidal moment operator in various ground manifolds. For example, for an equilateral triangle with $S_3 = n + \frac{1}{2}$, setting $\lambda_{ex} = J_{ex}$ and representing $\hat{\tau}_z$ on the basis $\{|A', +\frac{1}{2}\rangle, |A', -\frac{1}{2}\rangle, |B', +\frac{1}{2}\rangle, |B', -\frac{1}{2}\rangle\}$ gives the following eigenvalues:

$$\begin{aligned}\tau_{1'\pm} &= \left(+\frac{n+1}{2} \pm \sqrt{(S-\frac{n}{2})(S+1+\frac{n}{2})/3}\right) g\mu_B R, \\ \tau_{2'\pm} &= \left(-\frac{n+1}{2} \pm \sqrt{(S-\frac{n}{2})(S+1+\frac{n}{2})/3}\right) g\mu_B R.\end{aligned} \tag{6.18}$$

Alternatively, representing $\hat{\tau}_z$ on $\{|A', +\frac{1}{2}\rangle, |A', -\frac{1}{2}\rangle\}$ (ground for $|\lambda_{ex}| < |J_{ex}|$), or representing $\hat{\tau}_z$ on $\{|B', +\frac{1}{2}\rangle, |B', -\frac{1}{2}\rangle\}$ (ground for $\frac{|\lambda_{ex}|}{8} < |J_{ex}| < |\lambda_{ex}|$), gives the following eigenvalues:

$$\tau_{A'\pm} = \tau_{B'\pm} = \pm\left(\frac{n+1}{2}\right) g\mu_B R. \tag{6.19}$$

Thus, the strengths of the exchange couplings determine whether there are two or four distinct toroidal states in the frustrated ground manifolds, regardless of the precise values for $S_3 = n{+}1/2$ and $S >= (n{+}1)/2$.

While we see in the next section that the most promising use of this device is for the purpose of data processing rather than storage. It is still interesting to consider an analogy to spin dipole moment where a degenerate multiplet of $2S + 1$ values can be split by a site anisotropy operator in the Hamiltonian ($D\hat{S}_z^2$) which commutes with the Zeeman operator ($\sum_{p=1}^{3} \hat{S}_p \cdot \vec{B}$). This leads to an energy barrier to relaxation of a spin polarized state. A state which is created by the application of an external magnetic field. In the analogous case for toroidal moments when $\lambda_{ex} = J_{ex}$ in the heterometallic spin triangle it would be interesting to see if an operator exists which would commute with the toroidal moment operator ($\sum_{p=1}^{3}(\hat{\mathbf{r}}_p \times \hat{\mathbf{S}}_p)$). Such an operator, could produce an similar barrier to relaxation of a state polarized for a particular value of toroidal moment. Such a state being produced here with the use of a curling magnetic field ($\nabla \times \vec{B}$), or a spintronics device as detailed below.

Additionally we numerically explored the case of a Dzyaloshinskii-Moriya term being included in the spin hamiltonian, where we used the operator given by $\hat{H}_{DM} = D\sum_i(\hat{S}_i \times \hat{S}_{i+1})_Z$ as used in literature for similar systems [103]. This was explored for the case of $D = J_{ex} = \lambda_{ex}$ to illustrate the effect when the Dzyaloshinskii-Moriya effect is comparable in strength to the spin exchange for the quartet. For the case

of $S_3 = 0.5$ and $S = 1,\ 1.5,\ 2,\ 2.5$ and 3, the ground doublets had toroidal moments $T_z = (\pm 1.467,\ \pm 1.939,\ \pm 2.417,\ \pm 2.901$ and $\pm 3.388)$. When S_3 was changed to 1.5 the ground toroidal moments changed to $T_z = (\pm 1.705,\ \pm 2.195,\ \pm 2.684,\ \pm 3.173$ and $\pm 3.663)$. What we observed is that the $J_{ex} = \lambda_{ex}$ quartet splits into two doublets which are mixed states of the A and B doublets. Toroidal moments are still observed, with magnitudes larger than the pure doublets. Dzyaloshinskii-Moriya effect seems likely to assist in the formation of the toroidal doublets. However, the exact effect in the context of a complex would have to take into account the exact orientation and magnitude of D, which in the more general case is described as a vector.

6.4 Use in a Spintronics Device

With these toroidal states in mind, we now explore how this family of triangular molecules would behave in the tunneling spintronics device proposed in earlier works [98, 103]. The device consists of a spin-polarized source lead and an unpolarized drain lead, whose Fermi levels are offset by an external bias potential, see Fig. 6.3. An external gate potential is also applied, to induce a resonance between the ground states of the triangle in its redox-neutral and singly-reduced forms. These two biases promote electrons to pass from the source lead, onto the triangle and then onto the drain lead. That is, we apply a sequential tunneling model under the Coulomb Blockade regime (doubly-reduced states are considered energetically inaccessible) [98,103,139–145]. This is because typically the leads are weakly coupled to the system being probed, which leads to a charge transfer integralbeing smaller than the charging energy. Experimental observation of characteristic plots when the differential conductance is plotted with respect to the gate and bias voltage in similar devices provides further evidence for this regime. These plots are known as coulomb diamonds. Recently some devices have shown charge transfer in the coherent regime [146], but the theoretical modelling of these devices is quite complex. We present the treatment of the coulomb blockade regime as a first step which explores the more common situation for these devices. However, a future treatment for the coherent regime would also be an interesting future avenue of study for these systems.The Hamiltonian describing these

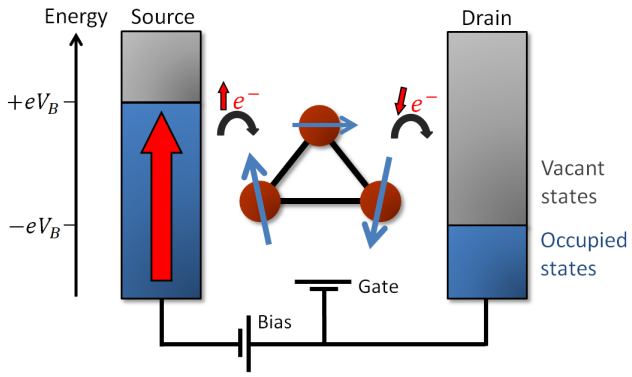

Figure 6.3: Schematic of the tunneling spintronics device based on a triangular nanomagnet with isosceles spin-coupling. The source and drain leads are weakly hybridized with the triangle, allowing electrons to sequentially tunnel from the up-polarized source lead, to the triangle, then to the unpolarized drain lead. As an electron passes from one side of the triangle to the other, its spin may interact with the triangle's toroidal spin texture. The extent of spin switching is indicative of the strength of a spin-transfer torque which also induces a net toroidal magnetization on the triangle. The triangle is depicted with the spin texture of the redox-neutral $|\tau_{1-}\rangle$ state.

tunneling processes in the coulomb blockade regime is [141, 143]:

$$\hat{H}_T = \sum_{p=1}^{3} \sum_{k}^{\text{first BZ}} \sum_{L}^{S,D} \sum_{\gamma}^{\uparrow,\downarrow} \beta_{pL} (\hat{a}^\dagger_{p\gamma} \hat{c}_{kL\gamma} + \hat{c}^\dagger_{kL\gamma} \hat{a}_{p\gamma}), \tag{6.20}$$

where $\hat{a}^\dagger_{p\gamma}$ creates an electron on site p with spin $\gamma = \uparrow$ or $\downarrow$; $\hat{c}^\dagger_{kL\gamma}$ creates an electron with wavenumber k and spin γ on lead $L = S$ or D (source or drain); k varies within the first Brillouin zone of a lead's electronic band structure; and β_{pL} is the tunneling amplitude between site p and lead L.

We set up the master equation for the nonequilibrium populations of the triangle's redox-neutral and singly-reduced states in the usual manner, by applying the Born-Markov approximation and considering coherences between different states of the triangle as negligible [140]:

$$\frac{dP_j}{dt} = \sum_{i \neq j} P_i W_{i \to j} - P_j \sum_{i \neq j} W_{j \to i}, \tag{6.21}$$

where $W_{i \to j}$ is the transition rate from state $|i\rangle$ to state $|j\rangle$. To find the transition rates, we apply the Fermi golden rule and integrate over all wavenumbers in each lead's first Brillouin zone, treating the tunneling

amplitudes β_{pL} and densities of spin states $\rho_{L\gamma}$ as being essentially constant [142, 144]:

$$W^{L\gamma}_{\tau_i \to r_j} = \frac{2\pi\rho_{L\gamma}}{\hbar} \left| \langle r_j | \sum_{p=1}^{3} \beta_{pL} \hat{a}^{\dagger}_{p\gamma} | \tau_i \rangle \right|^2 F_L\left(\Delta E\right), \tag{6.22}$$

where $W^{L\gamma}_{\tau_i \to r_j}$ is the charging rate from neutral state $|\tau_i\rangle$ to reduced state $|r_j\rangle$, with the extra electron coming from lead L and having spin γ; $\Delta E = E(r_j) - E(\tau_i)$ is the energy difference between the two states; and $F_L(\Delta E) = [1 + \exp(\frac{\Delta E - \mu_L}{k_B T})]^{-1}$, with $\mu_S = +eV_B$ and $\mu_D = -eV_B$ being the Fermi levels of the source and drain leads. A discharging rate such as $W^{L\gamma}_{r_j \to \tau_i}$ is defined similarly, but is weighted by $[1 - F_L(\Delta E)]$ rather than $F_L(\Delta E)$.

Before proceeding further, we must establish how the triangle would interact with an extra electron which is passing through. We consider exchange coupling between the extra electron's spin and the local spin where the electron temporarily resides, and delocalization of the extra electron across all three sites [145, 147]:

$$\hat{H}_{Hund} = -\sum_{p=1}^{3} \sum_{\gamma,\delta}^{\uparrow,\downarrow} J_{Hp} \left(\hat{a}^{\dagger}_{p\gamma} \hat{a}_{p\delta} \sigma_{\gamma\delta} \cdot \hat{\mathbf{S}}_p \right), \tag{6.23}$$

$$\hat{H}_{hop} = \sum_{p=1}^{3} \sum_{\gamma}^{\uparrow,\downarrow} t_{p,p+1} \left(\hat{a}^{\dagger}_{p\gamma} \hat{a}_{p+1,\gamma} + \hat{a}^{\dagger}_{p+1,\gamma} \hat{a}_{p\gamma} \right). \tag{6.24}$$

The subscripts γ and δ indicate the rows and columns of the entries in the Pauli matrices σ_x, σ_y and σ_z to be used in the dot product with $\hat{\mathbf{S}}_p$. The isosceles nature of the triangle is used to reduce the number of parameters in the above Hamiltonians, such that $J_{H1} = J_{H2} \equiv J_{H12}$ and $t_{13} = t_{23} \equiv t_3$.

We apply first-order degenerate perturbation theory to solve $\hat{H}_{Hund}$ and $\hat{H}_{hop}$ simultaneously within the ground manifolds of $\hat{H}_{ex}$ (See Eq. 6.1). That is, we choose $|J_{ex}|$, $|\lambda_{ex}| \gg J_{H12}$, J_{H3}, t_{12}, t_3, β_{pL}, eV_B, $k_B T$ and inspect each ground manifold separately: $|J_{ex}| > |\lambda_{ex}|$, $|J_{ex}| = |\lambda_{ex}|$, $\frac{|\lambda_{ex}|}{8} < |J_{ex}| < |\lambda_{ex}|$. We then solve Eq. (6.21) under the steady-state approximation to obtain the nonequilibrium populations of states. For the case of $|J_{ex}| = |\lambda_{ex}|$, see Fig. 6.4.

Based on a numerical analysis of the transition rates in Eq. (6.22), we have concluded that the mechanism behind the population splitting for a forward bias voltage is as follows: The rate at which an electron moves from the source lead to the triangle is faster when the initial exchange coupling between the electron and the triangle is favorable. For example, consider the scenario where $|J_{ex}| = |\lambda_{ex}|$ and the Hund exchange coupling

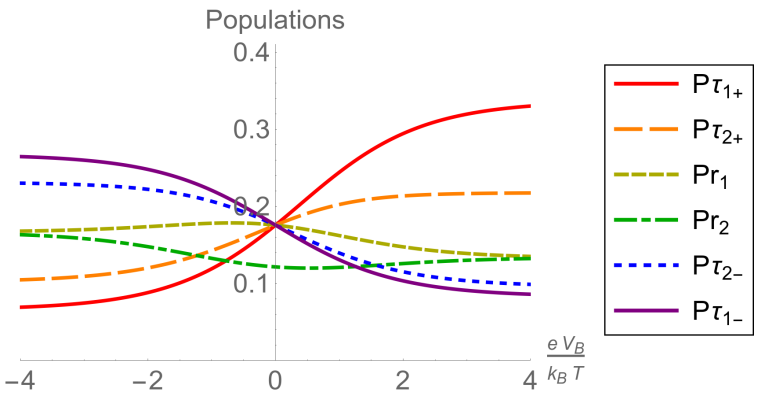

Figure 6.4: Nonequilibrium populations vs. bias voltage for the device shown in Fig. 6.3, using $S = \frac{7}{2}$, $S_3 = \frac{1}{2}$ and $|J_{ex}| = |\lambda_{ex}| \gg J_{H12}\ S > J_{H3}\ S_3$, t_{12}, t_3, β_{pL}, eV_B, k_BT. Pr_1 and Pr_2 represent the populations of the lowest energy singly-reduced states $|r_1\rangle$ and $|r_2\rangle$, which are split in energy by t_{12}. The populations of other reduced states are negligible and not shown. A net toroidal magnetization can be prepared as counterclockwise or clockwise by using a positive or negative bias, respectively.

to an extra electron is ferromagnetic. In states $|\tau_{1-}\rangle$ and $|\tau_{2-}\rangle$, the local spin which is nearest to the source lead is almost parallel to the source's polarization direction, see Fig. 6.3. With this alignment, there will be an efficient transfer in population from $|\tau_{1-}\rangle$ and $|\tau_{2-}\rangle$ (redox-neutral) to $|r_1\rangle$ and $|r_2\rangle$ (singly-reduced) as the electron moves onto the triangle. Meanwhile, the drain lead is unpolarized, so the rate at which an electron moves from the triangle to the drain is less dependent on the triangle's spin state, so any of $|\tau_{1\pm}\rangle$ or $|\tau_{2\pm}\rangle$ may be regenerated. The overall effect is a transfer of population from $|\tau_{1-}\rangle$ and $|\tau_{2-}\rangle$ to $|\tau_{1+}\rangle$ and $|\tau_{2+}\rangle$, thus a net toroidal magnetization is produced, see Fig. 6.4.

Conversely, for a reverse bias voltage, the triangle may be in any redox-neutral state $|\tau_{1\pm}\rangle$ or $|\tau_{2\pm}\rangle$ when an electron tunnels from the unpolarized drain lead onto the triangle to produce a singly-reduced state $|r_1\rangle$ or $|r_2\rangle$. However, the electron must be spin-up when it tunnels onto the polarized source lead. Thus, in the case of ferromagnetic Hund coupling, the triangle is more likely to be reset into a clockwise state ($|\tau_{1-}\rangle$ or $|\tau_{2-}\rangle$) than a counterclockwise state ($|\tau_{1+}\rangle$ or $|\tau_{2+}\rangle$) when the electron departs. (For antiferromagnetic Hund coupling or a down-polarized source lead, the preference for clockwise or counterclockwise is simply reversed.)

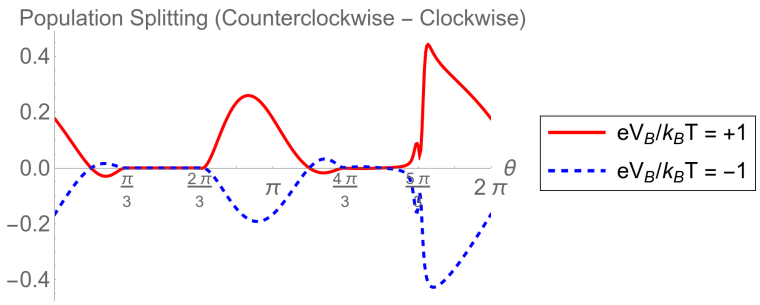

Figure 6.5: Nonequilibrium population splitting $(\mathrm{P}\tau_{1+}+\mathrm{P}\tau_{2+})-(\mathrm{P}\tau_{1-}+\mathrm{P}\tau_{2-})$ vs. in-plane angle of rotation θ relative to the geometry shown in Fig. 6.3, using $S=\frac{7}{2}$, $S_3=\frac{1}{2}$ and $|J_{ex}|=|\lambda_{ex}|\gg J_{H12}\ S>J_{H3}\ S_3$, t_{12}, t_3, β_{pL}, eV_B, k_BT. The angular dependencies of the tunneling amplitudes β_{pL} are empirically chosen as follows: $\beta_{1S}\propto \mathrm{Max}\left[\cos\left(\theta+\pi/6\right),0\right]$, $\beta_{2S}\propto \mathrm{Max}\left[\cos\left(\theta+5\pi/6\right),0\right]$, $\beta_{3S}\propto \mathrm{Max}\left[\cos\left(\theta-\pi/2\right),0\right]$, $\beta_{1D}\propto \mathrm{Max}\left[\cos\left(\theta-5\pi/6\right),0\right]$, $\beta_{2D}\propto \mathrm{Max}\left[\cos\left(\theta-\pi/6\right),0\right]$, $\beta_{3D}\propto \mathrm{Max}\left[\cos\left(\theta+\pi/2\right),0\right]$.

Since the selectivity in transition rates for clockwise or counterclockwise states depends on the orientations of the local spins, when the triangle is rotated within its plane, the strength of the population splitting varies dramatically, see Fig. 6.5. For example, if the local spin which is nearest to the source is oriented roughly perpendicular to the source's spin-polarization direction, the initial Hund coupling will be relatively unaffected by the choice of a clockwise state over a counterclockwise state, so the corresponding charging rates will become equal, and there will be no population splitting. Alternatively, if that local spin is aligned along the polarization direction, there will be a significant difference in the charging rates, and the mechanism described above takes place.

To further understand this mechanism, we studied the dependence of the population splitting on the strengths of the Hund couplings, and found the splitting to be larger when $|J_{\mathrm{H}12}S|>|J_{\mathrm{H}3}S_3|$, see Fig. 6.6. In this case, the ground singly-reduced states are $|r_1\rangle$ and $|r_2\rangle$, in which the extra electron predominantly resides on either of the two sites with spin S, whereas when $|J_{\mathrm{H}12}S|<|J_{\mathrm{H}3}S_3|$, the extra electron predominantly resides only on the site with spin S_3. To produce the spin-transfer torque needed to induce a net toroidal magnetization on the triangle, the extra electron's spin must be rotated as it moves across the triangle, which is best achieved via Hund coupling to *two* differently oriented spins, so the case of $|J_{\mathrm{H}12}S|>|J_{\mathrm{H}3}S_3|$

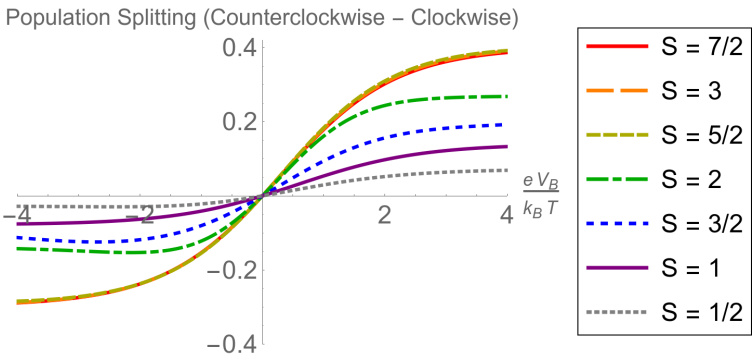

Figure 6.6: Nonequilibrium population splitting $(\mathrm{P}\tau_{1+} + \mathrm{P}\tau_{2+}) - (\mathrm{P}\tau_{1-} + \mathrm{P}\tau_{2-})$ vs. bias voltage for various values of S, using the geometry shown in Fig. 6.3 (i.e. $\theta = 0$), $S_3 = \frac{1}{2}$ and $|J_{ex}| = |\lambda_{ex}| \gg |J_{H3}| = 4|J_{H12}| > t_{12}$, t_3, β_{pL}, eV_B, k_BT. The ideal regime for producing a strong toroidal magnetization is $|J_{H12}\ S| > |J_{H3}\ S_3|$, which can be achieved by increasing S, as done here, and/or by increasing $|J_{H12}|$. For $|J_{H12}\ S| - |J_{H3}\ S_3| > k_BT$, further increases in $|J_{H12}\ S|$ have little effect.

is more effective.

Of course, if this spintronics device is to be used for high-density data storage applications, we require a method to measure the net toroidal magnetization as being clockwise or counterclockwise. This would be virtually impossible to do via direct magnetic probing of the triangular nanomagnet, as non-dipolar toroidal states do not interact with homogeneous magnetic fields [100, 102]. Rather, we propose to look for evidence of the toroidal magnetization by measuring the spin currents passing through the device.

With the populations of states known, we simply multiply by the relevant transition rates to evaluate the spin currents passing through each lead [140–144]:

$$I_S^{\uparrow} - I_S^{\downarrow} = e \sum_{i,j} \left[\left(W^{S\uparrow}_{\tau_i \to r_j} - W^{S\downarrow}_{\tau_i \to r_j} \right) P\tau_i - \left(W^{S\uparrow}_{r_j \to \tau_i} - W^{S\downarrow}_{r_j \to \tau_i} \right) Pr_j \right], \tag{6.25}$$

$$I_D^{\uparrow} - I_D^{\downarrow} = -e \sum_{i,j} \left[\left(W^{D\uparrow}_{\tau_i \to r_j} - W^{D\downarrow}_{\tau_i \to r_j} \right) P\tau_i - \left(W^{D\uparrow}_{r_j \to \tau_i} - W^{D\downarrow}_{r_j \to \tau_i} \right) Pr_j \right]. \tag{6.26}$$

We find that the polarization of the spin current passing through the device is partially reversed, to an extent which varies in accordance with the mechanism for population splitting described above, see Fig. 6.7. For example, with the geometry shown in Fig. 6.3 (i.e. $\theta = 0$), there is a strong selectivity in the charging

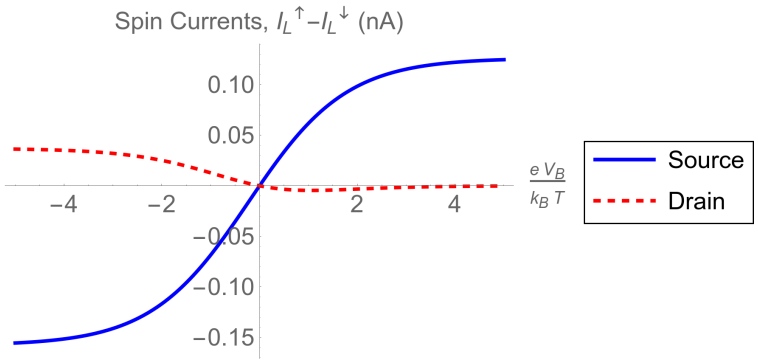

Figure 6.7: Spin currents vs. bias voltage, using the geometry shown in Fig. 6.3 (i.e. $\theta = 0$), $S = \frac{7}{2}$, $S_3 = \frac{1}{2}$ and $|J_{ex}| = |\lambda_{ex}| \gg J_{H12}\ S > J_{H3}\ S_3$, t_{12}, t_3, β_{pL}, eV_B, k_BT, with $\rho_{S\uparrow} = 1$ cm, $\rho_{S\downarrow} = 0$ cm, $\rho_{D\uparrow} = \rho_{D\downarrow} = 0.5$ cm, $\beta_{1D} = \beta_{2S} = 0.1$ cm^{-1}, other $\beta_{pL} = 0$ cm^{-1}. For a negative bias, more than half of the tunneling electrons' spins are reversed by the triangle's toroidal spin texture.

rates from the spin-polarized source lead, but only minor selectivity in the discharging rates to the unpolarized drain lead, thus the forward spin-up and spin-down drain currents mostly cancel each other out. By contrast, for a reverse bias voltage and ferromagnetic Hund coupling, spin-down electrons from the drain prefer to tunnel onto clockwise states, while spin-up electrons from the drain prefer to tunnel onto counterclockwise states. The excess population in the clockwise states for a reverse bias means that more spin-down electrons will flow (backwards) through the drain than spin-up electrons. (Note: The redox-neutral clockwise states are selectively regenerated upon discharging spin-up electrons to the source lead.)

Because both phenomena are caused by spin-transfer torque, the extent of this spin-switching effect follows a pattern similar to the extent of population splitting. For example, the strength of spin-switching increases for larger $|J_{H12}\ S|$, and the angular dependence of the spin currents resembles the angular dependence of the population splitting, see Figs. 6.5 and 6.8.

Similar behavior also occurs when $|J_{ex}| > |\lambda_{ex}|$ (i.e. in the $|\tau_{A\pm}\rangle$ doublet) and when $\frac{|\lambda_{ex}|}{8} < |J_{ex}| < |\lambda_{ex}|$ (i.e. in the $|\tau_{B\pm}\rangle$ doublet), but the extents of population splitting and spin switching are smaller than for $|J_{ex}| = |\lambda_{ex}|$, as the ground states in those regimes have smaller toroidal moments, see Figs. 6.9 and 6.10. Another key difference is that none of the spin textures of the redox-neutral or singly-reduced states arising

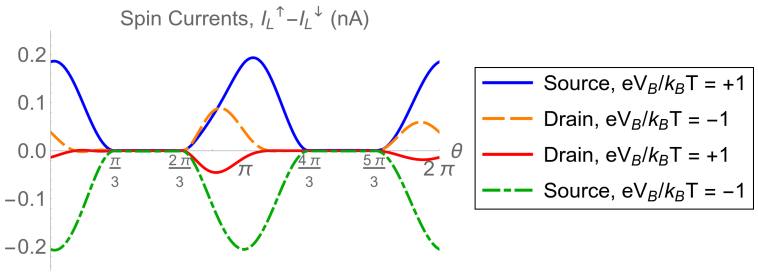

Figure 6.8: Spin currents vs. in-plane angle of rotation θ relative to the geometry shown in Fig. 6.3, using $S = \frac{7}{2}$, $S_3 = \frac{1}{2}$ and $|J_{ex}| = |\lambda_{ex}| \gg J_{H12}\ S > J_{H3}\ S_3$, t_{12}, t_3, β_{pL}, eV_B, k_BT, with $\rho_{S\uparrow} = 1$ cm, $\rho_{S\downarrow} = 0$ cm, $\rho_{D\uparrow} = \rho_{D\downarrow} = 0.5$ cm. The tunneling amplitudes β_{pL} are the same as in Fig. 6.5, but with proportionality constants of 0.2 cm^{-1}.

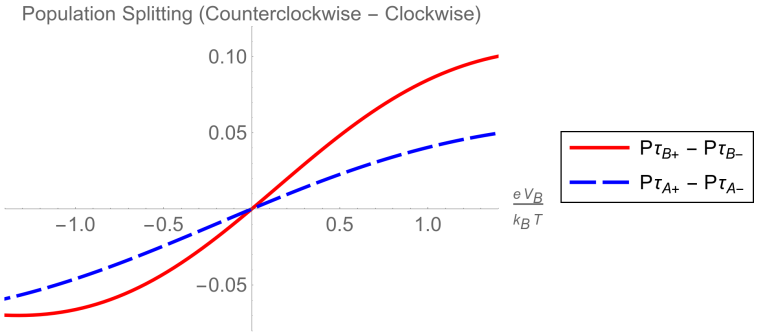

Figure 6.9: Nonequilibrium population splitting vs. bias voltage in the A and B doublets vs. bias voltage, using $\theta = \pi$ and $J_{H12} > J_{H3}$, t_{12}, t_3, β_{pL}, eV_B, k_BT.

from the A or B doublets depend on the value of S, so the behavior of the spintronics device in those regimes is also independent of S.

6.5 Conclusion

Both from the perspective of fundamental interest and practical applicability, toroidal states are an exciting field of study. By predicting the existence of toroidal ground states in isosceles spin triangles, we have extended the number of candidate molecules without spin-orbit coupling well beyond the equilateral spin $\frac{1}{2}$ case.

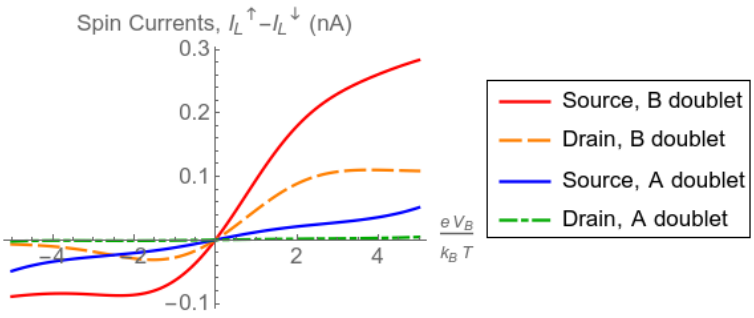

Figure 6.10: Spin currents vs. bias voltage for the A and B doublets, using $\theta = \pi$ and $J_{H12} > J_{H3}$, t_{12}, t_3, β_{pL}, eV_B, k_BT, with $\rho_{S\uparrow} = 1$ cm, $\rho_{S\downarrow} = 0$ cm, $\rho_{D\uparrow} = \rho_{D\downarrow} = 0.5$ cm, $\beta_{1D} = \beta_{2S} = 0.1$ cm^{-1}, other $\beta_{pL} = 0$ cm^{-1}.

When the exchange interactions between each of the spins are equal, four distinct toroidal states can be produced from the frustrated ground manifold. In the case where not all the couplings are equal, there are still toroidal moments in the ground doublets. In each scenario, we obtain analytical expressions for the toroidal moments for any values of the spins, provided $S_1 = S_2$.

This family of molecules may also be used in a tunneling spintronics device to reverse the polarization of an injected spin current and simultaneously produce a net toroidal magnetization on the triangle − a property which has exciting possibilities for high-density data storage.

6.6 Acknowledgements

S.V.R. acknowledges a Melbourne International Research Scholarship and Melbourne International Fee Remission Scholarship through the Melbourne India Postgraduate Program. J.M.A. acknowledges financial support from an Australian Government Research Training Program scholarship. A.S. thankfully acknowledges support from the Australian Research Council, Future Fellowship No. FT180100519.

Chapter 7

Toroidal Moment in Extended Spin-Frustrated Metal Rings

7.1 Introduction

We have discussed in previous chapter [104] triangular molecular nanomagnets that can carry a toroidal moment as a consequence of spin-frustration, with no need of strong spin-orbit coupling, also in the limit in fact of zero spin-orbit coupling. In this chapter we want to investigate the possibility of having toroidal moments in spin frustrated rings, having more than 3 metal centres.

The obvious starting point to look for larger rings with a toroidal moment in the ground state arising solely from spin-frustration is to look at the family of odd-membered nearest-neighbour Heisenberg antiferromagnetic rings, with half-odd integer spin on site. These systems obviously lead to spin frustrated ground states, for the same reason an antiferromagnetic spin triangle with spin half on site leads to a spin-frustrated ground state [103]. Interestingly however, the first result that will be reported here is that no toroidal moment can exist in the four-fold degenerate spin frustrated ground state of any odd membered N-ring with $N > 3$, if only nearest neighbour antiferromagnetic exchange is considered. We will see instead that a

four-fold degenerate spin frustrated excited state exists having a toroidal moment.

Hence, the next obvious generalization of our model for a spin frustrated extended ring toroic was to introduce new mechanisms in the Heisenberg exchange Hamiltonian in order to investigate the possibility of bringing the previously identified toroidal excited state into the ground state. We actually achieved this by introducing next-nearest neighbour coupling, which led to the definition in particular of two new families of toroics based on spin frustrated odd-membered antiferromagnetic Heisenberg rings with more than three centres.

Finally, we were also able to identify a special topological structure of the local spin texture of the novel spin-frustrated toroidal states, which suggests that toroidal states can only be achieved in antiferromagnetic spin-frustrated states where the collinear spin texture is such that longer-range ferromagnetic islands covering several adjacent magnetic centres will form, so to effectively realize an antiferromagnetic triangular spin texture covering the full extent of the ring.

7.2 Theoretical Background

Let us consider a ring with N spin centres, exchange coupled via a Heisenberg Hamiltonian with Nearest and Next-Nearest neighbour interactions, which reads:

$$\hat{H} = \sum_{i}^{n} J_{i,i+1}(\hat{S}_i \cdot \hat{S}_{i+1}) + \sum_{i}^{n} J_{i,i+2}(\hat{S}_i \cdot \hat{S}_{i+2}) \tag{7.1}$$

where,

$$\frac{|\text{Next-Nearest}|}{|\text{Nearest}|} = \frac{|J_{i,i+2}|}{|J_{i,i+1}|} = R_J \tag{7.2}$$

and

$$\hat{S}_{N+1} = \hat{S}_1 \tag{7.3}$$

$$\hat{S}_{N+2} = \hat{S}_2 \tag{7.4}$$

If the on-site spin length is half-odd integer [103], this is a generalization of the paradigmatic spin-frustrated triangle, thus expected to display extra-degeneracy in the ground state, consisting of two degen-

erate S=1/2 doublets, leading to an overall quartet. The possibility to realize a toroidal spin texture in this generalized spin-frustrated ground state is explored by diagonalizing within this four-fold degenerate ground state the toroidal moment operator, given by:

$$\hat{\tau_z} = (\vec{r_i} \times \vec{S_i})_z = \sum_i^n x_i S_i^y - y_i S_i^x \tag{7.5}$$

$$= \sum_i^n (\frac{-y_i - ix_i}{2}) S_i^+ + (\frac{-y_i + ix_i}{2}) S_i^- \tag{7.6}$$

The resulting pairs of eigenvalues (each pair consisting of opposite real values $\pm\tau_i$, due to the time-odd symmetry of any magnetic multipole operator) correspond, when different from zero, to measurable values of the toroidal moment in the associated states, while the eigenvectors provide indications about the detailed magnetic texture of the associated toroidal state. The magnetic texture of the toroidal states can be exposed by analysing the expectation value of the tangential on-site spin operator, given by:

$$\langle S_i^t \rangle = -\sin(\alpha_i)\langle S_i^x \rangle + \cos(\alpha_i)\langle S_i^y \rangle \tag{7.7}$$

$\langle S_i^t \rangle$ is the average on-site tangential moment, i is the site number and $\alpha_i = 2\pi(i-1)/N$ is the angular position of centre i along an idealized equilateral geometry of the ring, made of N equally spaced centres along the circumference circumscribing the polygonal ring.

Thus in this study we proceed by (i) building and diagonalizing Hamiltonian Eq. (7.1) for a range of R_J values, then (ii) use the eigenvectors associated to the degenerate ground quartet to compute the toroidal moment Eq. (7.5) eigenvalues and eigenvectors, and (iii) analyse the magnetic texture associated to both the four ground collinear exchange eigenstates of Eq. (7.1), and the four non-collinear toroidal eigenstates of operator Eq. (7.5), by computing and plotting the expectation values of local spin operators, namely the z-component $< S_i^z >$, and the in-plane tangential component Eq. (7.7), respectively, to try and characterize the origin of the toroidal nature of the ground quartet.

7.3 Families of frustrated spin rings explored

Previous studies on spin rings in the strong spin-orbit coupling regime [94], and in particular of spin triangles [43,95,96,103–105,111,113–115] have shown that in order to obtain a toroidal ground state essential ingredients are (i) a ring exchange connectivity of the spin system (ii) either on-site strong magnetic anisotropy with a magnetic axis lying in the rings plane and tangential to the rings circumference [94–96,101], or spin frustrated systems in the case of spin triangles in the weak spin-orbit coupling regime [100,103,104].

As mentioned above, we consider odd-membered spin rings with half-odd integer on-site spin length, and only nearest neighbour antiferromagnetic exchange coupling (ensuring the spin frustrated character of the system, and the ensuing 4-fold degeneracy in the ground state which revealed essential in the previous Chapter). We will label this infinite family of rings as Family 1. Then, we will proceed studying the effect of next-nearest neighbour coupling in the following families of exchange ring connectivities:

Family 2: Odd-membered rings with nearest neighbour interaction as ferromagnetic and next-nearest neighbour interaction as antiferromagnetic

Family 3: Odd-membered rings with nearest neighbour interaction as antiferromagnetic and next-nearest neighbour interaction as antiferromagnetic

We chose only combinations which are antiferromagnetic in the next-nearest neighbour interaction as having a case ferromagnetic interaction in the next-nearest neighbour would only reinforce the effect of nearest neighbour exchange, and hence would yield a similar ground state to a non-frustrated purely ferromagnetic or a purely antiferromagnetic nearest neighbour exchange. The former is not frustrated and the latter coincides with the ground state as Family 1.

Family	Nearest Neighbour	Next-Nearest Neighbour	Sites
1	A	-	odd $\geqslant 3$
2	**F**	**A**	**odd $\geqslant 5$**
3	A	A	odd $\geqslant 5$

Table 7.1: Summary of the families under consideration

These families, summarized by Table 7.1 and Figure 7.1, differ in exchange connectivity rather than

structure. The next-nearest neighbour exchange was always kept antiferromagnetic and its magnitude was varied systematically with respect to the nearest neighbour exchange as function of R_J, which results in a change of electronic structure.

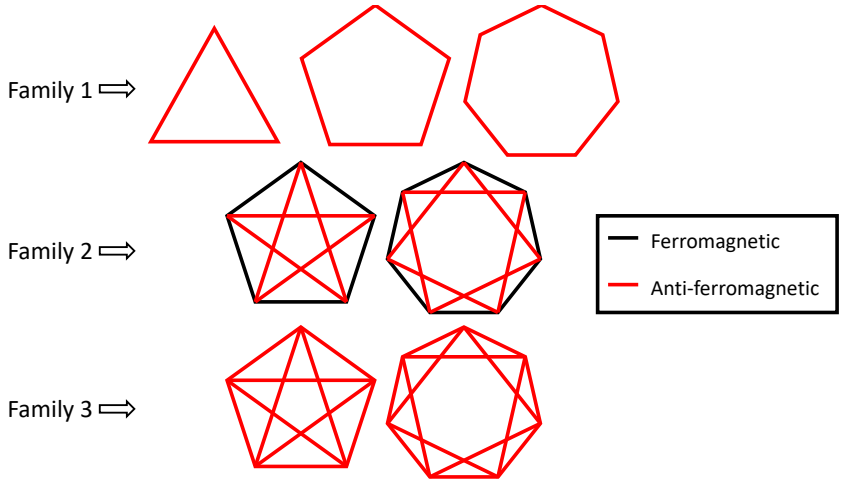

Figure 7.1: Structure and connectivities of families under consideration

7.3.1 Family 1: Antiferromagnetic odd-membered N-rings, with $N > 3$

For the five-membered antiferromagnetic ring of Family 1, it was found that a non-toroidal pair of frustrated spin 1/2 states constitute the ground state. Upon diagonalization of the toroidal moment operator within the quartet ground state, we find that all eigenvalues are zero. Interestingly, by systematically carrying out the diagonalization of the toroidal moment operator over all degenerate exchange manifolds, we found that there exists an excited quartet [see Figure 7.2, fourth energy level] which can display a toroidal moment. We will later show that this excited toroidal state can become the ground state by introducing particular combinations of nearest neighbours and next nearest neighbours exchange coupling constants (giving rise to what we will call Family 2). However, with just antiferromagnetic nearest neighbour interactions in Family 1 systems, odd membered N-rings with $N > 3$ have a ground quartet that is frustrated but incapable of showing toroidal moments.

While the reasons for the impossibility of creating a toroidal texture in spin-frustrated rings with more

than 3 centres is at the moment unclear, we have carefully checked this statement for odd-membered rings with N up to 11 centres, and the ground frustrated quartet is never able to support a toroidal moment, even when the on-site spin length is varied from $S_i = 1/2$ up to $S_i = 7/2$

The energy spectrum of the five-membered system is given in Figure 7.2 and, the ground state eigenvectors are given in the Appendix. B.1

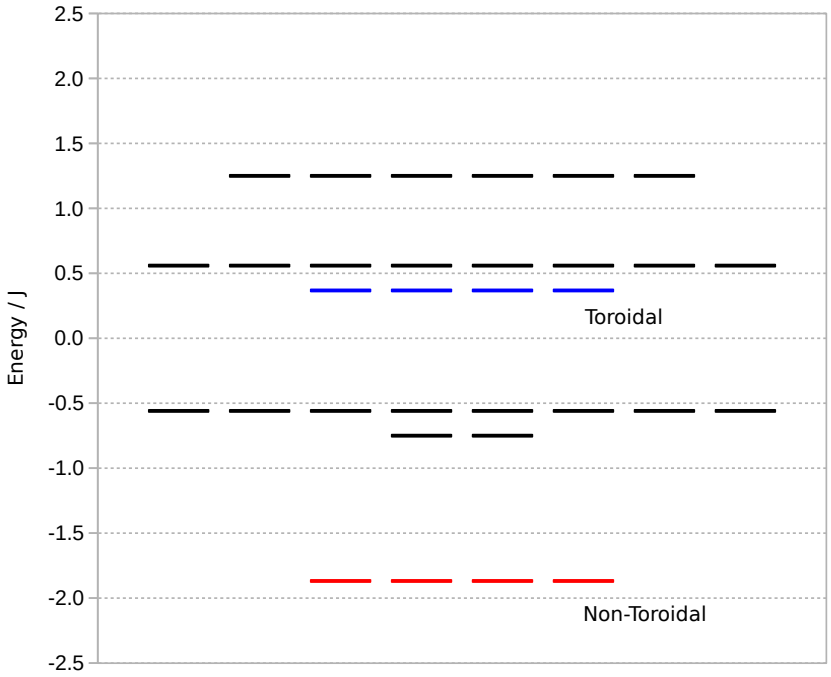

Figure 7.2: Energy $/J_{i,i+1}$ for the states of 5-membered, ring of Family 1, while the ground state has a quartet that doesn't show toroidal moment on diagonalization, the excited quartet can show toroidal moment

It is clear from these that there are six degenerate levels that exist in five membered rings.

An increase of site spin from spin 1/2 to spin 3/2, 5/2 and 7/2 showed similar trend (see Appendix B.2). Only the 3-membered ring of this family, a special case of the family of triangles discussed in Chapter 6, is capable of sustaining a toroidal moment in the ground quartet solely as a consequence of spin-frustration.

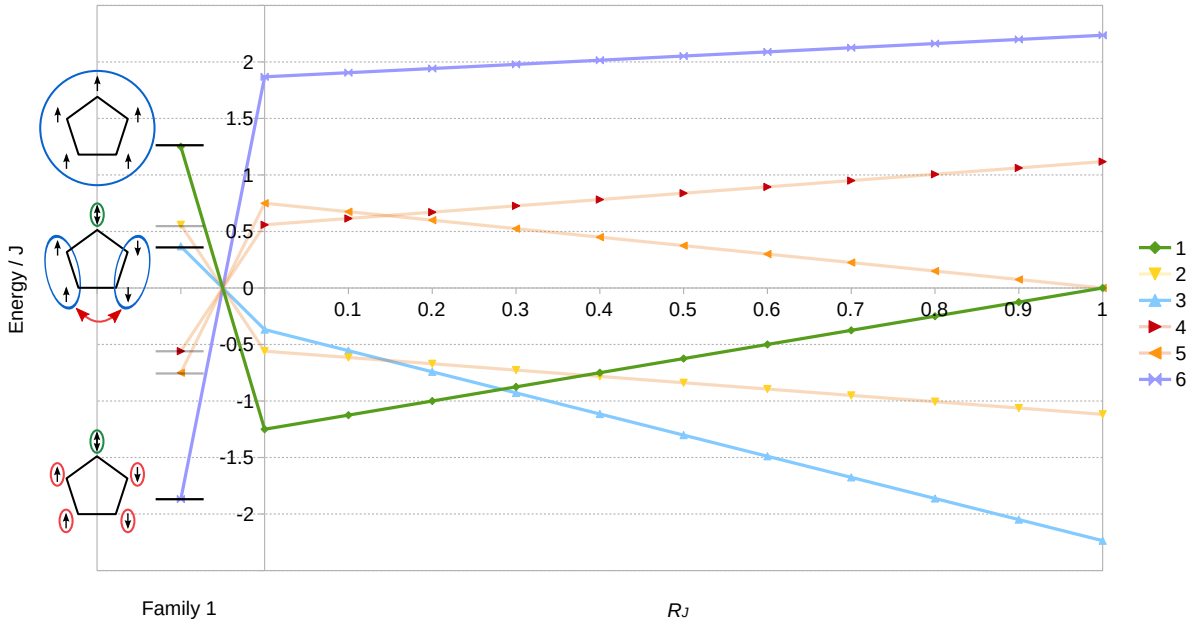

Figure 7.3: Energy $/J_{i,i+1}$ spectrum of degenerate states in the 5-membered Family 2 ring as a function of R_J. The 0 point on the x-axis shows the purely ferromagnetic case with only nearest neighbour exchange. To the left of $R_J = 0$ we report the energy levels for Family 1 (i.e. only antiferromagnetic nearest neighbour exchange).

7.3.2 Family 2 Rings

The case of the rings belonging to Family 2 is most notable. In this case, both frustration and toroidal moments are present in the ground quartet for particular ranges of R_J.

The simplest case within Family 2 is that of the five membered ring. In the graph of Figure 7.3 we can see the variation in the energy levels is shown as a function of R_J.

It is helpful to start at the purely ferromagnetic case where all the spins are aligned parallel to each other, this correspond to the point $R_J = 0$ in Figure 7.3. To the left of the purely ferromagnetic state we see the purely antiferromagnetic nearest neighbour exchange i.e. Family 1, 5-membered rings. On the other hand, if we look to the right side of the purely ferromagnetic state the next-nearest neighbour antiferromagnetic exchange is gradually switched on till it is equal in magnitude to the ferromagnetic exchange, corresponding

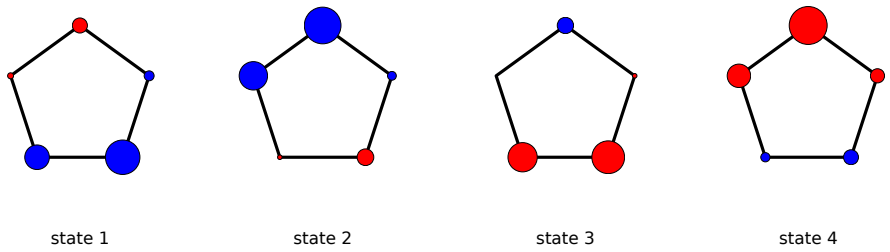

Figure 7.4: Site $< S_i^z >$ for the four eigenstates of the ground state quartet in the 5-ring (Family 2) for $R_J > 0.25$ (toroidal quartet). Blue (red) circles correspond positive (negative) values of $< S_i^z >$, while the area of the circle is proportional to the magnitude of $| < S_i^z > |$.

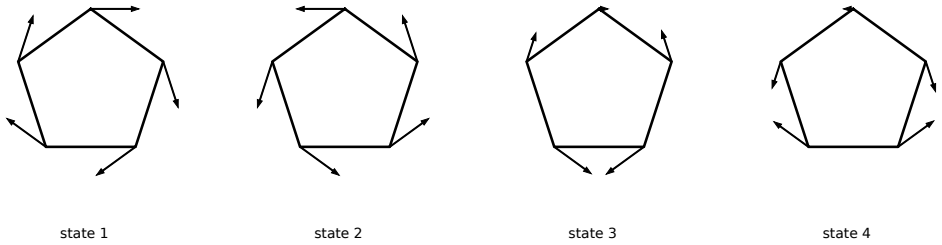

Figure 7.5: Site $\langle S_i^t \rangle$ tangential spin components for frustrated and toroidal (5-Site, Family 2, $R_J > .25$) ring over the lowest eigenvectors of the total toroidal moment operator τ_z.

to the 5-membered rings of Family 2 for various values of R_J.

As the next-nearest neighbour interaction becomes increasingly larger the eigenstates shift in energy. Remarkably, at $R_J = 0.25$ we find a level crossing between the ground quartet of Family 1, and the toroidal frustrated fourth excited quartet of Family 1, so that the ground state quartet of Family 2 becomes for $R_J > 0.25$ a spin frustrated toroidal ground quartet. The toroidal moments generated in this system are $\tau_Z = (1.3333333, -1.3333333, 0, 0)$

When we analyse the $\langle S_i^z \rangle$ expectation values we find that the purely ferromagnetic state breaks into smaller regions that have similar value of $\langle S_i^z \rangle$ (Figure 7.4). We will come back to this point when we

describe the seven membered rings later on. But such spin texture, is reminiscent of the paradigmatic antiferromagnetic spin-triangle, in that we always find two points along the ring where the sign of $< S_i^z >$ changes, just like we would find in a frustrated triangle. We can see from Figure 7.4 that the toroidal quartet that becomes the ground state for $R_J > 0.25$ is characterised by a partition of the collinear $< S_i^z >$ spin texture into three regions (some of which delocalised over more than one metal), two of which having the same sign, just like one would observe at the atomic level for a frustrated spin triangle. Of course, we must be careful to note that these regions are not the same as thermodynamic magnetic domains. These are neighbouring regions of parallel spin within a particular quantum state.

We see in Figure 7.5 that the tangential components of the spin at a given site over the basis of the toroidal states are equal across the sites for state 1 and state 2. States 3 and 4 each produce a net toroidal moment of 0. For the 7-membered ring case, (Figure 7.6), once again, the $R_J = 0$ case correspond to the purely

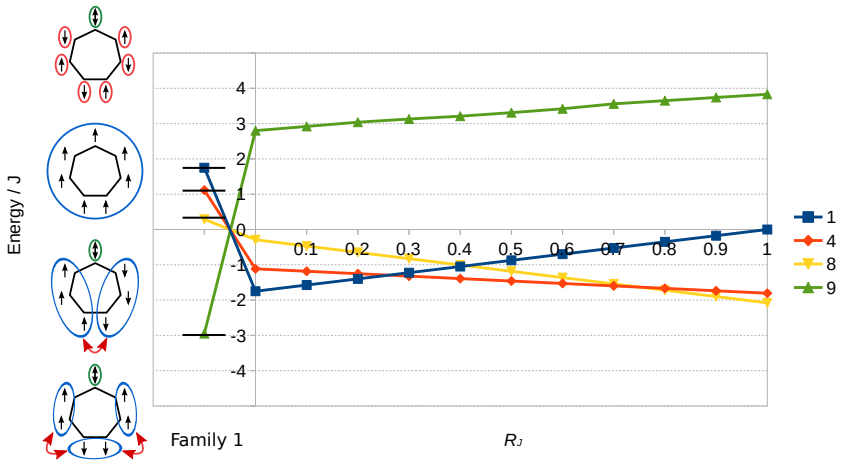

Figure 7.6: Energy/$J_{i,i+1}$ spectrum of key degenerate states in the 5-membered Family 2 ring as a function of R_J

ferromagnetic ring, as expected for a ferromagnetic nearest neighbour interaction and zero next-nearest neighbour interaction. On the left of $R_J = 0$ in Figure 7.6 we report the energy levels for a 7-membered ring belonging to Family 1. On systematically increasing the value of R_J we find that two level crossings occur in the case of the seven membered ring. The first level crossing is at $R_J = .25$ and ground state $\langle S_i^z \rangle$ breaks into

3 regions of neighbouring parallel spin (Figure. 7.7, 7.8). However, at $R_J = .56$ the $\langle S_i^z \rangle$ further breaks down into 4 regions of neighbouring parallel $\langle S_i^z \rangle$. Once again, by direct numerical calculation we find that the range of R_J values for which $< S_i^z >$ breaks down into three antiparallel multinuclear domains, corresponding here to $0.25 < R_J < 0.56$, mimics a frustrated local spin texture reminiscent of the frustrated ground quartet of a spin triangle, and gives rise to a ground state quartet that can sustain a toroidal moment. In particular, direct diagonalization of the toroidal moment operator gives in this case $\tau_z = (1.6576393, -1.6576393, 0, 0)$.

Similar results are found for 9-membered rings where the range of $0.26 < R_J < 0.33$ for which the frustration occurs is much smaller (see Appendix B.2,B.4). For the 9-membered ring, as well, the collinear spin texture of the exchange ground quartet that can sustain a toroidal moment displays $< S_i^z >$ domains of parallel local spins, reminiscent of the frustrated spin triangle magnetic texture, and leads to the following toroidal eigenvalues $\tau_z = (1.985255, -1.985255, 0, 0)$.

In summary, the possible antiferromagnetic ground state quartets for the odd membered rings explored here belonging to Family 2 present the following eigenvalues of the toroidal moment operator:

- 5-membered Ring, $1.00 > R_J > 0.25$: τ_Z =(1.3333333, -1.3333333, 0, 0)
- 7-membered Ring, $0.56 > R_J > 0.25$: τ_Z =(1.6576393, -1.6576393, 0, 0)
- 7-membered Ring, $1.00 > R_J > 0.56$: τ_Z =(0, 0, 0, 0)
- 9-membered Ring, $0.33 > R_J > 0.26$: τ_Z =(1.985255, -1.985255, 0, 0)
- 9-membered Ring, $1.00 > R_J > 0.33$: τ_Z =(0, 0, 0, 0)

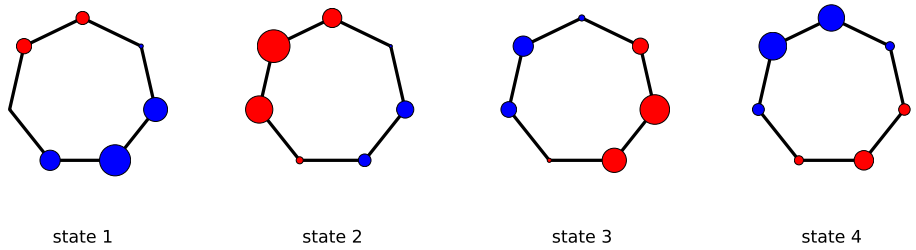

Figure 7.7: Site $< S_i^z >$ for the four eigenstates of the ground state quartet in the 7-ring (Family 2) for $0.56 > R_J > 0.25$ (toroidal quartet). Blue (red) circles correspond positive (negative) values of $< S_i^z >$, while the area of the circle is proportional to the magnitude of $| < S_i^z > |$.

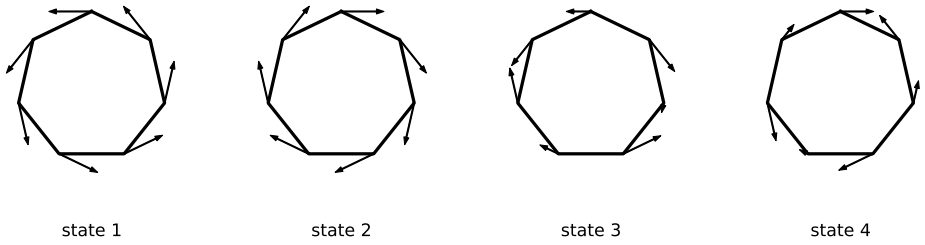

Figure 7.8: Site $\langle S_i^t \rangle$ tangential spin components for frustrated and toroidal (7-Site, Family 2, $0.56 > R_J > 0.25$) ring over the lowest eigenvectors of the total toroidal moment operator τ_z

7.3.3 Family 3 Rings

Family three gives a 10 fold degenerate state for a spin 1/2, 5-membered ring at a very specific value for the ratio of next-nearest to nearest interaction, $R_J = 1$ which is highly sensitive to value of R_J, these states do give a toroidal moment upon diagonalization (Figure. 7.10). We see that upon even a small variation of R_J of just $\Delta R_J = 0.1$ the degeneracy becomes only pseudo degenerate (Figure. 7.14 and 7.13). We shall see that a similar result is also true for the $S_i = 3/2$ case.

This 10 fold degeneracy in the ground state increased to 40 fold when the site spin was increased to 3/2. These 40 fold degenerate states (Figure. 7.11) displayed toroidal moments. (Figure 7.12). Once again, a $\Delta R_J = 0.01$ broke the degeneracy. Such a specific value of R_J makes the engineering and synthesis of an appropriate spin ring difficult, however a pseudo degeneracy spread over an energy range comparable to the temperature would suffice to achieve a toroidal moment in this large pseudo-degenerate manifold. Recent wheels reported in the literature appear to have similar magnitude of nearest and next nearest neighbour coupling constants, albeit in an even membered ring [148]

Larger sized rings show a ground quartet with no toroidal moments similar to Family 1.

The Toroidal Moments of Family 3 are:

- 5-site, Spin 1/2:

  τ_Z =(±1.3333333, ±0.8164965, ±0.8164965, ±0.3333332, ±0.3333333)

- 5-site, Spin 3/2:

  τ_Z =(±3.0000000, ±2.6312709, ±2.6312710, ±2.2496977, ±2.2496976, ±2.1140638, ±1.7202571, ±1.7202569, ±1.5275251, ±1.5275253, ±1.0701132, ±1.0701133, ±1.0491692, ±0.9351054, ±0.7732639, ±0.7732639, ±0.8038925, ±0.8038925, ± 0.3333332, ±0.3333332)

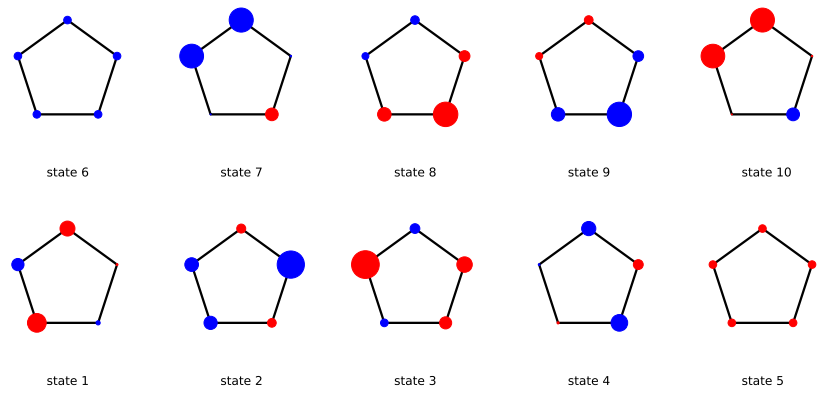

Figure 7.9: Site $< S_i^z >$ for the four eigenstates of the ground state quartet in the $S_i = 1/2$ 5-ring (Family 2) for $R_J = 1$ (ten toroidal states). Blue (red) circles correspond positive (negative) values of $< S_i^z >$, while the area of the circle is proportional to the magnitude of $| < S_i^z > |$.

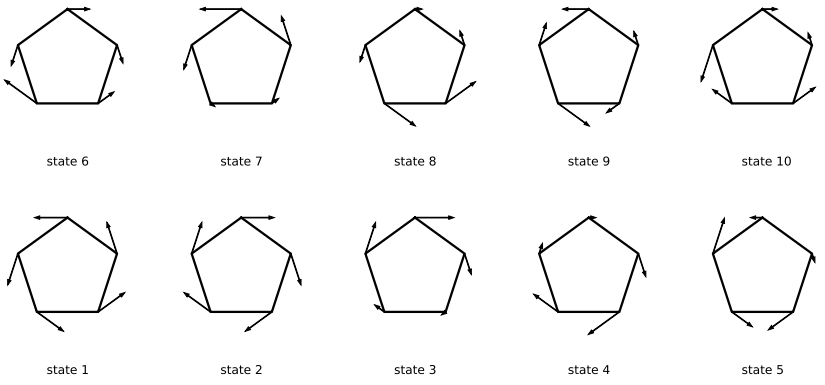

Figure 7.10: Site $\langle S_i^t \rangle$ tangential spin components for Frustrated and toroidal(5-Site, Family 3, $S_i = 1/2$, $R_J = 1$) ring over the lowest eigenvectors of the total toroidal moment operator τ_z

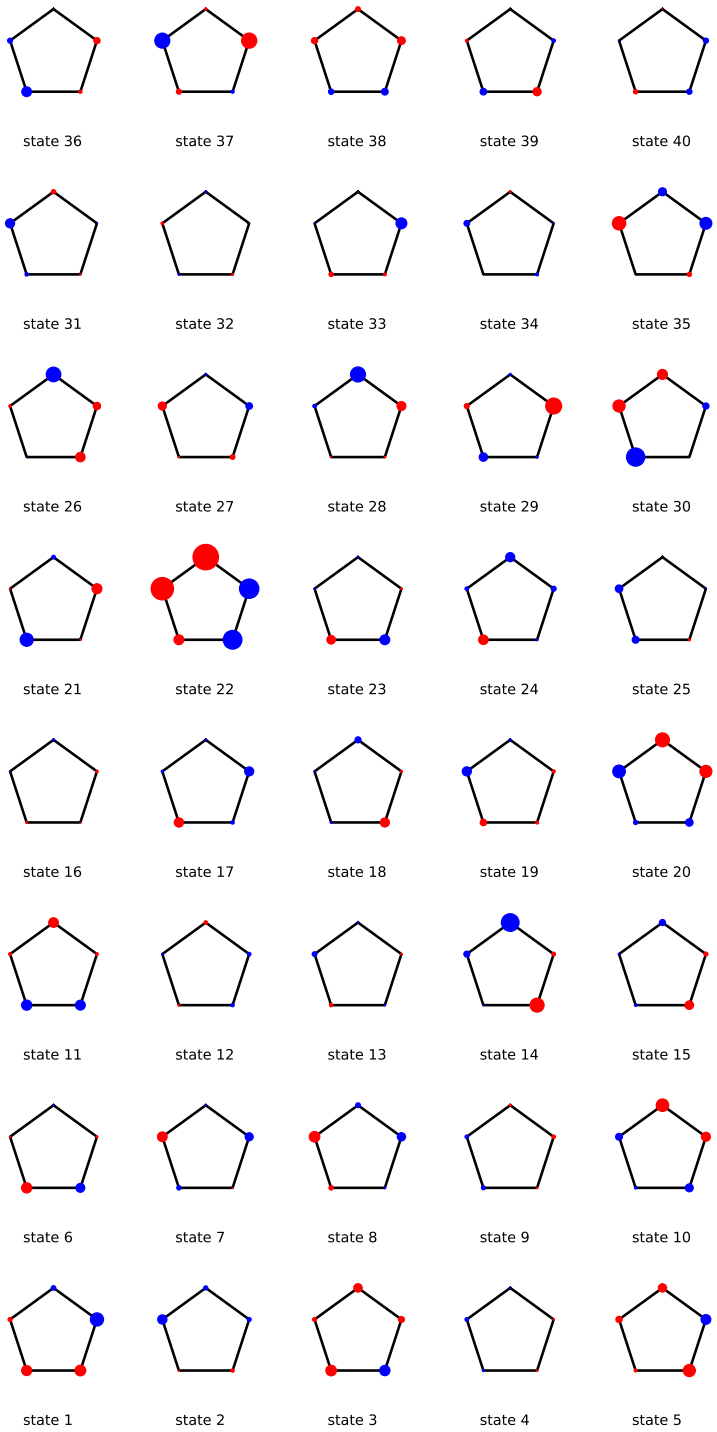

Figure 7.11: Site $< S_i^z >$ for the four eigenstates of the ground state quartet in the $S_i = 3/2$ 5-ring (Family 2) for $R_J = 1$ (forty toroidal states). Blue (red) circles correspond positive (negative) values of $< S_i^z >$, while the area of the circle is proportional to the magnitude of $| < S_i^z > |$

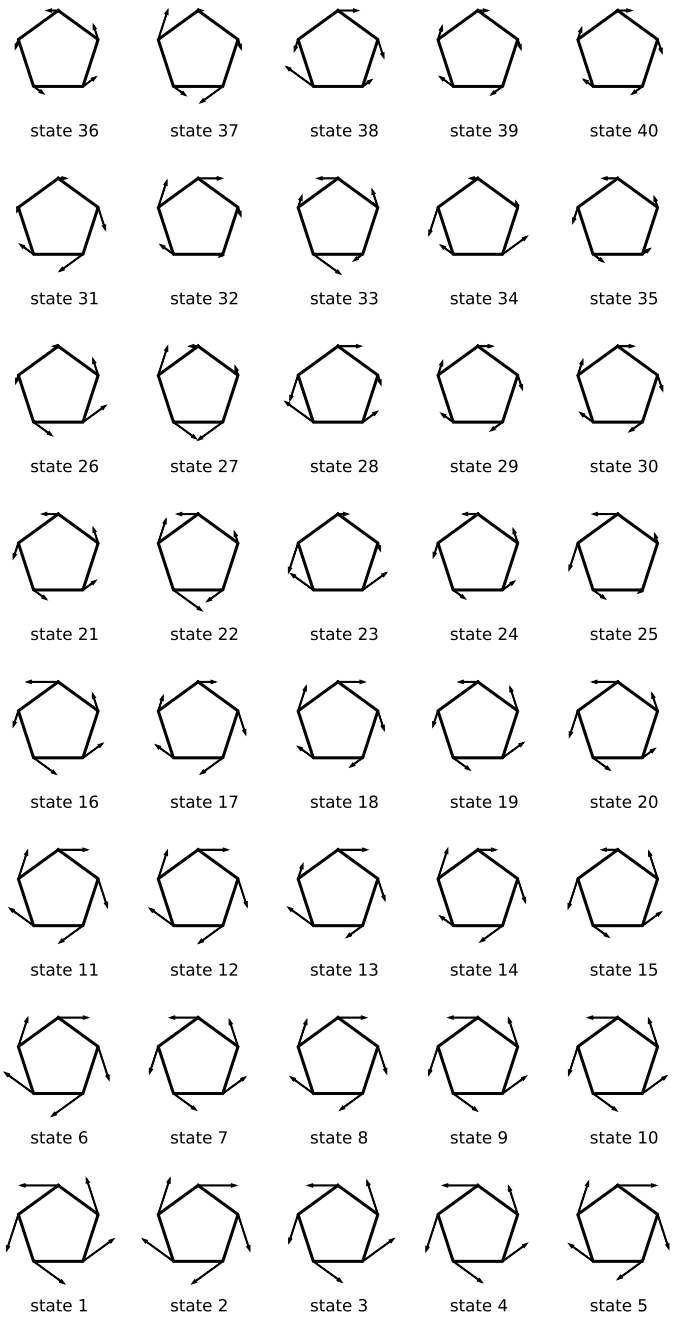

Figure 7.12: Site $\langle S_i^t \rangle$ tangential spin components for frustrated and toroidal(7-Site, Family 2, $0.56 > R_J > 0.25$) ring over the lowest eigenvectors of the total toroidal moment operator τ_z

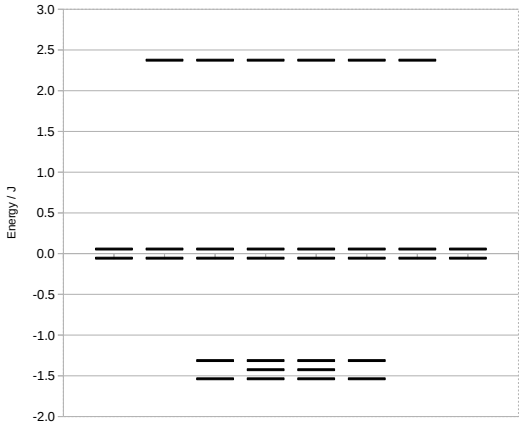

Figure 7.13: Energy spectrum for Frustrated and toroidal (5-Site, Family 5, $S_i = 1/2$, $R_J = 0.9$) where many states are no longer degenerate compared to the $R_J = 1.0$ case

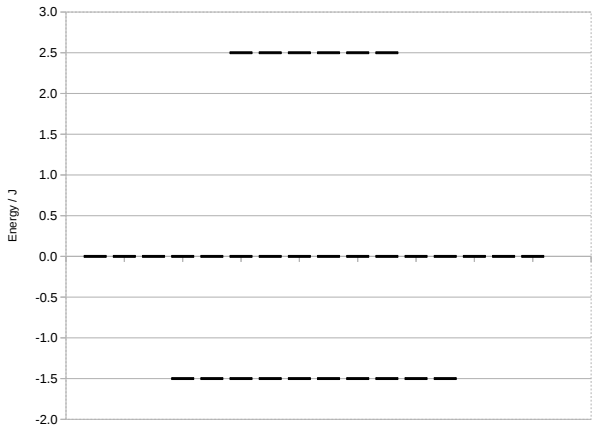

Figure 7.14: Energy spectrum for Frustrated and toroidal (5-Site, Family 5 $S_i = 1/2$, $R_J = 1.0$) where many states are now degenerate compared to the $R_J = 0.$ case

7.4 Discussion

Family	Frustration	Toroidal Moment
1	Present for all	Present for 3 site rings
2	**Present for some R_J**	**Present for some R_J**
3	Frustrated	Present for $R_J = 1$

Table 7.2: Summary of the results

Table 7.2 is a summary of the results of the study. Within, Family 1 both heterogeneous and homogeneous site spins yielded toroidal moments with the latter showing higher number of toroidal states. Family 3 showed the highest number of toroidal states over all but was found highly sensitive to values of R_J.

Family 2 showed stable degeneracies over ranges of R_J. This range of values became smaller with growing ring size. This range was found to be $0.25 \leq R_J$ for 5-membered rings, $0.25 \leq R_J \leq 0.56$ for 7-membered rings and $0.26 \leq R_J \leq 0.33$ for 9-membered rings.

When we examine the topology of the spins in the eigenvectors of the Hamiltonian Family 2, we found that the exchange states sustaining a toroidal moment have a collinear spin textures (as probed by expectation values of local S_i^z operators) that are reminiscent of that of frustrated spin triangle from Family 1.

Chapter 8

Conclusions

In addition to magnetic moments, higher magnetic multipoles become relevant for the description of the ground state magnetism of molecular nanomagnets that are fascinating objects of study. One such property is the toroidal moment. Toroidal moment is an operator that naturally appears as a component of quadrupole part in the the multipolar expansion of the vector potential associated to a collection of magnetic moment, such as on-site spin moments on a spin rings. In particular, the toroidal moment is the antisymmetric part of a general quadrupole moment associated to a collection of localised magnetic moments. In a spin ring this can be understood as the sum of the tangential components of the spin multiplied by their distance from the center. It is possible to produce special states in molecules which are purely toroidal, i.e. they have zero total magnetic moment, but a non-zero toroidal moment, which in such instances is the first non-zero magnetic multipole in the multipolar expansion. In the previous two chapters making up the second part of this Ph.D. thesis, I was able to identify three new infinite families of molecules displaying a non-zero toroidal moment in the ground state, solely as result of spin-frustration, i.e. with zero spin-orbit coupling (hence zero magnetic anisotropy). Such a toroidal state would only interact with the curl component of an external magnetic field and would be unaffected by the presence of a homogeneous magnetic field. Also, given that it is a quadrupole moment, its interaction with neighbouring quadrupole moments falls off quicker with distance than the interaction between two magnetic dipole moments, which in principle could allow for denser packing

of molecular toroidal moments i.e on the surface of a molecular device. Both these properties are potentially useful to develop new strategies to design and fabricate dense storage devices for molecular nanomagnets. In previous literature, toroidal states have mostly been discussed for molecular magnets within the strong magnetic anisotropy (i.e. strong spin-orbit coupling) regime. In the limit of weak spin-orbit coupling/weak magnetic anisotropy toroidal states have only been described for a triangular ring with on-site spin length of s=1/2. Larger antiferromagnetic rings analogous to the antiferromagnetic triangle have been shown here for the first time (Chapter 7) to be incapable of displaying a toroidal moment in the ground quartet, as consequence of pure spin-frustration (i.e. in the weak spin-orbit coupling limit). Do not display a toroidal moment in the ground quartet. In Chapter 6 we have then shown that a toroidal moment in the ground quartet of these extended odd membered rings can be recovered if next nearest neighbour is considered.

Further systems that can display a toroidal moment im the ground state as a result of spin-frustration were identified in Chapter 6, where and infinite family of heterometallic spin triangles with arbitrary on site spin was identified as promising target, which should be easier to realize from the experimental point of view. we saw the effect of next-nearest neighbour interactions. It appears that with the right next-nearest neighbour interaction switched on, it is possible to reintroduce toroidal moment in larger ring systems.

Chapter 4 describes new possibilities for the observation toroidal moment. Firstly, we see that instead of only two toroidal states there is a possibility of 4 distinct toroidal states to be generated out of a frustrated quartet using specific geometry. It is also possible to obtain these states in the absence of inherent site anisotropy. Furthermore, the system has also been characterized in a molecular spintronics device where we can selectively change the equilibrium population of specific toroidal states.

Bibliography

[1] F. Neese and D. A. Pantazis, "What is not required to make a single molecule magnet," *Faraday Discussions*, vol. 148, pp. 229–238, dec 2011.

[2] A. Caneschi, D. Gatteschi, R. Sessoli, A. L. Barra, L. C. Brunel, and M. Guillot, "Alternating current susceptibility, high field magnetization, and millimeter band EPR evidence for a ground S = 10 state in [Mn12O12(Ch3COO)16(H2O)4].2CH3COOH.4H2O," *Journal of the American Chemical Society*, vol. 113, pp. 5873–5874, jul 1991.

[3] R. Sessoli, D. Gatteschi, A. Caneschi, and M. A. Novak, "Magnetic bistability in a metal-ion cluster," *Nature*, vol. 365, pp. 141–143, sep 1993.

[4] R. Sessoli, H. L. Tsai, A. R. Schake, S. Wang, J. B. Vincent, K. Folting, D. Gatteschi, G. Christou, and D. N. Hendrickson, "High-spin molecules: [Mn12O12(O2CR)16(H2O)4]," *Journal of the American Chemical Society*, vol. 115, pp. 1804–1816, mar 1993.

[5] D. Gatteschi, R. Sessoli, and J. Villain, *Molecular Nanomagnets*. Oxford University Press, Oxford, U.K., 2006.

[6] O. Kahn, *Molecular magnetism*. VCH, 1993.

[7] A.-L. Barra, P. Debrunner, D. Gatteschi, C. E. Schulz, and R. Sessoli, "Superparamagnetic-like behavior in an octanuclear iron cluster," *Europhysics Letters*, vol. 35, pp. 133–138, jul 1996.

[8] C. J. Milios, A. Vinslava, W. Wernsdorfer, S. Moggach, S. Parsons, S. P. Perlepes, G. Christou, and E. K. Brechin, "A Record Anisotropy Barrier for a Single-Molecule Magnet," *Journal of the American Chemical Society*, 2007.

[9] A. M. Ako, I. J. Hewitt, V. Mereacre, R. Clérac, W. Wernsdorfer, C. E. Anson, and A. K. Powell, "A Ferromagnetically Coupled Mn19 Aggregate with a RecordS=83/2 Ground Spin State," *Angewandte Chemie International Edition*, vol. 45, pp. 4926–4929, jul 2006.

[10] J. D. Rinehart and J. R. Long, "Exploiting single-ion anisotropy in the design of f-element single-molecule magnets," *Chemical Science*, vol. 2, no. 11, p. 2078, 2011.

[11] C. A. P. Goodwin, F. Ortu, D. Reta, N. F. Chilton, and D. P. Mills, "Molecular magnetic hysteresis at 60 kelvin in dysprosocenium," *Nature*, vol. 548, pp. 439–442, aug 2017.

[12] F.-S. Guo, B. M. Day, Y.-C. Chen, M.-L. Tong, A. Mansikkamäki, and R. A. Layfield, "Magnetic hysteresis up to 80 kelvin in a dysprosium metallocene single-molecule magnet.," *Science (New York, N.Y.)*, vol. 362, pp. 1400–1403, dec 2018.

[13] M. Bottrill, L. Kwok, and N. J. Long, "Lanthanides in magnetic resonance imaging," *Chemical Society Reviews*, vol. 35, p. 557, may 2006.

[14] L. Bogani and W. Wernsdorfer, "Molecular spintronics using single-molecule magnets," *Nature Materials*, vol. 7, pp. 179–186, mar 2008.

[15] S. Sanvito, "Molecular spintronics," *Chem. Soc. Rev.*, vol. 40, p. 3336, may 2011.

[16] M. N. Leuenberger and D. Loss, "Spin tunneling and phonon-assisted relaxation in Mn 12 -acetate," *Physical Review B*, vol. 61, pp. 1286–1302, jan 2000.

[17] N. Ishikawa, "Single molecule magnet with single lanthanide ion," *Polyhedron*, vol. 26, pp. 2147–2153, jun 2007.

[18] N. Ishikawa, M. Sugita, T. Okubo, N. Tanaka, T. Iino, and Y. Kaizu, "Determination of Ligand-Field Parameters and f-Electronic Structures of Double-Decker Bis(phthalocyaninato)lanthanide Complexes," *Inorganic Chemistry*, vol. 42, pp. 2440–2446, apr 2003.

[19] . Naoto Ishikawa, , . Miki Sugita, . Tadahiko Ishikawa, , . Shin-ya Koshihara, and Y. Kaizu, "Lanthanide Double-Decker Complexes Functioning as Magnets at the Single-Molecular Level," *Journal of the American Chemical Society*, 2003.

[20] . Naoto Ishikawa, *, . Miki Sugita, . Tadahiko Ishikawa, , . Shin-ya Koshihara, and . Youkoh Kaizu*, "Mononuclear Lanthanide Complexes with a Long Magnetization Relaxation Time at High Temperatures: A New Category of Magnets at the Single-Molecular Level," *Journal of the American Chemical Society*, 2004.

[21] D. N. Woodruff, R. E. P. Winpenny, and R. A. Layfield, "Lanthanide Single-Molecule Magnets," *Chemical Reviews*, vol. 113, pp. 5110–5148, jul 2013.

[22] J. Tang and Z. Peng, *Lanthanide Single Molecule Magnets*. London: Springer, 2015.

[23] A. Abragam and B. B. Bleaney, *Electron paramagnetic resonance of transition ions*. Oxford University Press, 2012.

[24] L. F. Chibotaru and L. Ungur, "Ab initio calculation of anisotropic magnetic properties of complexes. I. Unique definition of pseudospin Hamiltonians and their derivation," *The Journal of Chemical Physics*, vol. 137, p. 064112, aug 2012.

[25] L. Ungur and L. F. Chibotaru, "Ab Initio Crystal Field for Lanthanides," *Chemistry - A European Journal*, vol. 23, pp. 3708–3718, mar 2017.

[26] L. Ungur and L. F. Chibotaru, "Magnetic anisotropy in the excited states of low symmetry lanthanide complexes," *Physical Chemistry Chemical Physics*, vol. 13, p. 20086, nov 2011.

[27] R. Marx, F. Moro, M. Dörfel, L. Ungur, M. Waters, S. D. Jiang, M. Orlita, J. Taylor, W. Frey, L. F. Chibotaru, and J. van Slageren, "Spectroscopic determination of crystal field splittings in lanthanide double deckers," *Chemical Science*, vol. 5, p. 3287, jun 2014.

[28] M.-E. Boulon, G. Cucinotta, S.-S. Liu, S.-D. Jiang, L. Ungur, L. F. Chibotaru, S. Gao, and R. Sessoli, "Angular-Resolved Magnetometry Beyond Triclinic Crystals: Out-of-Equilibrium Studies of Cp*ErCOT Single-Molecule Magnet," *Chemistry - A European Journal*, vol. 19, pp. 13726–13731, oct 2013.

[29] J. Luzon and R. Sessoli, "Lanthanides in molecular magnetism: so fascinating, so challenging," *Dalton Transactions*, vol. 41, p. 13556, oct 2012.

[30] K. Bernot, J. Luzon, L. Bogani, M. Etienne, C. Sangregorio, M. Shanmugam, A. Caneschi, R. Sessoli, and D. Gatteschi, "Magnetic Anisotropy of Dysprosium(III) in a Low-Symmetry Environment: A Theoretical and Experimental Investigation," *Journal of the American Chemical Society*, vol. 131, pp. 5573–5579, apr 2009.

[31] K. Bernot, J. Luzon, A. Caneschi, D. Gatteschi, R. Sessoli, L. Bogani, A. Vindigni, A. Rettori, and M. G. Pini, "Spin canting in a Dy-based single-chain magnet with dominant next-nearest-neighbor antiferromagnetic interactions," *Physical Review B*, vol. 79, p. 134419, apr 2009.

[32] G. Cucinotta, M. Perfetti, J. Luzon, M. Etienne, P.-E. Car, A. Caneschi, G. Calvez, K. Bernot, and R. Sessoli, "Magnetic Anisotropy in a Dysprosium/DOTA Single-Molecule Magnet: Beyond Simple Magneto-Structural Correlations," *Angewandte Chemie International Edition*, vol. 51, pp. 1606–1610, feb 2012.

[33] J. Jung, O. Cador, K. Bernot, F. Pointillart, J. Luzon, and B. Le Guennic, "Influence of the supramolecular architecture on the magnetic properties of a Dy(III) single-molecule magnet: an ab initio investigation.," *Beilstein Journal of Nanotechnology*, vol. 5, pp. 2267–74, 2014.

[34] J. Jung, X. Yi, G. Huang, G. Calvez, C. Daiguebonne, O. Guillou, O. Cador, A. Caneschi, T. Roisnel, B. Le Guennic, and K. Bernot, "Analysis of the electrostatics in Dy III single-molecule magnets: the case study of Dy(Murex) 3," *Dalton Transactions*, vol. 44, pp. 18270–18275, oct 2015.

[35] K. Sharkas, B. Pritchard, and J. Autschbach, "Effects from SpinOrbit Coupling on ElectronNucleus Hyperfine Coupling Calculated at the Restricted Active Space Level for Kramers Doublets," *Journal of Chemical Theory and Computation*, vol. 11, pp. 538–549, feb 2015.

[36] P. Zhang, J. Jung, L. Zhang, J. Tang, and B. Le Guennic, "Elucidating the Magnetic Anisotropy and Relaxation Dynamics of Low-Coordinate Lanthanide Compounds," *Inorganic Chemistry*, vol. 55, pp. 1905–1911, feb 2016.

[37] A. Lunghi, F. Totti, R. Sessoli, and S. Sanvito, "The role of anharmonic phonons in under-barrier spin relaxation of single molecule magnets," *Nature Communications*, vol. 8, p. 14620, apr 2017.

[38] F. Gendron, B. Pritchard, H. Bolvin, and J. Autschbach, "Single-ion 4f element magnetism: an ab-initio look at Ln(COT) 2 ," *Dalton Transactions*, vol. 44, pp. 19886–19900, nov 2015.

[39] M. Vonci, M. J. Giansiracusa, R. W. Gable, W. Van den Heuvel, K. Latham, B. Moubaraki, K. S. Murray, D. Yu, R. A. Mole, A. Soncini, and C. Boskovic, "Ab initio calculations as a quantitative tool in the inelastic neutron scattering study of a single-molecule magnet analogue," *Chemical Communications*, vol. 52, pp. 2091–2094, jan 2016.

[40] N. F. Chilton, D. Collison, E. J. L. McInnes, R. E. P. Winpenny, and A. Soncini, "An electrostatic model for the determination of magnetic anisotropy in dysprosium complexes," *Nature Communications*, vol. 4, p. 2551, dec 2013.

[41] W. V. den Heuvel, S. Calvello, and A. Soncini, "Configuration-averaged 4f orbitals in ab initio calculations of low-lying crystal field levels in lanthanide(III) complexes," *Physical Chemsitry Chemical Physics*, sep 2015.

[42] F. Aquilante, J. Autschbach, R. K. Carlson, L. F. Chibotaru, M. G. Delcey, L. De Vico, I. Fdez. Galván, N. Ferré, L. M. Frutos, L. Gagliardi, M. Garavelli, A. Giussani, C. E. Hoyer, G. Li Manni, H. Lischka, D. Ma, P. Å. Malmqvist, T. Müller, A. Nenov, M. Olivucci, T. B. Pedersen, D. Peng, F. Plasser, B. Pritchard, M. Reiher, I. Rivalta, I. Schapiro, J. Segarra-Martí, M. Stenrup, D. G. Truhlar, L. Ungur, A. Valentini, S. Vancoillie, V. Veryazov, V. P. Vysotskiy, O. Weingart, F. Zapata, and R. Lindh, "Molcas 8: New capabilities for multiconfigurational quantum chemical calculations across the periodic table," *Journal of Computational Chemistry*, vol. 37, pp. 506–541, feb 2016.

[43] L. Ungur, S. K. Langley, T. N. Hooper, B. Moubaraki, E. K. Brechin, K. S. Murray, and L. F. Chibotaru, "Net Toroidal Magnetic Moment in the Ground State of a {Dy 6 }-Triethanolamine Ring," *Journal of the American Chemical Society*, vol. 134, pp. 18554–18557, nov 2012.

[44] B. O. Roos, P. R. Taylor, and P. E. Sigbahn, "A complete active space SCF method (CASSCF) using a density matrix formulated super-CI approach," *Chemical Physics*, vol. 48, pp. 157–173, may 1980.

[45] P. Å. Malmqvist, B. O. Roos, and B. Schimmelpfennig, "The restricted active space (RAS) state interaction approach with spinorbit coupling," *Chemical Physics Letters*, vol. 357, pp. 230–240, may 2002.

[46] R. McWeeny, "SCF theory for excited states," *Molecular Physics*, vol. 28, pp. 1273–1282, nov 1974.

[47] R. McWeeny and B. T. Sutcliffe, *Methods of molecular quantum mechanics*. Theoretical chemistry, San Diego: Academic Press, 1969.

[48] S. Calvello, M. Piccardo, S. V. Rao, and A. Soncini, "CERES: An ab initio code dedicated to the calculation of the electronic structure and magnetic properties of lanthanide complexes," *Journal of Computational Chemistry*, vol. 39, pp. 328–337, mar 2018.

[49] A. Soncini, S. Calvello, M. Piccardo, and S. V. Rao, "Ceres, an ab initio quantum chemistry package for the electronic structure and magnetic properties of lanthanide complexes," 2017.

[50] M. Piccardo and A. Soncini, "A full-pivoting algorithm for the Cholesky decomposition of two-electron repulsion and spin-orbit coupling integrals," *Journal of Computational Chemistry*, vol. 38, pp. 2775–2783, dec 2017.

[51] K. G. Dyall and K. Fægri, *Introduction to relativistic quantum chemistry.* Oxford University Press, 2007.

[52] A. Wolf, M. Reiher, and B. A. Hess, "The generalized DouglasKroll transformation," *The Journal of Chemical Physics*, vol. 117, pp. 9215–9226, nov 2002.

[53] A. Wolf and M. Reiher, "Exact decoupling of the Dirac Hamiltonian. IV. Automated evaluation of molecular properties within the Douglas-Kroll-Hess theory up to arbitrary order," *The Journal of Chemical Physics*, vol. 124, p. 064103, feb 2006.

[54] M. Reiher and A. Wolf, "Exact decoupling of the Dirac Hamiltonian. II. The generalized DouglasKroll-Hess transformation up to arbitrary order," *The Journal of Chemical Physics*, vol. 121, p. 10945, nov 2004.

[55] G. Breit, "The Effect of Retardation on the Interaction of Two Electrons," *Physical Review*, vol. 34, pp. 553–573, aug 1929.

[56] G. Breit, "Dirac's Equation and the Spin-Spin Interactions of Two Electrons," *Physical Review*, vol. 39, pp. 616–624, feb 1932.

[57] G. Breit and L. A. Wills, "Hyperfine Structure in Intermediate Coupling," *Physical Review*, vol. 44, pp. 470–490, sep 1933.

[58] B. A. Heß, C. M. Marian, U. Wahlgren, and O. Gropen, "A mean-field spin-orbit method applicable to correlated wavefunctions," *Chemical Physics Letters*, vol. 251, pp. 365–371, mar 1996.

[59] S.-D. Jiang, B.-W. Wang, G. Su, Z.-M. Wang, and S. Gao, "A Mononuclear Dysprosium Complex Featuring Single-Molecule-Magnet Behavior," *Angewandte Chemie*, vol. 122, pp. 7610–7613, aug 2010.

[60] B. Schimmelpfennig, "AMFI - An Atomic Mean Field Program," 1996.

[61] F. Neese, "The ORCA program system," *DescriptionWiley Interdisciplinary Reviews: Computational Molecular Science*, vol. 2, pp. 73–78, jan 2012.

[62] J. J. Sakurai, *Modern quantum mechanics*. Pearson Education, 2006.

[63] T. Helgaker, P. Jorgensen, and J. Olsen, *Molecular electronic-structure theory*. John Wiley & Sons, Ltd, 2000.

[64] A. Szabo and N. S. Ostlund, *Modern quantum chemistry : introduction to advanced electronic structure theory*. Dover Publications, 1996.

[65] B. Roos, "A new method for large-scale Cl calculations," *Chemical Physics Letters*, vol. 15, pp. 153–159, aug 1972.

[66] J. L. Heully, I. Lindgren, E. Lindroth, S. Lundqvist, and A. M. Martensson-Pendrill, "Diagonalisation of the Dirac Hamiltonian as a basis for a relativistic many-body procedure," *Journal of Physics B: Atomic and Molecular Physics*, vol. 19, pp. 2799–2815, sep 1986.

[67] L. L. Foldy and S. A. Wouthuysen, "On the Dirac Theory of Spin 1/2 Particles and Its Non-Relativistic Limit," *Physical Review*, vol. 78, pp. 29–36, apr 1950.

[68] E. F. Valeev, "Libint: A library for the evaluation of molecular integrals of many-body operators over gaussian functions." http://libint.valeyev.net/, 2019. version 2.7.0-beta.1.

[69] D. Gatteschi and R. Sessoli, "Quantum Tunneling of Magnetization and Related Phenomena in Molecular Materials," *Angewandte Chemie International Edition*, vol. 42, pp. 268–297, jan 2003.

[70] C. Benelli and D. D. Gatteschi, *Introduction to molecular magnetism : from transition metals to lanthanides*. John Wiley & Sons, Ltd, 2016.

[71] P. E. M. Siegbahn, J. Almlöf, A. Heiberg, and B. O. Roos, "The complete active space SCF (CASSCF) method in a NewtonRaphson formulation with application to the HNO molecule," *The Journal of Chemical Physics*, vol. 74, pp. 2384–2396, feb 1981.

[72] R. McWeeny, *Methods of molecular quantum mechanics*. Academic Press, 1992.

[73] C. M. Marian, "Spin-Orbit Coupling in Molecules," in *Reviews in Computational Chemistry*, ch. 3, pp. 99–204, Wiley, 2001.

[74] F. Neese, "Efficient and accurate approximations to the molecular spin-orbit coupling operator and their use in molecular g-tensor calculations," *The Journal of Chemical Physics*, vol. 122, p. 24103, jan 2005.

[75] A. Berning, Marcus Schweizer, Hans-Joa, "Spin-orbit matrix elements for internally contracted multireference configuration interaction wavefunctions," *Molecular Physics*, vol. 98, pp. 1823–1833, nov 2000.

[76] C. M. Marian, "Spin-orbit coupling and intersystem crossing in molecules," *DescriptionWiley Interdisciplinary Reviews: Computational Molecular Science*, vol. 2, pp. 187–203, mar 2012.

[77] A. Van Yperen-De Deyne, E. Pauwels, V. Van Speybroeck, and M. Waroquier, "Accurate spinorbit and spinother-orbit contributions to the g-tensor for transition metal containing systems," *Physical Chemistry Chemical Physics*, vol. 14, p. 10690, jul 2012.

[78] M. Blume and R. E. Watson, "Theory of Spin-Orbit Coupling in Atoms. I. Derivation of the Spin-Orbit Coupling Constant," *Proceedings of the Royal Society A: Mathematical, Physical and Engineering Sciences*, vol. 270, pp. 127–143, oct 1962.

[79] T. Nakajima and K. Hirao, "The DouglasKrollHess Approach," *Chemical Reviews*, vol. 112, pp. 385–402, jan 2012.

[80] M. Reiher and A. Wolf, *Relativistic quantum chemistry: the fundamental theory of molecular science*. Wiley-VCH, 2015.

[81] P. Jensen and P. R. Bunker, *Computational molecular spectroscopy.* Wiley, 2000.

[82] M. Sjøvoll, O. Gropen, and J. Olsen, "A determinantal approach to spin-orbit configuration interaction," *Theoretical Chemistry Accounts: Theory, Computation, and Modeling (Theoretica Chimica Acta)*, vol. 97, pp. 301–312, oct 1997.

[83] S. Itoh, R. Saito, T. Kimura, and S. Yabushita, "Relativistic Effect on Multiplet Terms of Rare Earth Ions," *Journal of the Physical Society of Japan*, vol. 63, pp. 807–813, feb 1994.

[84] G.-J. Chen, C.-Y. Gao, J.-L. Tian, J. Tang, W. Gu, X. Liu, S.-P. Yan, D.-Z. Liao, and P. Cheng, "Coordination-perturbed single-molecule magnet behaviour of mononuclear dysprosium complexes," *Dalton Transactions*, vol. 40, p. 5579, may 2011.

[85] G.-J. Chen, Y.-N. Guo, J.-L. Tian, J. Tang, W. Gu, X. Liu, S.-P. Yan, P. Cheng, and D.-Z. Liao, "Enhancing Anisotropy Barriers of Dysprosium(III) Single-Ion Magnets," *Chemistry - A European Journal*, vol. 18, pp. 2484–2487, feb 2012.

[86] E. M. Fatila, E. E. Hetherington, M. Jennings, A. J. Lough, and K. E. Preuss, "Syntheses and crystal structures of anhydrous Ln(hfac) 3 (monoglyme). Ln = La, Ce, Pr, Sm, Eu, Gd, Tb, Dy, Er, Tm," *Dalton Trans.*, vol. 41, pp. 1352–1362, jan 2012.

[87] N. F. Chilton, S. K. Langley, B. Moubaraki, A. Soncini, S. R. Batten, and K. S. Murray, "Single molecule magnetism in a family of mononuclear β-diketonate lanthanide(iii) complexes: rationalization of magnetic anisotropy in complexes of low symmetry," *Chemical Science*, vol. 4, p. 1719, mar 2013.

[88] Z.-G. Wang, J. Lu, C.-Y. Gao, C. Wang, J.-L. Tian, W. Gu, X. Liu, and S.-P. Yan, "Single-ion magnet behavior of a new mononuclear dysprosium complex," *Inorganic Chemistry Communications*, vol. 27, pp. 127–130, jan 2013.

[89] Y. Bi, Y.-N. Guo, L. Zhao, Y. Guo, S.-Y. Lin, S.-D. Jiang, J. Tang, B.-W. Wang, and S. Gao, "Capping Ligand Perturbed Slow Magnetic Relaxation in Dysprosium Single-Ion Magnets," *Chemistry - A European Journal*, vol. 17, pp. 12476–12481, oct 2011.

[90] B. O. Roos, R. Lindh, P.-Å. Malmqvist, V. Veryazov, P.-O. Widmark, and A. C. Borin, "New Relativistic Atomic Natural Orbital Basis Sets for Lanthanide Atoms with Applications to the Ce Diatom and LuF 3," *The Journal of Physical Chemistry A*, vol. 112, pp. 11431–11435, nov 2008.

[91] H. Bolvin, "An Alternative Approach to the g-Matrix: Theory and Applications," *ChemPhysChem*, vol. 7, pp. 1575–1589, jul 2006.

[92] J. J. Baldoví, Y. Duan, R. Morales, A. Gaita-Ariño, E. Ruiz, and E. Coronado, "Rational Design of Lanthanoid Single-Ion Magnets: Predictive Power of the Theoretical Models," *Chemistry - A European Journal*, vol. 22, pp. 13532–13539, sep 2016.

[93] W. Martin, R. Zalubas, and L. Hagan, *Atomic energy levels - the rare-earth elements.* National bureau of standards technical report, 1978.

[94] A. Soncini and L. F. Chibotaru, "Toroidal magnetic states in molecular wheels: Interplay between isotropic exchange interactions and local magnetic anisotropy," *Physical Review B*, vol. 77, p. 220406, jun 2008.

[95] L. Chibotaru, L. Ungur, and A. Soncini, "The Origin of Nonmagnetic Kramers Doublets in the Ground State of Dysprosium Triangles: Evidence for a Toroidal Magnetic Moment," *Angewandte Chemie*, vol. 120, pp. 4194–4197, may 2008.

[96] J. Luzon, K. Bernot, I. J. Hewitt, C. E. Anson, A. K. Powell, and R. Sessoli, "Spin Chirality in a Molecular Dysprosium Triangle: The Archetype of the Noncollinear Ising Model," *Physical Review Letters*, vol. 100, p. 247205, jun 2008.

[97] M. Trif, F. Troiani, D. Stepanenko, and D. Loss, "Spin-Electric Coupling in Molecular Magnets," *Physical Review Letters*, vol. 101, p. 217201, nov 2008.

[98] A. Soncini and L. F. Chibotaru, "Molecular spintronics using noncollinear magnetic molecules," *Physical Review B*, vol. 81, p. 132403, apr 2010.

[99] H. Katsura, N. Nagaosa, and A. V. Balatsky, "Spin Current and Magnetoelectric Effect in Noncollinear Magnets," *Physical Review Letters*, vol. 95, p. 057205, jul 2005.

[100] N. A. Spaldin, M. Fiebig, and M. Mostovoy, "The toroidal moment in condensed-matter physics and its relation to the magnetoelectric effect," *Journal of Physics: Condensed Matter*, vol. 20, p. 434203, oct 2008.

[101] J. Tang, I. Hewitt, N. T. Madhu, G. Chastanet, W. Wernsdorfer, C. E. Anson, C. Benelli, R. Sessoli, and A. K. Powell, "Dysprosium Triangles Showing Single-Molecule Magnet Behavior of Thermally Excited Spin States," *Angewandte Chemie International Edition*, vol. 45, pp. 1729–1733, mar 2006.

[102] F. Faglioni, A. Ligabue, S. Pelloni, A. Soncini, and P. Lazzeretti, "Molecular response to a time-independent non-uniform magnetic-field," *Chemical Physics*, vol. 304, p. 289, oct 2004.

[103] J. M. Crabtree and A. Soncini, "Toroidal quantum states in molecular spin-frustrated triangular nanomagnets with weak spin-orbit coupling: Applications to molecular spintronics," *Physical Review B*, vol. 98, p. 094417, sep 2018.

[104] S. V. Rao, J. M. Ashtree, and A. Soncini, "Toroidal moment in a family of spin-frustrated heterometallic triangular nanomagnets without spin-orbit coupling: Applications in a molecular spintronics device," *Physica B*, vol. Submitted, 2020.

[105] L. Ungur, W. Van den Heuvel, and L. F. Chibotaru, "Ab initio investigation of the non-collinear magnetic structure and the lowest magnetic excitations in dysprosium triangles," *New Journal of Chemistry*, vol. 33, p. 1224, jun 2009.

[106] S.-Y. Lin, W. Wernsdorfer, L. Ungur, A. K. Powell, Y.-N. Guo, J. Tang, L. Zhao, L. F. Chibotaru, and H.-J. Zhang, "Coupling Dy 3 Triangles to Maximize the Toroidal Moment," *Angewandte Chemie*, vol. 124, pp. 12939–12943, dec 2012.

[107] M. Gysler, F. El Hallak, L. Ungur, R. Marx, M. Hakl, P. Neugebauer, Y. Rechkemmer, Y. Lan, I. Sheikin, M. Orlita, C. E. Anson, A. K. Powell, R. Sessoli, L. F. Chibotaru, and J. van Slageren,

"Multitechnique investigation of Dy 3 implications for coupled lanthanide clusters," *Chemical Science*, vol. 7, pp. 4347–4354, jun 2016.

[108] I. Hewitt, J. Tang, N. Madhu, C. Anson, Y. Lan, J. Luzon, M. Etienne, R. Sessoli, and A. Powell, "Coupling Dy3 Triangles Enhances Their Slow Magnetic Relaxation," *Angewandte Chemie International Edition*, vol. 49, pp. 6352–6356, aug 2010.

[109] G. Novitchi, G. Pilet, L. Ungur, V. V. Moshchalkov, W. Wernsdorfer, L. F. Chibotaru, D. Luneau, and A. K. Powell, "Heterometallic CuII/DyIII 1D chiral polymers: chirogenesis and exchange coupling of toroidal moments in trinuclear Dy3 single molecule magnets," *Chemical Science*, vol. 3, p. 1169, mar 2012.

[110] D. Schray, G. Abbas, Y. Lan, V. Mereacre, A. Sundt, J. Dreiser, O. Waldmann, G. Kostakis, C. Anson, and A. Powell, "Combined Magnetic Susceptibility Measurements and 57 Fe Mössbauer Spectroscopy on a Ferromagnetic {Fe III 4 Dy 4 } Ring," *Angewandte Chemie International Edition*, vol. 49, pp. 5185–5188, jul 2010.

[111] K. R. Vignesh, S. K. Langley, K. S. Murray, and G. Rajaraman, "Exploring the Influence of Diamagnetic Ions on the Mechanism of Magnetization Relaxation in {Co III 2 Ln III 2 } (Ln = Dy, Tb, Ho) Butterfly Complexes," *Inorganic Chemistry*, vol. 56, pp. 2518–2532, mar 2017.

[112] M. Li, Y. Lan, A. M. Ako, W. Wernsdorfer, C. E. Anson, G. Buth, A. K. Powell, Z. Wang, and S. Gao, "A Family of 3d-4f Octa-Nuclear [Mn III 4 Ln III 4] Wheels (Ln = Sm, Gd, Tb, Dy, Ho, Er, and Y): Synthesis, Structure, and Magnetism," *Inorganic Chemistry*, vol. 49, pp. 11587–11594, dec 2010.

[113] C. Das, S. Vaidya, T. Gupta, J. M. Frost, M. Righi, E. K. Brechin, M. Affronte, G. Rajaraman, and M. Shanmugam, "Single-Molecule Magnetism, Enhanced Magnetocaloric Effect, and Toroidal Magnetic Moments in a Family of Ln 4 Squares," *Chemistry - A European Journal*, vol. 21, pp. 15639–15650, oct 2015.

[114] P.-H. Guo, J.-L. Liu, Z.-M. Zhang, L. Ungur, L. F. Chibotaru, J.-D. Leng, F.-S. Guo, and M.-L. Tong, "The First {Dy 4 } Single-Molecule Magnet with a Toroidal Magnetic Moment in the Ground State," *Inorganic Chemistry*, vol. 51, pp. 1233–1235, feb 2012.

[115] A. I. Popov, D. I. Plokhov, and A. K. Zvezdin, "Magnetoelectricity of single molecular toroics: The Dy 4 ring cluster," *Physical Review B*, vol. 94, p. 184408, nov 2016.

[116] N. F. Chilton, S. K. Langley, B. Moubaraki, and K. S. Murray, "Synthesis, structural and magnetic studies of an isostructural family of mixed 3d/4f tetranuclear star' clusters," *Chemical Communications*, vol. 46, p. 7787, oct 2010.

[117] S. K. Langley, N. F. Chilton, L. Ungur, B. Moubaraki, L. F. Chibotaru, and K. S. Murray, "Heterometallic Tetranuclear [Ln III 2 Co III 2] Complexes Including Suppression of Quantum Tunneling of Magnetization in the [Dy III 2 Co III 2] Single Molecule Magn," *Inorganic Chemistry*, vol. 51, pp. 11873–11881, nov 2012.

[118] K. R. Vignesh, S. K. Langley, B. Moubaraki, K. S. Murray, and G. Rajaraman, "Large Hexadecametallic {Mn III -Ln III } Wheels: Synthesis, Structural, Magnetic, and Theoretical Characterization," *Chemistry - A European Journal*, vol. 21, pp. 16364–16369, nov 2015.

[119] M. F. Islam, J. F. Nossa, C. M. Canali, and M. Pederson, "First-principles study of spin-electric coupling in a { Cu 3 } single molecular magnet," *Physical Review B*, vol. 82, p. 155446, oct 2010.

[120] J. F. Nossa, M. F. Islam, C. M. Canali, and M. R. Pederson, "First-principles studies of spin-orbit and Dzyaloshinskii-Moriya interactions in the {Cu 3 } single-molecule magnet," *Physical Review B*, vol. 85, p. 085427, feb 2012.

[121] L. Ungur, S.-Y. Lin, J. Tang, and L. F. Chibotaru, "Single-molecule toroics in Ising-type lanthanide molecular clusters," *Chem. Soc. Rev.*, vol. 43, pp. 6894–6905, sep 2014.

[122] K.-Y. Choi, Z. Wang, H. Nojiri, J. van Tol, P. Kumar, P. Lemmens, B. S. Bassil, U. Kortz, and N. S. Dalal, "Coherent Manipulation of Electron Spins in the { Cu 3 } Spin Triangle Complex Impregnated in Nanoporous Silicon," *Physical Review Letters*, vol. 108, p. 067206, feb 2012.

[123] S. Bertaina, S. Gambarelli, T. Mitra, B. Tsukerblat, A. Müller, B. Barbara, and S. Bertaina, "-," *Nature (London)*, vol. 453, p. 203, 2008.

[124] G. Christou, D. Gatteschi, D. N. Hendrickson, and R. Sessoli, "Single-Molecule Magnets," *MRS Bulletin*, vol. 25, pp. 66–71, nov 2000.

[125] D. Gatteschi, "Molecular Magnetism: A basis for new materials," *Advanced Materials*, vol. 6, pp. 635–645, sep 1994.

[126] P. Gütlich and H. A. Goodwin, *Spin CrossoverAn Overall Perspective*. Springer, Berlin, Heidelberg, 2004.

[127] D. I. Plokhov, A. I. Popov, and A. K. Zvezdin, "Quantum magnetoelectric effect in the molecular crystal Dy 3," *Physical Review B*, vol. 84, p. 224436, dec 2011.

[128] D. I. Plokhov, A. K. Zvezdin, and A. I. Popov, "Macroscopic quantum dynamics of toroidal moment in Ising-type rare-earth clusters," *Physical Review B*, vol. 83, p. 184415, may 2011.

[129] R. Winpenny, "Quantum Information Processing Using Molecular Nanomagnets As Qubits," *Angewandte Chemie International Edition*, vol. 47, pp. 7992–7994, oct 2008.

[130] A. S. Zyazin, H. S. van der Zant, M. R. Wegewijs, and A. Cornia, "High-spin and magnetic anisotropy signatures in three-terminal transport through a single molecule," *Synthetic Metals*, vol. 161, pp. 591–597, apr 2011.

[131] A. Candini, S. Klyatskaya, M. Ruben, W. Wernsdorfer, and M. Affronte, "Graphene Spintronic Devices with Molecular Nanomagnets," *Nano Letters*, vol. 11, pp. 2634–2639, jul 2011.

[132] M. Urdampilleta, S. Klyatskaya, J.-P. Cleuziou, M. Ruben, and W. Wernsdorfer, "Supramolecular spin valves," *Nature Materials*, vol. 10, pp. 502–506, jul 2011.

[133] S. Thiele, F. Balestro, R. Ballou, S. Klyatskaya, M. Ruben, and W. Wernsdorfer, "Electrically driven nuclear spin resonance in single-molecule magnets.," *Science (New York, N.Y.)*, vol. 344, pp. 1135–8, jun 2014.

[134] S. Lumetti, A. Candini, C. Godfrin, F. Balestro, W. Wernsdorfer, S. Klyatskaya, M. Ruben, and M. Affronte, "Single-molecule devices with graphene electrodes," *Dalton Transactions*, vol. 45, pp. 16570–16574, oct 2016.

[135] K. Hymas and A. Soncini, "Molecular spintronics using single-molecule magnets under irradiation," *Physical Review B*, vol. 99, no. 24, p. 245404, 2019.

[136] C. Lampropoulos, T. C. Stamatatos, K. A. Abboud, and G. Christou, "Initial use of dioximate ligands in 3d/4f cluster chemistry: Synthesis, structure, and magnetic studies of an unusual [gdiii2mnivo] 8+ complex," *Inorganic chemistry*, vol. 48, no. 2, pp. 429–431, 2009.

[137] S. Mukherjee, M. R. Daniels, R. Bagai, K. A. Abboud, G. Christou, and C. Lampropoulos, "A variety of new tri-and tetranuclear mn–ln and fe–ln (ln= lanthanide) complexes," *Polyhedron*, vol. 29, no. 1, pp. 54–65, 2010.

[138] N. Singh, S. D. Gupta, R. J. Butcher, and G. Christou, "Synthesis and magnetochemistry of heterometallic triangular fe iii2 ln iii (ln= la, gd, tb, dy, and ho) and fe iii2 y iii complexes," *Dalton Transactions*, vol. 46, no. 24, pp. 7897–7903, 2017.

[139] S. Carretta, G. Amoretti, P. Santini, V. Mougel, M. Mazzanti, S. Gambarelli, E. Colineau, and R. Caciuffo, "Magnetic properties and chiral states of a trimetallic uranium complex," *Journal of Physics: Condensed Matter*, vol. 25, p. 486001, dec 2013.

[140] F. Delgado, J. J. Palacios, and J. Fernández-Rossier, "Spin-Transfer Torque on a Single Magnetic Adatom," *Physical Review Letters*, vol. 104, p. 026601, jan 2010.

[141] G.-H. Kim and T.-S. Kim, "Electronic Transport in Single-Molecule Magnets on Metallic Surfaces," *Physical Review Letters*, vol. 92, p. 137203, apr 2004.

[142] M. Misiorny and J. Barnas, "Switching of molecular magnets," *physica status solidi (b)*, vol. 246, pp. 695–715, apr 2009.

[143] F. Elste and C. Timm, "Theory for transport through a single magnetic molecule: Endohedral N @ C 60," *Physical Review B*, vol. 71, p. 155403, apr 2005.

[144] G. González and M. N. Leuenberger, "Berry-Phase Blockade in Single-Molecule Magnets," *Physical Review Letters*, vol. 98, p. 256804, jun 2007.

[145] A. Soncini, T. Mallah, and L. F. Chibotaru, "Molecular Spintronics in Mixed-Valence Magnetic Dimers: The Double-Exchange Blockade Mechanism," *Journal of the American Chemical Society*, vol. 132, pp. 8106–8114, jun 2010.

[146] C. Godfrin, S. Thiele, A. Ferhat, S. Klyatskaya, M. Ruben, W. Wernsdorfer, and F. Balestro, "Electrical read-out of a single spin using an exchange-coupled quantum dot," *ACS nano*, vol. 11, no. 4, pp. 3984–3989, 2017.

[147] B. Georgeot and F. Mila, "Chirality of Triangular Antiferromagnetic Clusters as a Qubit," *Physical Review Letters*, vol. 104, p. 200502, may 2010.

[148] A. Baniodeh, N. Magnani, Y. Lan, G. Buth, C. E. Anson, J. Richter, M. Affronte, J. Schnack, and A. K. Powell, "High spin cycles: topping the spin record for a single molecule verging on quantum criticality," *Nature Partner Journal: Quantum Mater.*, vol. 3, p. 10, dec 2018.

Appendix A

Supplementary Information for Chapter 3

Table A.1: Lowest energy levels in cm^{-1} for Eu^{3+} atom, estimated using different approximations to spin-orbit coupling Hamiltonian (Note: Here the lowest multiplet is a singlet hence for even the first excited state, the gap with the next multiplet must be computed and hence the $\mathcal{H}_{\mathrm{SO}}^{(1)}$ has a high error rate). Computation at CAHF/CASCI-SO level on ANO-RCC basis set, with the contraction [8s7p5d3f2g1h]. Experimental values from: W.C. Martin, R.Zalubas, and L. Hagan, *Atomic energy levels - the rare-earth elements*, Tech. Rep. (National Bureau of Standards, Gaithersburg, MD, 1978).

		$\mathcal{H}_{\mathrm{SO}}^{(1)}$	$\mathcal{H}_{\mathrm{SO}}^{\mathrm{MF}}$	$\mathcal{H}_{\mathrm{SO}}^{\mathrm{BP}}$	EXP.
1	$^7F_0$	0	0	0	0
2	$^7F_1$	1529	382	369	370
3	$^7F_2$	3582	1067	1028	1040
4	$^7F_3$	5765	1967	1889	1890
5	$^7F_4$	7922	3010	2880	2860
6	$^7F_5$	9968	4145	3949	3910
7	$^7F_6$	11813	5334	5056	4940

Table A.2: Lowest energy levels in cm^{-1} for Pr-acac$_3$-$(H_2O)_2$, estimated using different approximations to spin-orbit coupling Hamiltonian. Computation at CAHF/CASCI-SO level on ANO-RCC basis set, with the contraction [8s7p5d3f2g1h] for Ln atoms, [4s3p2d1f] for O, [3s2p] for C and N, [2s] for H.

		$\mathcal{H}_{SO}^{(1)}$	$\mathcal{H}_{SO}^{MF}$	$\mathcal{H}_{SO}^{AMF}$	$\mathcal{H}_{SO}^{ABP}$	$\mathcal{H}_{SO}^{BP}$
1	$^3H_4$	0.000	0.000	0.000	0.000	0.000
2		30.044	35.422	35.337	35.144	35.228
3		245.415	257.721	258.120	258.042	257.645
4		323.248	335.834	336.136	335.976	335.677
5		351.058	372.879	373.300	372.979	372.561
6		432.155	454.142	454.707	454.443	453.868
7		463.804	479.552	480.057	479.947	479.445
8		554.146	572.214	573.088	572.854	571.979
9		560.293	578.304	579.185	578.930	578.044
10	$^3H_5$	5100.211	2268.720	2269.091	2261.752	2261.384
11		5101.345	2272.403	2272.775	2265.458	2265.087
12		5313.022	2490.227	2490.486	2483.208	2482.955
13		5342.852	2515.782	2516.078	2508.754	2508.467
14		5404.147	2576.737	2576.882	2569.604	2569.465
15		5447.364	2618.922	2619.038	2611.744	2611.629
16		5477.411	2649.229	2649.455	2642.120	2641.904
17		5529.861	2696.860	2696.933	2689.586	2689.510
18		5536.870	2713.352	2713.432	2706.145	2706.066
19		5631.764	2796.512	2796.416	2789.012	2789.110
20		5639.174	2803.905	2803.813	2796.425	2796.518

Table A.3: Lowest energy levels in cm^{-1} for Nd-$acac_3$-$(H_2O)_2$, estimated using different approximations to spin-orbit coupling Hamiltonian. Computation at CAHF/CASCI-SO level on ANO-RCC basis set, with the contraction [8s7p5d3f2g1h] for Ln atoms, [4s3p2d1f] for O, [3s2p] for C and N, [2s] for H.

		$\mathcal{H}_{SO}^{(1)}$	$\mathcal{H}_{SO}^{MF}$	$\mathcal{H}_{SO}^{AMF}$	$\mathcal{H}_{SO}^{ABP}$	$\mathcal{H}_{SO}^{BP}$
1	$^4I_{9/2}$	0.000	0.000	0.000	0.000	0.000
2		119.087	123.800	124.312	124.328	123.791
3		183.426	199.307	199.927	199.896	199.263
4		240.237	257.802	258.261	258.306	257.816
5		293.518	313.924	314.829	314.815	313.880
6	$^4I_{11/2}$	4537.869	1996.989	1997.329	1968.895	1968.565
7		4618.762	2079.781	2080.100	2051.724	2051.389
8		4670.952	2131.587	2131.841	2103.463	2103.198
9		4691.019	2151.582	2151.831	2123.401	2123.149
10		4710.870	2172.357	2172.616	2144.278	2144.002
11		4770.697	2232.022	2232.165	2203.795	2203.635

Table A.4: Lowest energy levels in cm^{-1} for Sm-$acac_3$-$(H_2O)_2$, estimated using different approximations to spin-orbit coupling Hamiltonian. Computation at CAHF/CASCI-SO level on ANO-RCC basis set, with the contraction [8s7p5d3f2g1h] for Ln atoms, [4s3p2d1f] for O, [3s2p] for C and N, [2s] for H.

		$\mathcal{H}_{\mathrm{SO}}^{(1)}$	$\mathcal{H}_{\mathrm{SO}}^{\mathrm{MF}}$	$\mathcal{H}_{\mathrm{SO}}^{\mathrm{AMF}}$	$\mathcal{H}_{\mathrm{SO}}^{\mathrm{ABP}}$	$\mathcal{H}_{\mathrm{SO}}^{\mathrm{BP}}$
1	$^6H_{5/2}$	0.000	0.000	0.000	0.000	0.000
2		177.622	177.085	176.653	177.167	177.607
3		305.772	312.792	312.168	312.320	312.954
4	$^6H_{7/2}$	2711.292	1089.569	1089.078	1049.252	1049.762
5		2851.411	1225.692	1225.172	1185.704	1186.243
6		2912.850	1289.108	1288.577	1249.163	1249.715
7		2994.362	1368.264	1367.810	1328.289	1328.763

Table A.5: Lowest energy levels in cm^{-1} for Eu-acac$_3$-$(H_2O)_2$, estimated using different approximations to spin-orbit coupling Hamiltonian. Computation at CAHF/CASCI-SO level on ANO-RCC basis set, with the contraction [8s7p5d3f2g1h] for Ln atoms, [4s3p2d1f] for O, [3s2p] for C and N, [2s] for H.

		$\mathcal{H}_{SO}^{(1)}$	$\mathcal{H}_{SO}^{MF}$	$\mathcal{H}_{SO}^{AMF}$	$\mathcal{H}_{SO}^{ABP}$	$\mathcal{H}_{SO}^{BP}$
1	$^7F_0$	0.000	0.000	0.000	0.000	0.000
2	$^7F_1$	1373.933	246.339	246.501	234.193	234.032
3		1518.521	401.216	401.186	388.828	388.870
4		1625.032	521.864	521.534	509.521	509.846
5	$^7F_2$	3406.539	961.186	961.265	924.811	924.737
6		3454.265	983.695	983.817	945.829	945.719
7		3556.923	1096.882	1096.698	1058.859	1059.060
8		3604.152	1152.722	1152.520	1115.540	1115.747
9		3638.359	1186.961	1186.467	1149.357	1149.852
10	$^7F_3$	5648.331	1924.055	1924.354	1848.650	1848.379
11		5660.111	1936.855	1937.045	1861.213	1861.088
12		5662.126	1938.488	1938.100	1862.530	1862.905
13		5687.503	1971.047	1970.584	1894.931	1895.409
14		5698.096	1989.560	1989.385	1915.053	1915.229
15		5738.170	2022.017	2021.579	1946.689	1947.123
16		5759.521	2038.474	2038.099	1962.630	1963.021
17	$^7F_4$	7698.420	2878.274	2878.084	2751.521	2751.729
18		7753.565	2928.207	2927.975	2800.857	2801.122
19		7773.922	2945.039	2944.588	2817.105	2817.570
20		7796.118	2966.115	2965.796	2837.764	2838.124
21		7821.712	3012.699	3012.270	2886.686	2887.136

22		7859.958	3039.070	3038.822	2912.385	2912.643
23		7884.314	3066.512	3066.143	2939.921	2940.305
24		7936.953	3116.137	3116.228	2989.366	2989.306
25		7951.923	3131.608	3131.621	3004.739	3004.753
26	$^7F_5$	9727.458	3991.868	3990.845	3797.194	3798.258
27		9731.709	3996.273	3995.287	3801.704	3802.730
28		9770.927	4039.874	4039.547	3846.778	3847.155
29		9781.244	4049.099	4048.848	3855.829	3856.132
30		9840.859	4126.938	4126.616	3935.898	3936.234
31		9856.045	4136.070	4135.768	3944.368	3944.688
32		9891.138	4174.527	4174.319	3983.094	3983.306
33		9902.187	4182.124	4182.195	3990.774	3990.727
34		9930.034	4210.433	4210.372	4018.753	4018.831
35		10018.426	4296.588	4296.775	4104.697	4104.565
36		10022.203	4300.427	4300.618	4108.492	4108.354
37	$^7F_6$	11422.275	5034.872	5033.739	4762.134	4763.308
38		11422.362	5034.987	5033.853	4762.257	4763.430
39		11621.991	5250.835	5250.075	4979.670	4980.461
40		11622.858	5251.765	5251.012	4980.614	4981.397
41		11704.953	5329.951	5329.414	5057.497	5058.056
42		11709.872	5336.197	5335.765	5064.059	5064.518
43		11741.869	5367.412	5367.038	5094.764	5095.158
44		11767.201	5394.999	5394.914	5122.833	5122.960
45		11773.721	5401.445	5401.334	5129.101	5129.252
46		11812.475	5438.815	5438.578	5165.739	5166.027
47		11812.652	5439.041	5438.795	5165.955	5166.253

48	11880.090	5506.517	5507.583	5234.450	5233.441
49	11880.162	5506.587	5507.653	5234.517	5233.508

Table A.6: Lowest energy levels in cm^{-1} for Gd-$acac_3$-$(H_2O)_2$, estimated using different approximations to spin-orbit coupling Hamiltonian. Computation at CAHF/CASCI-SO level on ANO-RCC basis set, with the contraction [8s7p5d3f2g1h] for Ln atoms, [4s3p2d1f] for O, [3s2p] for C and N, [2s] for H.

		$\mathcal{H}_{\mathrm{SO}}^{(1)}$	$\mathcal{H}_{\mathrm{SO}}^{\mathrm{MF}}$	$\mathcal{H}_{\mathrm{SO}}^{\mathrm{AMF}}$	$\mathcal{H}_{\mathrm{SO}}^{\mathrm{ABP}}$	$\mathcal{H}_{\mathrm{SO}}^{\mathrm{BP}}$
1	$^8H_{7/2}$	0.000	0.000	0.000	0.000	0.000
2		1.198	0.256	0.240	0.240	0.256
3		2.329	0.534	0.466	0.465	0.534
4		4.320	0.978	0.820	0.820	0.978
5	$^6P_{7/2}$	35631.422	38754.739	38755.034	38742.438	38742.153
6		35687.191	38791.917	38792.152	38779.474	38779.248
7		35728.649	38819.803	38819.965	38807.179	38807.027
8		35822.180	38862.123	38862.141	38849.166	38849.156

Table A.7: Lowest energy levels in cm^{-1} for Tb-$acac_3$-$(H_2O)_2$, estimated using different approximations to spin-orbit coupling Hamiltonian. Computation at CAHF/CASCI-SO level on ANO-RCC basis set, with the contraction [8s7p5d3f2g1h] for Ln atoms, [4s3p2d1f] for O, [3s2p] for C and N, [2s] for H.

		$\mathcal{H}_{SO}^{(1)}$	$\mathcal{H}_{SO}^{MF}$	$\mathcal{H}_{SO}^{AMF}$	$\mathcal{H}_{SO}^{ABP}$	$\mathcal{H}_{SO}^{BP}$
1	$^7F_6$	0.000	0.000	0.000	0.000	0.000
2		0.086	0.088	0.088	0.089	0.089
3		109.166	110.230	110.745	110.994	110.466
4		109.498	110.721	111.240	111.488	110.955
5		178.742	175.074	175.694	176.244	175.607
6		181.252	177.079	177.679	178.232	177.615
7		251.493	249.227	249.974	250.728	249.955
8		274.771	270.802	271.533	272.333	271.578
9		302.233	301.949	302.774	303.449	302.595
10		382.280	372.479	373.349	374.708	373.811
11		385.096	376.714	377.600	378.854	377.941
12		598.843	609.223	610.352	611.159	610.007
13		598.918	609.364	610.494	611.296	610.143
14	$^7F_5$	4578.634	2134.613	2134.871	2221.242	2220.953
15		4581.181	2137.687	2137.938	2224.307	2224.024
16		4709.263	2264.358	2264.789	2351.952	2351.479
17		4729.411	2285.391	2285.791	2372.912	2372.478
18		4754.032	2306.305	2306.825	2394.257	2393.687
19		4790.102	2342.268	2342.862	2430.763	2430.125
20		4800.710	2358.785	2359.322	2446.743	2446.169
21		4841.647	2413.206	2413.719	2500.278	2499.730

22	4843.614	2415.628	2416.174	2502.618	2502.035
23	4936.468	2506.351	2507.343	2593.697	2592.669
24	4941.254	2511.618	2512.609	2598.894	2597.867

Table A.8: Lowest energy levels in cm^{-1} for Dy-$acac_3$-$(H_2O)_2$, estimated using different approximations to spin-orbit coupling Hamiltonian. Computation at CAHF/CASCI-SO level on ANO-RCC basis set, with the contraction [8s7p5d3f2g1h] for Ln atoms, [4s3p2d1f] for O, [3s2p] for C and N, [2s] for H.

		$\mathcal{H}_{SO}^{(1)}$	$\mathcal{H}_{SO}^{MF}$	$\mathcal{H}_{SO}^{AMF}$	$\mathcal{H}_{SO}^{ABP}$	$\mathcal{H}_{SO}^{BP}$
1	$^6H_{15/2}$	0.000	0.000	0.000	0.000	0.000
2		150.012	155.631	155.926	156.224	155.919
3		227.942	233.726	234.178	234.441	233.973
4		279.416	287.084	287.655	287.940	287.350
5		308.225	316.519	317.365	317.671	316.802
6		392.191	408.291	409.277	409.614	408.606
7		441.406	462.929	463.280	463.546	463.192
8		504.802	527.901	529.371	529.712	528.218
9	$^6H_{13/2}$	7590.741	3604.472	3604.306	3720.021	3720.180
10		7667.916	3681.367	3681.459	3797.518	3797.394
11		7744.439	3760.008	3760.295	3876.349	3876.011
12		7789.661	3806.445	3806.795	3922.803	3922.396
13		7833.079	3853.451	3853.829	3969.690	3969.251
14		7868.779	3891.231	3891.794	4007.600	4006.987
15		7927.175	3949.623	3950.773	4066.627	4065.433

Table A.9: Lowest energy levels in cm^{-1} for Dy-acac3-dppz, estimated using different approximations to spin-orbit coupling Hamiltonian. Computation at CAHF/CASCI-SO level on ANO-RCC basis set, with the contraction [8s7p5d3f2g1h] for Ln atoms, [4s3p2d1f] for O, [3s2p] for C and N, [2s] for H.

		$\mathcal{H}_{SO}^{(1)}$	$\mathcal{H}_{SO}^{MF}$	$\mathcal{H}_{SO}^{AMF}$	$\mathcal{H}_{SO}^{ABP}$	$\mathcal{H}_{SO}^{BP}$
1	$^6H_{15/2}$	0.000	0.000	0.000	0.000	0.000
2		140.260	146.058	146.238	146.525	146.334
3		216.017	220.812	221.069	221.339	221.062
4		252.616	258.739	258.929	259.182	258.961
5		284.484	294.399	294.613	294.884	294.643
6		331.070	347.807	347.545	347.798	348.046
7		389.570	407.767	408.196	408.522	408.059
8		482.724	507.087	507.844	508.170	507.399
9	$^6H_{13/2}$	7578.824	3593.847	3593.496	3709.120	3709.457
10		7662.257	3676.720	3676.694	3792.632	3792.626
11		7735.159	3752.413	3752.448	3868.375	3868.289
12		7763.013	3782.877	3782.624	3898.441	3898.637
13		7799.203	3817.762	3817.716	3933.601	3933.597
14		7820.567	3842.565	3842.681	3958.441	3958.256
15		7864.291	3889.519	3889.862	4005.493	4005.088

Table A.10: Lowest energy levels in cm^{-1} for Dy-acac3-dpq, estimated using different approximations to spin-orbit coupling Hamiltonian. Computation at CAHF/CASCI-SO level on ANO-RCC basis set, with the contraction [8s7p5d3f2g1h] for Ln atoms, [4s3p2d1f] for O, [3s2p] for C and N, [2s] for H.

		$\mathcal{H}_{SO}^{(1)}$	$\mathcal{H}_{SO}^{MF}$	$\mathcal{H}_{SO}^{AMF}$	$\mathcal{H}_{SO}^{ABP}$	$\mathcal{H}_{SO}^{BP}$
1	$^6H_{15/2}$	0.000	0.000	0.000	0.000	0.000
2		115.823	121.063	121.091	121.300	121.265
3		183.165	188.351	188.291	188.503	188.549
4		219.752	225.325	225.250	225.483	225.539
5		259.673	267.290	267.295	267.586	267.560
6		279.837	291.320	291.175	291.433	291.563
7		385.096	404.242	404.679	404.986	404.516
8		515.146	540.573	540.678	540.984	540.875
9	$^6H_{13/2}$	7561.693	3574.656	3574.412	3690.108	3690.334
10		7647.109	3660.830	3660.653	3776.558	3776.709
11		7698.455	3714.005	3713.662	3829.550	3829.849
12		7725.342	3742.333	3741.930	3857.782	3858.137
13		7771.694	3788.416	3788.278	3904.199	3904.284
14		7812.332	3833.729	3833.726	3949.506	3949.458
15		7893.439	3919.229	3919.106	4034.756	4034.821

Table A.11: Lowest energy levels in cm^{-1} for Dy-acac3-phen, estimated using different approximations to spin-orbit coupling Hamiltonian. Computation at CAHF/CASCI-SO level on ANO-RCC basis set, with the contraction [8s7p5d3f2g1h] for Ln atoms, [4s3p2d1f] for O, [3s2p] for C and N, [2s] for H.

		$\mathcal{H}_{SO}^{(1)}$	$\mathcal{H}_{SO}^{MF}$	$\mathcal{H}_{SO}^{AMF}$	$\mathcal{H}_{SO}^{ABP}$	$\mathcal{H}_{SO}^{BP}$
1	$^6H_{15/2}$	0.000	0.000	0.000	0.000	0.000
2		123.698	129.729	129.951	130.197	129.963
3		193.171	198.917	199.001	199.249	199.149
4		244.202	250.050	250.095	250.340	250.270
5		284.896	292.441	292.697	292.986	292.695
6		320.482	337.056	336.694	336.955	337.298
7		405.817	425.197	425.920	426.274	425.509
8		493.610	517.999	519.016	519.358	518.314
9	$^6H_{13/2}$	7567.171	3581.339	3580.932	3696.600	3696.986
10		7650.893	3664.519	3664.507	3780.435	3780.414
11		7718.129	3734.289	3734.242	3850.170	3850.170
12		7755.668	3774.985	3774.499	3890.331	3890.759
13		7792.445	3811.010	3811.021	3926.910	3926.838
14		7830.099	3852.449	3852.806	3968.569	3968.141
15		7888.933	3912.703	3913.335	4029.106	4028.407

Table A.12: Lowest energy levels in cm^{-1} for Dy-hfac3-glyme, estimated using different approximations to spin-orbit coupling Hamiltonian. Computation at CAHF/CASCI-SO level on ANO-RCC basis set, with the contraction [8s7p5d3f2g1h] for Ln atoms, [4s3p2d1f] for O, [3s2p] for C and N, [2s] for H.

		$\mathcal{H}_{SO}^{(1)}$	$\mathcal{H}_{SO}^{MF}$	$\mathcal{H}_{SO}^{AMF}$	$\mathcal{H}_{SO}^{ABP}$	$\mathcal{H}_{SO}^{BP}$
1	$^6H_{15/2}$	0.000	0.000	0.000	0.000	0.000
2		105.036	108.469	108.605	108.768	108.627
3		156.141	157.833	158.129	158.300	157.993
4		182.523	186.353	186.838	187.023	186.523
5		210.550	218.292	218.160	218.300	218.428
6		239.918	249.820	250.098	250.292	250.000
7		300.513	313.612	314.499	314.743	313.831
8		428.731	450.082	451.792	452.086	450.360
9	$^6H_{13/2}$	7547.744	3558.825	3558.305	3673.997	3674.502
10		7628.518	3639.850	3639.693	3755.570	3755.696
11		7670.593	3684.425	3684.138	3799.947	3800.201
12		7692.455	3705.553	3705.504	3821.370	3821.375
13		7729.002	3742.389	3742.794	3858.691	3858.238
14		7753.931	3769.822	3770.476	3886.304	3885.593
15		7807.296	3827.080	3828.392	3944.047	3942.673

Table A.13: Lowest energy levels in cm^{-1} for Ho-acac$_3$-$(H_2O)_2$, estimated using different approximations to spin-orbit coupling Hamiltonian. Computation at CAHF/CASCI-SO level on ANO-RCC basis set, with the contraction [8s7p5d3f2g1h] for Ln atoms, [4s3p2d1f] for O, [3s2p] for C and N, [2s] for H.

		$\mathcal{H}_{SO}^{(1)}$	$\mathcal{H}_{SO}^{MF}$	$\mathcal{H}_{SO}^{AMF}$	$\mathcal{H}_{SO}^{ABP}$	$\mathcal{H}_{SO}^{BP}$
1	$^5I_8$	0.000	0.000	0.000	0.000	0.000
2		1.919	2.182	2.140	2.147	2.190
3		46.129	50.707	51.257	51.368	50.787
4		52.377	58.020	58.590	58.714	58.117
5		84.145	93.831	94.794	95.001	94.013
6		108.648	122.029	123.069	123.319	122.255
7		129.353	144.360	145.815	146.136	144.645
8		142.483	159.688	160.937	161.270	159.981
9		149.947	167.620	168.593	168.957	167.933
10		165.937	185.877	186.440	186.840	186.228
11		182.349	204.311	205.442	205.871	204.680
12		190.878	212.945	214.624	215.061	213.305
13		197.172	219.965	221.302	221.774	220.362
14		206.744	231.834	232.292	232.771	232.246
15		220.600	247.650	248.364	248.888	248.109
16		251.539	282.228	284.298	284.909	282.779
17		252.224	283.145	285.208	285.821	283.699
18	$^5I_7$	10504.775	5158.213	5158.016	5276.684	5276.792
19		10504.879	5158.382	5158.183	5276.851	5276.962
20		10552.648	5208.799	5209.058	5327.730	5327.393
21		10553.927	5210.656	5210.902	5329.574	5329.249

22	10586.377	5244.056	5244.654	5363.403	5362.728
23	10593.621	5252.806	5253.363	5372.110	5371.482
24	10599.377	5258.857	5259.545	5378.293	5377.520
25	10607.311	5267.616	5268.188	5386.907	5386.256
26	10614.533	5275.319	5276.007	5394.734	5393.974
27	10618.157	5279.770	5279.788	5398.482	5398.405
28	10621.291	5283.129	5283.250	5401.952	5401.773
29	10628.557	5289.912	5291.177	5409.923	5408.578
30	10629.669	5291.149	5292.406	5411.152	5409.817
31	10678.232	5342.224	5344.069	5462.801	5460.893
32	10678.298	5342.304	5344.149	5462.881	5460.973

Table A.14: Lowest energy levels in cm^{-1} for Er-acac$_3$-$(H_2O)_2$, estimated using different approximations to spin-orbit coupling Hamiltonian. Computation at CAHF/CASCI-SO level on ANO-RCC basis set, with the contraction [8s7p5d3f2g1h] for Ln atoms, [4s3p2d1f] for O, [3s2p] for C and N, [2s] for H.

		$\mathcal{H}_{SO}^{(1)}$	$\mathcal{H}_{SO}^{MF}$	$\mathcal{H}_{SO}^{AMF}$	$\mathcal{H}_{SO}^{ABP}$	$\mathcal{H}_{SO}^{BP}$
1	$^4I_{15/2}$	0.000	0.000	0.000	0.000	0.000
2		36.831	37.218	36.034	36.052	37.255
3		74.791	73.151	72.775	72.820	73.200
4		100.935	97.498	96.568	96.576	97.505
5		136.949	137.747	137.332	137.469	137.864
6		184.714	183.265	182.466	182.581	183.347
7		266.129	262.179	260.916	261.015	262.248
8		323.567	316.769	314.869	314.921	316.775
9	$^4I_{13/2}$	12759.303	6612.572	6612.129	6693.212	6693.604
10		12789.242	6642.180	6640.532	6721.613	6723.204
11		12819.419	6671.957	6671.104	6752.167	6752.985
12		12836.205	6688.354	6687.029	6768.101	6769.386
13		12868.241	6720.243	6718.951	6799.999	6801.262
14		12924.615	6775.984	6774.444	6855.483	6856.993
15		12984.987	6834.685	6832.727	6913.722	6915.667

Table A.15: Lowest energy levels in cm^{-1} for Tm-$acac_3$-$(H_2O)_2$, estimated using different approximations to spin-orbit coupling Hamiltonian. Computation at CAHF/CASCI-SO level on ANO-RCC basis set, with the contraction [8s7p5d3f2g1h] for Ln atoms, [4s3p2d1f] for O, [3s2p] for C and N, [2s] for H.

		$\mathcal{H}_{SO}^{(1)}$	$\mathcal{H}_{SO}^{MF}$	$\mathcal{H}_{SO}^{AMF}$	$\mathcal{H}_{SO}^{ABP}$	$\mathcal{H}_{SO}^{BP}$
1	$^3H_6$	0.000	0.000	0.000	0.000	0.000
2		0.710	0.713	0.721	0.721	0.713
3		137.511	139.317	138.485	138.560	139.389
4		141.074	142.578	141.713	141.782	142.644
5		188.034	188.855	187.311	187.372	188.912
6		202.109	202.194	200.521	200.569	202.236
7		253.536	253.171	251.595	251.655	253.222
8		305.557	304.046	302.132	302.179	304.083
9		321.478	320.195	318.348	318.396	320.231
10		427.783	424.983	422.620	422.658	425.008
11		428.420	425.746	423.402	423.440	425.771
12		634.833	632.315	629.472	629.552	632.376
13		634.905	632.398	629.553	629.632	632.459
14	$^3H_5$	6457.523	6900.916	6899.561	6958.324	6959.676
15		6498.903	6944.529	6943.114	7000.986	7002.398
16		6538.608	6976.716	6974.969	7034.027	7035.750
17		6544.062	6991.190	6989.564	7047.778	7049.388
18		6592.535	7032.458	7030.819	7089.153	7090.769
19		6641.845	7100.982	7099.326	7156.263	7157.873
20		6660.412	7121.374	7119.760	7175.855	7177.438
21		6711.782	7149.517	7147.674	7205.678	7207.474

22	6725.750	7173.261	7171.467	7228.504	7230.260
23	15519.004	8360.321	8358.678	8390.166	8391.800
24	15519.434	8361.362	8359.721	8391.226	8392.858

Table A.16: Lowest energy levels in cm^{-1} for Yb-$acac_3$-$(H_2O)_2$, estimated using different approximations to spin-orbit coupling Hamiltonian. Computation at CAHF/CASCI-SO level on ANO-RCC basis set, with the contraction [8s7p5d3f2g1h] for Ln atoms, [4s3p2d1f] for O, [3s2p] for C and N, [2s] for H.

		$\mathcal{H}_{\mathrm{SO}}^{(1)}$	$\mathcal{H}_{\mathrm{SO}}^{\mathrm{MF}}$	$\mathcal{H}_{\mathrm{SO}}^{\mathrm{AMF}}$	$\mathcal{H}_{\mathrm{SO}}^{\mathrm{ABP}}$	$\mathcal{H}_{\mathrm{SO}}^{\mathrm{BP}}$
1	$^2F_{7/2}$	0.000	0.000	0.000	0.000	0.000
2		210.998	208.998	208.662	208.661	208.988
3		253.015	251.256	250.563	250.563	251.250
4		360.947	359.358	358.009	358.010	359.345
5	$^2F_{5/2}$	19085.144	10611.114	10609.584	10581.883	10583.408
6		19259.737	10787.325	10786.045	10758.341	10759.617
7		19372.892	10900.917	10900.108	10872.402	10873.215

Table A.17: Mean μ and standard deviation σ for the %errors affecting the energy gaps within the lowest energy spin-orbit multiplets for Ln-acac$_3$-$(H_2O)_2$ complexes, estimated using different approximations to spin-orbit coupling Hamiltonian with respect to the results obtained by inclusion of the true Breit-Pauli Hamiltonian contribution. Between parenthesis the mean absolute errors (MAE) when different from $|\mu|$. Computations at CAHF/CASCI-SO level on ANO-RCC basis set, with the contraction [8s7p5d3f2g1h] for Ln atoms, [4s3p2d1f] for O, [3s2p] for C, [2s] for H.

			$\mathcal{H}_{\rm SO}^{(1)}$	$\mathcal{H}_{\rm SO}^{\rm MF}$	$\mathcal{H}_{\rm SO}^{\rm AMF}$	$\mathcal{H}_{\rm SO}^{\rm ABP}$
Pr(III)	$^3H_4$	μ	−5.396	0.110	0.192	0.082
		σ	3.888	0.179	0.055	0.132
			–	–	–	(0.141)
	$^3H_5$	μ	110.704	0.286	0.292	0.006
		σ	8.275	0.021	0.027	0.007
			–	–	–	(0.008)
Nd(III)	$^4I_{9/2}$	μ	−6.263	0.009	0.307	0.310
		σ	1.757	0.012	0.103	0.100
			–	(0.012)	–	–
	$^4I_{11/2}$	μ	122.487	1.355	1.367	0.013
		σ	4.852	0.054	0.057	0.003
			–	–	–	–
Sm(III)	$^6H_{5/2}$	μ	−1.143	−0.173	−0.394	−0.225
		σ	1.629	0.171	0.202	0.032
			(1.152)	–	–	–
	$^6H_{7/2}$	μ	139.270	3.311	3.269	−0.043
		σ	14.078	0.352	0.347	0.006
			–	–	–	–

Eu(III)	$^7F_1$	μ	332.099	3.597	3.596	−0.002
		σ	138.924	1.496	1.562	0.067
			–	–	–	(0.048)
	$^7F_2$	μ	241.787	3.614	3.603	−0.012
		σ	23.919	0.357	0.379	0.022
			–	–	–	(0.020)
	$^7F_3$	μ	199.905	3.969	3.959	−0.011
		σ	4.856	0.110	0.121	0.016
			–	–	–	(0.017)
	$^7F_4$	μ	171.805	4.402	4.393	−0.009
		σ	5.272	0.141	0.138	0.006
			–	–	–	(0.010)
	$^7F_5$	μ	150.097	4.874	4.867	−0.008
		σ	4.334	0.153	0.143	0.011
			–	–	–	(0.009)
	$^7F_6$	μ	131.530	5.381	5.375	−0.007
		σ	4.176	0.157	0.146	0.014
			–	–	–	(0.013)

Gd(III)	$^{8}H_{7/2}$	μ	348.856	0.023	−11.697	−11.716
		σ	17.186	0.020	5.138	5.119
			–	–	–	–
	$^{6}P_{7/2}$	μ	−7.932	0.033	0.033	0.000
		σ	0.101	0.000	0.000	0.000
			–	–	–	–
Tb(III)	$^{7}F_{6}$	μ	−0.063	−0.305	−0.076	0.227
		σ	2.040	0.200	0.449	0.299
			(1.693)	–	(0.205)	(0.339)
	$^{7}F_{5}$	μ	97.419	−3.595	−3.573	0.024
		σ	5.425	0.193	0.201	0.009
			–	–	–	–
Dy(III)	$^{6}H_{15/2}$	μ	−3.570	−0.095	0.111	0.211
		σ	0.881	0.043	0.081	0.069
			–	–	–	–
	$^{6}H_{13/2}$	μ	99.011	−2.967	−2.958	0.011
		σ	3.176	0.093	0.102	0.010
			–	–	–	(0.012)
Ho(III)	$^{5}I_{8}$	μ	−10.770	−0.196	0.343	0.562
		σ	0.668	0.055	0.749	0.726
			–	–	(0.627)	(0.807)
	$^{5}I_{7}$	μ	97.141	−2.207	−2.195	0.013
		σ	1.063	0.022	0.033	0.012
			–	–	–	(0.014)
Er(III)	$^{4}I_{15/2}$	μ	1.180	−0.047	−0.971	−0.923
		σ	1.655	0.038	1.034	1.038

			(1.695)	–	–	–
	$^4I_{13/2}$	μ	89.393	−1.194	−1.213	−0.018
		σ	0.996	0.014	0.010	0.007
			–	–	–	–
Tm(III)	$^3H_6$	μ	−0.021	−0.020	−0.484	−0.460
		σ	0.665	0.015	0.512	0.516
			(0.529)	–	(0.667)	(0.649)
	$^3H_5$	μ	9.628	−0.734	−0.757	−0.022
		σ	37.226	0.179	0.180	0.002
			(21.252)	–	–	–
Yb(III)	$^2F_{7/2}$	μ	0.703	0.004	−0.267	−0.267
		σ	0.258	0.001	0.108	0.108
			–	–	–	–
	$^2F_{5/2}$	μ	79.167	0.258	0.247	−0.011
		σ	1.090	0.004	0.001	0.004
			–	–	–	–

Table A.18: Mean μ and standard deviation σ for the %errors affecting the energy gaps within the ground $^6H_{15/2}$ and first excited $^6H_{13/2}$ spin-orbit multiplet for different Dy(III) complexes, estimated using different approximations to spin-orbit coupling Hamiltonian with respect to the results obtained by inclusion of the true Breit-Pauli Hamiltonian contribution. Between parenthesis the mean absolute errors (MAE) when different from $|\mu|$. Computations at CAHF/CASCI-SO level on ANO-RCC basis set, with the contraction [8s7p5d3f2g1h] for Ln atoms, [4s3p2d1f] for O, [3s2p] for C and N, [2s] for H.

			$\mathcal{H}_{\rm SO}^{(1)}$	$\mathcal{H}_{\rm SO}^{\rm MF}$	$\mathcal{H}_{\rm SO}^{\rm AMF}$	$\mathcal{H}_{\rm SO}^{\rm ABP}$
$acac_3$-$(H_2O)_2$	$^6H_{15/2}$	μ	−3.570	−0.095	0.111	0.211
		σ	0.881	0.043	0.081	0.069
			–	–	–	–
	$^6H_{13/2}$	μ	99.011	−2.967	−2.958	0.011
		σ	3.176	0.093	0.102	0.010
			–	–	–	(0.012)
$acac_3$-dppz	$^6H_{15/2}$	μ	−3.800	−0.096	−0.015	0.088
		σ	1.095	0.044	0.074	0.075
			–	–	(0.051)	(0.108)
	$^6H_{13/2}$	μ	99.662	−2.984	−2.985	0.000
		σ	2.733	0.080	0.084	0.006
			–	–	–	(0.004)
$acac_3$-dpq	$^6H_{15/2}$	μ	−3.777	−0.096	−0.091	0.011
		σ	0.964	0.036	0.069	0.053
			–	–	(0.103)	(0.039)
	$^6H_{13/2}$	μ	100.161	−2.999	−3.004	−0.004
		σ	3.052	0.089	0.091	0.004
			–	–	–	(0.005)

$acac_3$-phen	$^6H_{15/2}$	μ	−3.899	−0.097	−0.014	0.091
		σ	1.141	0.041	0.107	0.109
			–	–	(0.081)	(0.120)
	$^6H_{13/2}$	μ	99.780	−2.988	−2.988	0.001
		σ	3.025	0.088	0.096	0.010
			–	–	–	(0.007)
$hfac_3$-glyme	$^6H_{15/2}$	μ	−3.330	−0.086	0.097	0.189
		σ	1.267	0.030	0.149	0.144
			–	–	(0.138)	(0.206)
	$^6H_{13/2}$	μ	101.368	−3.032	−3.027	0.006
		σ	2.422	0.071	0.086	0.017
			–	–	–	(0.013)

Appendix B

Supplementary Information for Chapter 7

B.1 Eigenvectors

B.1.1 Family 1, 3-site, Spin 1/2

$$\hat{\tau_z} = -1, +1, 0, 0$$

$$0.021119|\downarrow\downarrow\uparrow\rangle + 0.696311|\downarrow\uparrow\downarrow\rangle - 0.717430|\uparrow\downarrow\downarrow\rangle$$

$$\Rightarrow Ms = -1/2, S = 1/2$$

$$0.021119|\downarrow\uparrow\uparrow\rangle + 0.696311|\uparrow\downarrow\uparrow\rangle - 0.717430|\uparrow\uparrow\downarrow\rangle$$

$$\Rightarrow Ms = +1/2, S = 1/2$$

$$0.816223|\downarrow\uparrow\uparrow\rangle - 0.426401|\uparrow\downarrow\uparrow\rangle - 0.389822|\uparrow\uparrow\downarrow\rangle$$

$$\Rightarrow Ms = +1/2, S = 1/2$$

$$-0.816223|\downarrow\downarrow\uparrow\rangle + 0.426401|\downarrow\uparrow\downarrow\rangle + 0.389822|\uparrow\downarrow\downarrow\rangle$$

$$\Rightarrow Ms = -1/2, S = 1/2$$

B.1.2 Family 1, 5-site, Spin 1/2

$$\hat{\tau_z} = 0, 0, 0, 0$$

$$-0.191079|\downarrow\downarrow\downarrow\uparrow\uparrow\rangle + 0.219995|\downarrow\downarrow\uparrow\downarrow\uparrow\rangle + 0.055115|\downarrow\downarrow\uparrow\uparrow\downarrow\rangle$$

$$-0.001718|\downarrow\downarrow\uparrow\uparrow\uparrow\rangle + 0.144293|\downarrow\uparrow\downarrow\downarrow\uparrow\rangle - 0.453467|\downarrow\uparrow\downarrow\uparrow\downarrow\rangle$$

$$+0.225143|\downarrow\uparrow\uparrow\downarrow\downarrow\rangle + 0.004499|\downarrow\uparrow\uparrow\downarrow\uparrow\rangle - 0.002780|\downarrow\uparrow\uparrow\uparrow\downarrow\rangle$$

$$-0.173209|\uparrow\downarrow\downarrow\downarrow\uparrow\rangle + 0.589431|\uparrow\downarrow\downarrow\uparrow\downarrow\rangle + 0.001718|\uparrow\downarrow\downarrow\uparrow\uparrow\rangle$$

$$-0.500253|\uparrow\downarrow\uparrow\downarrow\downarrow\rangle - 0.007279|\uparrow\downarrow\uparrow\downarrow\uparrow\rangle + 0.007279|\uparrow\downarrow\uparrow\uparrow\downarrow\rangle$$

$$+0.084031|\uparrow\uparrow\downarrow\downarrow\downarrow\rangle + 0.002780|\uparrow\uparrow\downarrow\downarrow\uparrow\rangle - 0.004499|\uparrow\uparrow\downarrow\uparrow\downarrow\rangle$$

$$\Rightarrow Eigenvector1$$

$$0.534183|\downarrow\downarrow\downarrow\uparrow\uparrow\rangle - 0.028544|\downarrow\downarrow\uparrow\downarrow\uparrow\rangle - 0.580369|\downarrow\downarrow\uparrow\uparrow\downarrow\rangle$$

$$-0.011410|\downarrow\downarrow\uparrow\uparrow\uparrow\rangle + -0.221681|\downarrow\uparrow\downarrow\downarrow\uparrow\rangle - 0.108462|\downarrow\uparrow\downarrow\uparrow\downarrow\rangle$$

$$+0.404873|\downarrow\uparrow\uparrow\downarrow\downarrow\rangle + 0.004358|\downarrow\uparrow\uparrow\downarrow\uparrow\rangle + 0.007052|\downarrow\uparrow\uparrow\uparrow\downarrow\rangle$$

$$-0.283958|\uparrow\downarrow\downarrow\downarrow\uparrow\rangle + 0.154648|\uparrow\downarrow\downarrow\uparrow\downarrow\rangle + 0.011410|\uparrow\downarrow\downarrow\uparrow\uparrow\rangle$$

$$+0.204040|\uparrow\downarrow\uparrow\downarrow\downarrow\rangle + 0.002694|\uparrow\downarrow\uparrow\downarrow\uparrow\rangle - 0.002694|\uparrow\downarrow\uparrow\uparrow\downarrow\rangle$$

$$-0.074730|\uparrow\uparrow\downarrow\downarrow\downarrow\rangle - 0.007052|\uparrow\uparrow\downarrow\downarrow\uparrow\rangle - 0.004358|\uparrow\uparrow\downarrow\uparrow\downarrow\rangle$$

$$\Rightarrow Eigenvector2$$

$$-0.036539|\downarrow\downarrow\downarrow\uparrow\uparrow\rangle - 0.040919|\downarrow\downarrow\uparrow\downarrow\uparrow\rangle - 0.029669|\downarrow\downarrow\uparrow\uparrow\downarrow\rangle$$

$$+0.562903|\downarrow\downarrow\uparrow\uparrow\uparrow\rangle - 0.011332|\downarrow\uparrow\downarrow\downarrow\uparrow\rangle + 0.033915|\downarrow\uparrow\downarrow\uparrow\downarrow\rangle$$

$$+0.084544|\downarrow\uparrow\uparrow\downarrow\downarrow\rangle - 0.141627|\downarrow\uparrow\uparrow\downarrow\uparrow\rangle - 0.540011|\downarrow\uparrow\uparrow\uparrow\downarrow\rangle$$

$$+0.088791|\uparrow\downarrow\downarrow\downarrow\uparrow\rangle + 0.032293|\uparrow\downarrow\downarrow\uparrow\downarrow\rangle - 0.370785|\uparrow\downarrow\downarrow\uparrow\uparrow\rangle$$

$$-0.013957|\uparrow\downarrow\uparrow\downarrow\downarrow\rangle - 0.206266|\uparrow\downarrow\uparrow\downarrow\uparrow\rangle + 0.014148|\uparrow\downarrow\uparrow\uparrow\downarrow\rangle$$

$$-0.107127|\uparrow\uparrow\downarrow\downarrow\downarrow\rangle + 0.037040|\uparrow\uparrow\downarrow\downarrow\uparrow\rangle + 0.215010|\uparrow\uparrow\downarrow\uparrow\downarrow\rangle$$

$$+0.118735|\downarrow\uparrow\downarrow\uparrow\uparrow\rangle + 0.310853|\uparrow\uparrow\uparrow\downarrow\downarrow\rangle$$

$$\Rightarrow Eigenvector3$$

$$-0.022607|\downarrow\downarrow\downarrow\uparrow\uparrow\rangle - 0.025316|\downarrow\downarrow\uparrow\downarrow\uparrow\rangle - 0.018356|\downarrow\downarrow\uparrow\uparrow\downarrow\rangle$$

$$+0.133572|\downarrow\downarrow\uparrow\uparrow\uparrow\rangle - 0.007011|\downarrow\uparrow\downarrow\downarrow\uparrow\rangle + 0.020983|\downarrow\uparrow\downarrow\uparrow\downarrow\rangle$$

$$+0.052307|\downarrow\uparrow\uparrow\downarrow\downarrow\rangle - 0.169629|\downarrow\uparrow\uparrow\downarrow\uparrow\rangle + 0.227970|\downarrow\uparrow\uparrow\uparrow\downarrow\rangle$$

$$+0.054934|\uparrow\downarrow\downarrow\downarrow\uparrow\rangle + 0.019979|\uparrow\downarrow\downarrow\uparrow\downarrow\rangle - 0.444094|\uparrow\downarrow\downarrow\uparrow\uparrow\rangle$$

$$-0.008635|\uparrow\downarrow\uparrow\downarrow\downarrow\rangle + 0.087077|\uparrow\downarrow\uparrow\downarrow\uparrow\rangle + 0.223445|\uparrow\downarrow\uparrow\uparrow\downarrow\rangle$$

$$-0.066279|\uparrow\uparrow\downarrow\downarrow\downarrow\rangle + 0.584988|\uparrow\uparrow\downarrow\downarrow\uparrow\rangle + 0.051020|\uparrow\uparrow\downarrow\uparrow\downarrow\rangle$$

$$-0.191913|\downarrow\uparrow\downarrow\uparrow\uparrow\rangle - 0.502436|\uparrow\uparrow\uparrow\downarrow\downarrow\rangle$$

$$\Rightarrow Eigenvector4$$

B.2 Ground-State Toroidal moments

- Family 1:
  - 3-membered Ring
    - Spin 1/2: τ_Z =(1,-1,0,0)
    - Spin 3/2: τ_Z =(2,-2,0,0)

    - Spin 5/2: τ_Z =(3,-3,0,0)
    - Spin 7/2: τ_Z =(4,-4,0,0)
  - 5-membered Ring
    - Spin 1/2: τ_Z =(0,0,0,0)
    - Spin 3/2: τ_Z =(0,0,0,0)
  - 7-membered Ring
    - Spin 1/2: τ_Z =(0,0,0,0)
    - Spin 3/2: τ_Z =(0,0,0,0)

- Family 2:
  - 5-membered Ring, $1.00 > R_J > 0.25$:

    τ_Z =(1.3333333, -1.3333333, 0, 0)
  - 7-membered Ring, $0.56 > R_J > 0.25$:

    τ_Z =(1.6576393, -1.6576393, 0, 0)
  - 7-membered Ring, $1.00 > R_J > 0.56$:

    τ_Z =(0, 0, 0, 0)
  - 9-membered Ring, $0.33 > R_J > 0.26$:

    τ_Z =(1.985255, -1.985255, 0, 0)
  - 9-membered Ring, $1.00 > R_J > 0.33$:

    τ_Z =(0, 0, 0, 0)

- Family 3
  - Spin 1/2:

    τ_Z =(1.3333333, -1.3333333, -0.8164965,

    0.8164965, 0.8164965, -0.8164965,

-0.3333332, -0.3333333, 0.3333332,

0.3333333)

– Spin 3/2:

τ_Z =(-3.0000000, 3.0000000, -2.6312711,

-2.6312710, 2.6312709, 2.6312710,

2.2496977, 2.2496976, -2.1140639,

2.1140638, -2.2496976, -2.2496975,

-1.7202569, -1.7202570, 1.7202571,

1.7202569, -1.5275253, -1.5275253,

1.5275251, 1.5275253, -0.9351054,

-1.0491693, -1.0701131, -1.0701134,

-0.3333334, -0.3333332, 0.9351054,

0.3333332, 0.3333332, 1.0491692,

-0.8038927, -0.8038925, 1.0701132,

1.0701133, -0.7732639, -0.7732639,

0.7732639, 0.7732639, 0.8038925,

0.8038925)

B.3 Site spins of the Eigenvectors of τ_Z

- Family 1 homogeneous rings: Here the site spin in the non zero eigenstates of τ_Z is always of the magnitude $S_i = \frac{2S+1}{6}$ oriented towards the positive or negative tangential axis. giving $\tau_Z = \frac{2S+1}{2}$

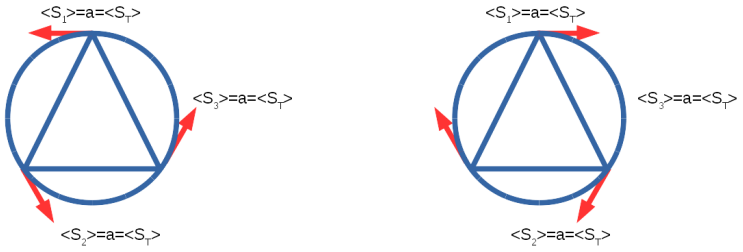

Site Spins for homogeneous 3-Site, Family 1

- Family 2 toroidal rings: Here the site spins are all equal and oriented towards the positive or negative tangential axis.

$$S_i = \begin{cases} 0.266666, & \text{if } N_{\text{site}} = 5 \\ 0.235579, & \text{if } N_{\text{site}} = 7 \\ 0.220584, & \text{if } N_{\text{site}} = 9 \end{cases} \tag{B.1}$$

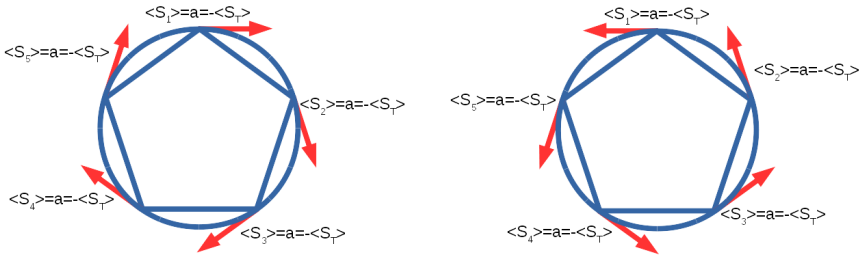

Site Spins for homogeneous 5-Site, Family 2

B.4 site S_z for for frustrated eigenstates of 9-membered ring

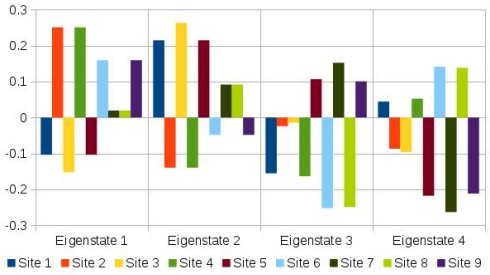

site S_z^i for Frustrated but not toroidal (9-Site, Family 1)in the lowest eigenvectors of the Hamiltonian

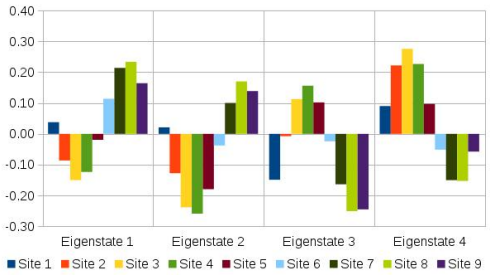

site S_z^i for Frustrated and toroidal (9-Site, Family 2, $.33 > R_J > .26$)in the lowest eigenvectors of the Hamiltonian

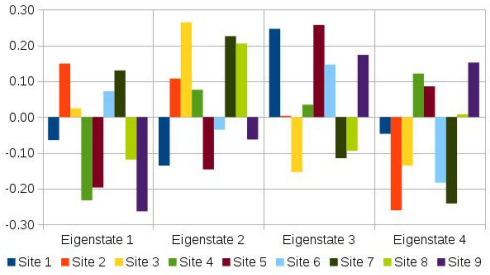

site S_z^i in Frustrated but not toroidal (9-Site, Family 2, $R_J > .33$)in the lowest eigenvectors of the Hamiltonian

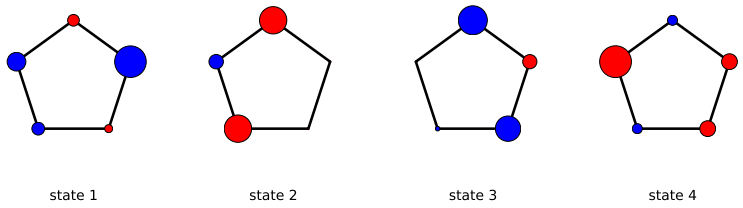

Site $< S_i^z >$ *for the four eigenstates of the ground state quartet in the 5-ring (Family 2) for* $R_J < 0.25$ *(non-toroidal quartet). Blue (red) circles correspond positive (negative) values of* $< S_i^z >$*, while the area of the circle is proportional to the magnitude of* $| < S_i^z > |$*.*

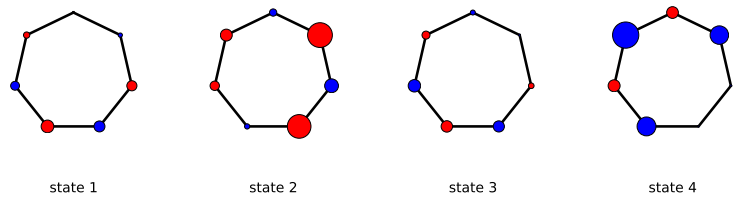

Site $< S_i^z >$ *for the four eigenstates of the ground state quartet in the 7-ring (Family 1), (non-toroidal quartet). Blue (red) circles correspond positive (negative) values of* $< S_i^z >$*, while the area of the circle is proportional to the magnitude of* $| < S_i^z > |$*.*

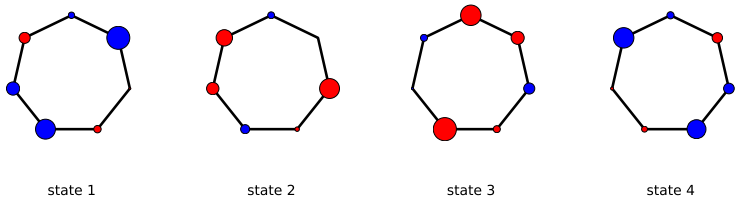

Site $< S_i^z >$ *for the four eigenstates of the ground state quartet in the 5-ring (Family 2) for* $R_J > 0.56$ *(toroidal quartet). Blue (red) circles correspond positive (negative) values of* $< S_i^z >$*, while the area of the circle is proportional to the magnitude of* $| < S_i^z > |$.